Sub-increment Based Iterative Constitutive Model for Cyclic Cracking-Crushing-Shearing in Masonry Interface Elements

Zihong Xie

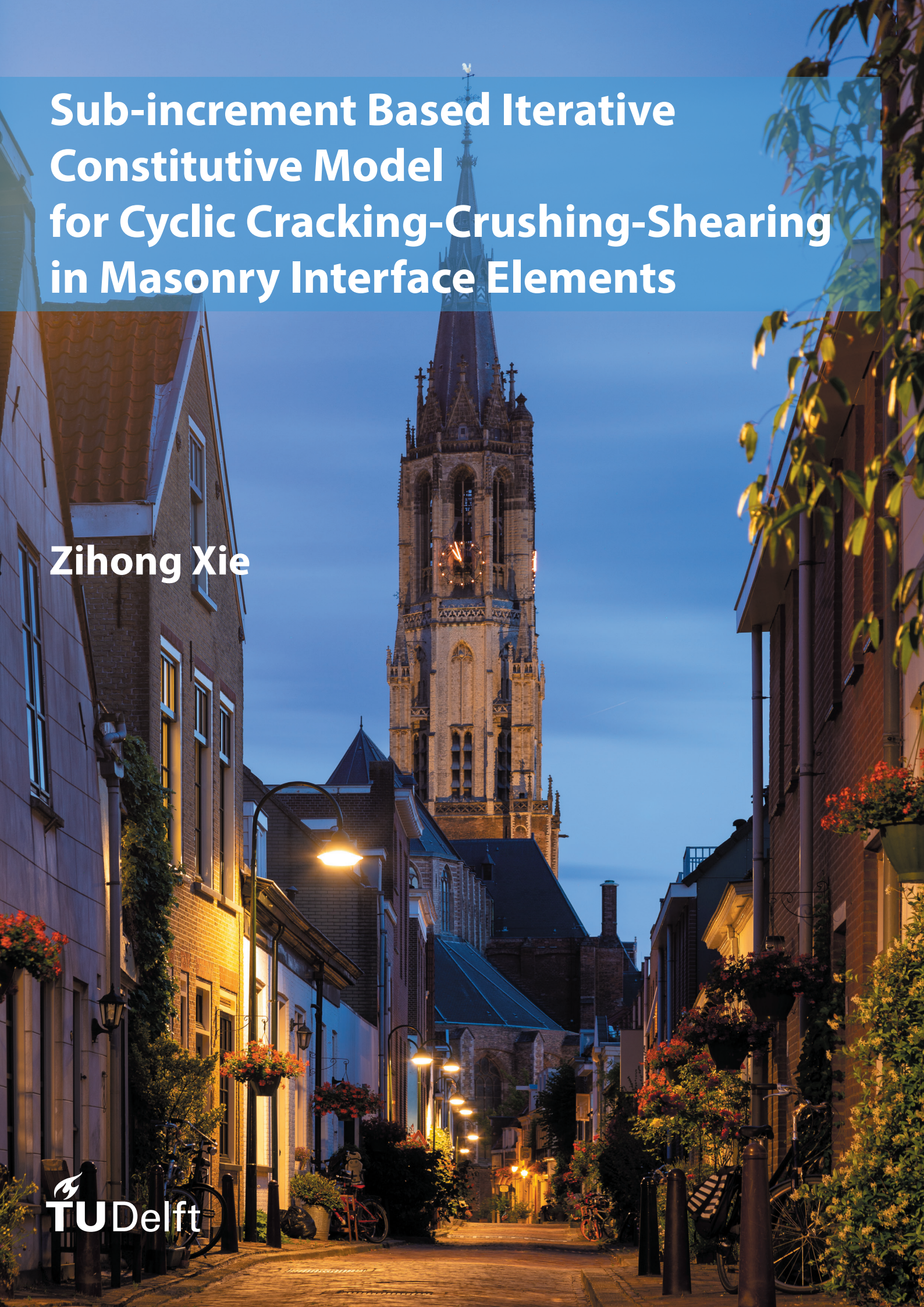

TU Delft

Sub-increment Based Iterative Constitutive Model for Cyclic Cracking-Crushing-Shearing in Masonry Interface Elements

by

Zihong Xie

to obtain the degree of Master of Science

at the Delft University of Technology,

to be defended publicly on Friday May 29, 2020 at 2:00 PM.

Student number:	4755715	
Project duration:	June 1, 2019 – May 29, 2020	
Thesis committee:	Prof.dr.ir. J.G. Rots,	TU Delft
	Dr. F. Messali,	TU Delft
	M. Sousamli, MSc,	TU Delft
	Dr.ir. G.J.P. Ravenshorst	TU Delft

This thesis is confidential and cannot be made public until May 28, 2020.

TU Delft

Acknowledgements

I take this opportunity to express my gratitude to the people who have been instrumental in the successful completion of this thesis.

First and foremost, I am deeply indebted to my committee members. They gave me the academic and moral supports as well as the freedom I needed to move on. Prof. Jan Rots, the Chair of my committee, inspired me with his scientific insights in this field and encouraged me to devote myself to this challenging but fascinating topic. His enthusiasm and immense knowledge steered me through this research. I am also extremely grateful to my daily supervisors Dr. Francesco Messali and Marianthi Sousamli for their valuable time, suggestions and guidance throughout the process. I will forever value those insightful discussions. Francesco always reminded me not to get lost in the minor details and ignore the big picture. He also provided unwavering guidance on the understanding of the mechanics of masonry. Marianthi helped me tackle numerous practical problems in the development of the model. She read through the manuscripts for multiple times and offered countless constructive suggestions. I must also thank Dr. Geert Ravenshorst, as the supervisor from the section of Biobased Structures and Materials, for his special perspectives and helpful advice on this thesis.

Also, the completion of my thesis would not have been possible without the results from the experiments conducted by Dr. Geert Ravenshorst, Dr. Francesco Messali, Dr. Rita Esposito and other staffs in Delft Univerisity of Technology. Many thanks to them for their great contributions and perfect works.

Heartfelt thanks are given to my family for their belief in me and understanding that learning is a lifetime venture. They continue to be a constant source of support no matter what I endeavour. I also thank them for their modelling of good work ethics and inspiring life philosophy. I would like to dedicate this study to my partner, who has cherished with me every great moment and supported me whenever I needed it. My thanks are extended to all my great friends during my bachelor and master studies. Their companion helped me sail through the most important seven years of education in my life. Last but not least, thank you to all the teachers in my life that taught me how to think and more essentially how to live.

Zihong Xie
Rotterdam, May 2020

Abstract

Masonry is one of the most commonly used construction materials for residential buildings and historic buildings around the world. Some of these buildings are located at seismic zones, while unreinforced masonry structures are vulnerable to large lateral loads. To assess and strengthen the existing masonry buildings and to design new and complex masonry structures, nonlinear seismic simulations are conducted with macro modelling or micro modelling approach. The macro modelling approach, which smears out the details of the bricks and joints as a homogenous material, can efficiently and robustly model complete masonry structures. A commonly used orthotropic constitutive model is the Engineering Masonry Model of the DIANA FEA, which is based on the Total Strain Method that eliminates the mapping-back process in conventional elastoplastic constitutive models. The micro modelling approach, which explicitly models the bricks and joints, can better represent the mechanical behaviours of masonry, and it is applied more on the simulations of structural components. However, most of the constitutive models used in micro modelling are based on elastoplasticity that usually causes numerical difficulties due to its mapping-back process. The lack of a robust constitutive model has severely hindered the application of this accurate analysis approach.

To resolve the problem, this thesis proposes a sub-increment based iterative constitutive model for interface elements, based on Multi-surface Plasticity Criterion, including Coulomb friction, tension cut-off and compression cut-off. This model aims to enhance the robustness and accuracy of the constitutive model used for the micro modelling of masonry structures. It eliminates the conventional mapping-back process in elastoplastic constitutive models by introducing the ideas of sequential uni-axial loading algorithm in normal and shear directions and an extra damage iterative calculation algorithm. These algorithms are robust even when the stress state is at the corners of the yield surface. The model also introduces the concept of sub-increments to consider the path dependency in plastic process. All the formulations of this constitutive model are derived based on a simple mechanical model. Formulas and examples are provided for obtaining the input parameters from material tests. The proposed constitutive model is tested on a single integration point level and found to be stable and reliable. It is further applied on the component level, by modelling three masonry walls of different dimensions and boundary conditions, under cyclic loading. For the verification of these wall models, the numerical results are compared with the experimental results in terms of force-displacement curve and crack pattern. Finally, the thesis presents a brief study on parameter sensitivity to provide guidelines for the level of accuracy needed for each input parameter, in order to get satisfactory numerical results.

The constitutive model is found to be robust for all the wall analyses conducted, without encountering divergence. The comparison between numerical results and experimental results shows that this constitutive model can cover the majority of shear and flexural failure mechanisms and mimic the crack patterns well. It is capable of modelling shear failure with high accuracy. It can also model flexural failure well with a few parameters calibrated. The fact that the model is little sensitive to parameters that are hard to be measured from experiments, such as tensile strength and tensile fracture energy, ensures its feasibility in engineering practices.

Therefore, the introduction of this sub-increment based iterative constitutive model fulfils the need for a robust, reliable, accurate and feasible constitutive model for interface elements in masonry micro modelling. We anticipate this thesis to be a good starting point for future studies on more sophisticated and robust constitutive models for interface elements, not only for masonry structures but also for all the structures with weak interfaces that are prone to crushing, cracking and shearing.

Keywords: Finite Element Method, constitutive model, interface element, masonry, discrete crack model, mirco modelling, cracking-crushing-shearing, cyclic loading.

Contents

List of Figures

List of Tables

1 Introduction

1.1. Motivation

The long-term gas extraction in the northern Netherlands, since the 1960s, has induced a high number of earthquakes. Since 1991, Earthquakes with magnitude greater than 1.5 have been recorded for 333 times, according to The Royal Netherlands Meteorological Institute (KNMI) [5]. After 2001, the magnitude and number of earthquakes increased, leading to more cracks or even damage to numerous building. Therefore, the annual gas extraction is judicially limited to 24bcm in order to reduce the earthquake activity, which could understate the necessity for (further) research of the seismic behaviour of the structures, if earthquakes could be avoided. However, if the extraction is stabilized at 24bcm per year, the annual number of earthquakes would still gradually increase, with an expected all-time maximum magnitude of 4.5 [15]. Geographically, Groningen is one of the major provinces that are heavily influenced by the hazard. However, the building stock in the Groningen province was not designed to withstand large lateral loads. Moreover, the unreinforced masonry (URM) buildings constitute the vast majority of the building stock. As the induced earthquakes will continue to influence the safety and serviceability of numerous masonry structures in the northern Netherlands, the necessity of accurate, efficient, and robust nonlinear seismic simulation for masonry structures must be emphasized.

From a broader point of view, masonry is one of the primary construction materials for historic buildings, and time has proved its durability. Also, it is still widely used in the modern building industry, especially for affordable housing. Because numerous masonry structures are built in the underdeveloped countries and regions, when performing FEM analyses, the input parameters of the model should be straightforward, so that the few or no calibrations are needed to ensure accuracy. Otherwise, it will hinder the engineers from performing simulations effectively.

Technically, nonlinear FEM simulations aim to assess and strengthen the existing masonry structures under complex loading cases, and also, to validate the design of new and complex masonry structures. The numerical simulations usually utilize three types of modelling approaches, namely the detailed micro-modelling, the simplified micro-modelling, and the macro-modelling [13], depending on whether the bricks, the mortar, and their interfaces are explicitly modelled or not. The macro-modelling is implemented as the renowned smeared crack model in most of the FE analyses. On the other hand, the micro-modelling is realized by the discrete crack model.

For the smeared crack model, a constitutive model called the Engineering Masonry Model was created to take into account the orthotropy of masonry, as well as its behaviour under shear. Furthermore, this model can also better capture the cyclic behaviour of masonry, in comparison to the conventional Total Strain Rotating Crack Model, also commonly used for masonry. Both the Engineering Masonry Model

and the Total Strain Rotating Crack Model are based on the total strain method[8], which eliminates the mapping back process in the plastic calculation and therefore is more robust than conventional elastoplastic constitutive models. On the other hand, the discrete crack model[1] with interface elements is still using elastoplastic constitutive models. These conventional constitutive models are not as robust as the Total Strain based Constitutive Model, especially when mapping back the stress onto the yield surface.

The micro modelling approach is a more accurate representation of the mechanical behaviour of masonry and returns the most accurate numerical results between the different modelling approaches. On the other hand, the macro modelling approach is less accurate than the micro modelling. However, it significantly eases the computational demand of the numerical analyses and is therefore commonly preferred for modelling of large structures. Therefore, in most cases, micro modelling is described as an approach that focuses more on the local aspect, while the macro modelling is used for complete structural analysis. The local aspect, specifically, is the investigation of single structural elements (e.g.piers and walls). This would allow studying in detail the behaviour of these elements, giving the opportunity to run numerical simulations in place of more expensive and time-consuming experimental tests. However, the application of the micro modelling, in other words, the discrete crack model, is not limited only to the local masonry analysis. It can also be applied to the analysis of complete structures. The possible applications of the interface elements in the discrete crack models can also be extended but not limited to

- Mortar joints of the entire masonry building model built with huge concrete/masonry blocks (joints between calcium silicate masonry elements);
- Dowels and anchors in masonry wall described by $\Delta u - \tau$ relation;
- Shear cracks of the concrete beam with predefined location;
- Vertical joints between two walls in two different directions;
- Joints between different materials, for example, the connections between timber beams and masonry walls.

Given such a broad range of applications and the lack of available robust constitutive model, it would be interesting to develop a more robust and accurate constitutive model than conventional elastoplastic models for the interface elements used in discrete crack models.

1.2. Research problem

This thesis tries to answer if it is possible to develop a constitutive model for interface elements that will outperform the robustness and accuracy of the current elastoplastic constitutive model used in simplified micro modelling of masonry, while also maintaining a certain level of computational efficiency. The proposed constitutive model should be based on a multi-surface failure criterion that includes the different types of cyclic failure observed in masonry interfaces: tensile cracking, compressive crushing, and shear sliding. It will be developed based on the structural behaviours and mechanical understanding of masonry walls and validated against related experimental data.

1.3. Aims and scope

For modelling of masonry structures, the pursuit of accurate and robust simulations that reflect their genuine mechanics has posed a continuous challenge to the study of material properties and constitutive models for a long time. To date, extensive tests have been conducted ranging from small-scale

[1] The word ”crack” of the discrete crack model is somehow misleading as it can not only model tensile cracking but also shear sliding and compressive crushing.

material level to full-scale structural level for masonry. Numerous constitutive models have been developed based on the studies of material and structural behaviours.

However, the material properties of the bricks, the mortar layers, and the interfaces between them have a very high level of uncertainty, as indicated from material tests. Some of the material properties are even hard to be measured through experiments, such as the tensile strength and fracture energy. On structural level, the construction process also results in more variation of the material properties and introduces different kinds of imperfections in the wall. Additionally, differences in loading conditions and boundary conditions between small scale material tests and the tests in structural level might also lead to differences in the value of the properties.

In computational modelling, different levels of simplification can be applied to the modelling of the structure to reduce the computational cost and lower the probability of numerical difficulties. Of course, these simplifications of the model should not severely influence its accuracy. Therefore, material properties obtained from tests must be translated[2] to match the simplified model. These translations (calculations) are not always straightforward, which can generate more uncertainty. For instance, the smeared crack model is homogeneous and at best orthotropic, while the real masonry is more complicated than this, not to mention the differences in the crack development or softening processes. Because of that, the input parameters used for smeared crack models cannot be directly obtained from material tests. Moreover, parameter calibrations or sensitivity studies are necessary to make the analysis reliable. Thanks to the extensive study, the Engineering Masonry Models has provided a robust and satisfactorily accurate approach for simulation, and it is still improving these years. This model does not have a mapping-back process that usually causes numerical difficulties. Besides, the loading and unloading behaviours are more realistic compared to conventional elastoplastic constitutive models. In contrast to the smeared crack model, the discrete crack model, which at least explicitly differentiates bricks and mortar, is geometrically and mechanically more similar to the masonry structure. It makes the translations (calculations) of the material properties derived from the experiments into the input parameters for the constitutive model more straightforward than that for the smeared crack model. Besides, the crack development is also more realistic, propagating along the weak joints such as the mortar-brick interfaces. However, the lack of a robust constitutive model that is based on the real mechanical behaviour of the weak joints makes the use of interface elements or micro modelling less appealing.

Therefore, to bridge this gap, the theory of a new iterative constitutive model based on mechanics will be introduced for the discrete crack model.

To be specific, the scope of the current study is to propose a robust constitutive model for interface elements for nonlinear cyclic analyses. The constitutive model defined herein is specially developed for masonry structures, where the zero-thickness interface elements represent the combined mechanical behaviour of the mortar layers and the interface between the mortar and the bricks.

The developing constitutive model will be implemented on the simplified micro model of masonry. Particularly, the study has the following objectives:

1. To eliminate the mapping-back process used in conventional constitutive models that cause numerical difficulties by an iterative method based on clear mechanical concepts;

2. To implement appropriate loading and unloading behaviours for tension, compression and shear, in order to ensure the proposed constitutive model can cover the majority of the failure mechanisms;

3. To verify the stability and reliability of the proposed constitutive model;

4. To validate the numerical results from the FE analyses adopting this proposed constitutive model against the experimental results;

[2]The word ”translate” means to calculate the equivalent input parameters for FEA from the parameters obtained in material tests.

5. To provide formulas for calculating input parameters for FE analyses, based on material properties from material tests;
6. To conduct a brief parameter sensitivity study for this constitutive model and provide guidelines for parameter calibration.

1.4. Structure of the work

The thesis starts with an overview of the three modelling approaches used for masonry structures and the available constitutive models designed for them (Chapter 2). Then the failure mechanisms on both micro and macro level are reviewed. After that, the rest of the chapters are directed towards the simplified discrete crack, which is one of the three modelling approaches. The constitutive models available for the discrete crack model is reviewed with more details.

Chapter 3 aims at formulating the theories of this constitutive model with some assumptions based on a simple mechanical model. One of the fundamental assumptions is that the zero-thickness interface elements lump all the nonlinearities of the bricks, mortar layers, and the interfaces between them. Therefore, formulas are derived for translating (calculating) the equivalent input parameters for the interface elements from the material tests. Next, the uni-axial constitutive relations of tension, compression, and shear are discussed. Most importantly, the coupling effect between normal and shear directions and the iterative method to calculate the damage are proposed also based on the mechanical model. Besides, the concept of sub-increments is introduced, considering the path dependency of the plastic process.

Chapter 4 explains the implementation of the theories proposed in chapter 3. Extensive flow charts are illustrated to show the structure of the code from overview to detailed modules. Five main modules, namely the Elastic Predictor, the Elastic Calculator, the Elastic Limit Finder, the Plastic Calculator, and the Constitutive Array Re-Constructor, constitute the code of this constitutive model.

Chapter 5 and 6 validate the proposed constitutive model on both single integration point level and structural wall level.

In chapter 5, the validation on the single integration point level examines the plastic calculation process of the algorithm under various plastic loading cases. The influences of the Coupling Options and sub-increments, introduced in chapter 3, on the numerical results are also discussed.

In chapter 6, the validation on the wall level reveals the capability of the constitutive model to simulate different types of failure mechanisms and force-displacement curves by comparing the numerical results with the experimental data. The verifications cover short and long walls characterized by flexural and shear failure mechanisms. Some parameters are also calibrated to better simulate the experiments with reasons explained.

In chapter 7, a brief parameter sensitivity study is conducted to broaden the validation of the constitutive model. The input parameters are varied by a certain amount, and the influences on the force-displacement curve and the crack pattern are checked. The parameter study provides guidelines for how precise a particular parameter is required to be in order to get reliable results from the analyses.

Last but not least, chapter 8 completes the thesis with reflection and summary in a critical manner to show the strength and weakness of the proposed constitutive model. Suggestions for future researches are also provided.

2

Background and literature review

2.1. Three numerical modelling approaches for masonry

Traditionally, the design and assessment of masonry structure mainly rely on empirical formulae and rules-of-thumb. Unlike the relatively sophisticated numerical study on concrete structures, the research community has only adopted numerical tools to masonry structures for the past 30 years. The difficulties that hinder the adoption of well-developed numerical models, such as the models for concrete, to masonry structure stem from its particular characteristics. Unreinforced masonry mainly comprises units and mortar joints, which cannot be treated as an isotropic material like concrete. To better capture the anisotropic behaviour of its units, mortar layers and their interactions, three types of numerical models are developed: the detailed micro-modelling, simplified micro-modelling, and the macro-modelling, as shown in figure 2.1 [13].

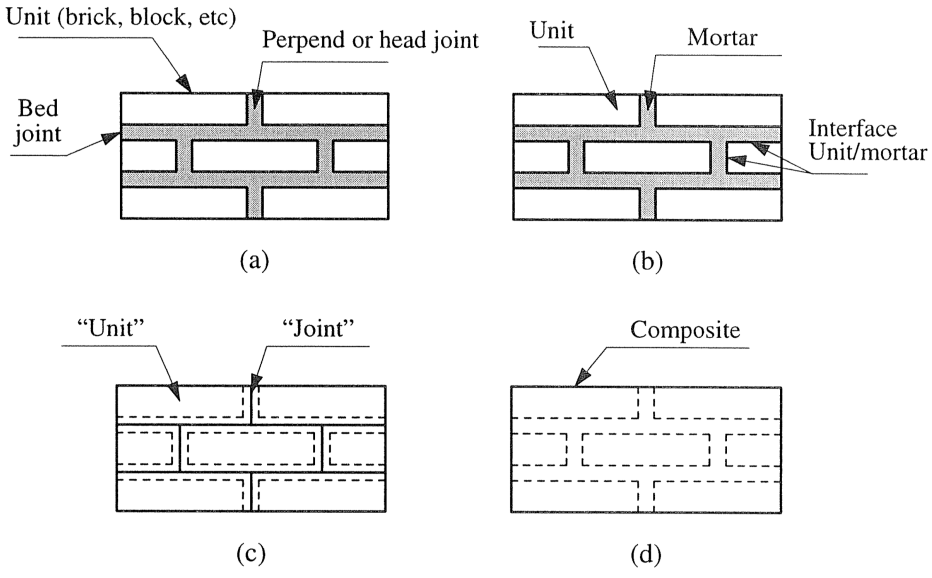

Figure 2.1: Modelling approaches for masonry structures: (a) Masonry sample; (b) Detailed micro-modelling; (c)Simplified micro-modelling (d) macro-modelling

- The detailed micro-modelling is the most accurate and comprehensive one. Both the units and mortar are modelled by continuum elements (shell elements), with the interface in between them

modelled by discontinuous elements (interface elements), see figure 2.1 (b). In this approach, Young's modulus, Poisson's ratio, and optionally, the inelastic properties of both the units and the mortar joints are taken into account. However, it is the most computationally demanding and memory consuming model;

- For the simplified micro-modelling (also called as meso-modelling), the mortar joints are further simplified to 1D interface elements, as shown in figure 2.1 (c). The continuum elements representing the units remain the same as the detailed micro-modelling. Therefore, the Young's modulus and the Poisson's ratio of the units are still included, while the Poisson's ratio of the mortar joints is lost. When considering the nonlinear behaviour of the structure, it is usually assumed that the units remain elastic throughout the analysis, whereas all the plastic behaviours and possible fractures are lumped into the joints (the interface elements). The computation is less demanding with some loss of accuracy;
- In contrast, for macro-modelling, the mortar joints and the units are not distinctively modelled. The possible cracks are smeared out, and the masonry is treated as an homogeneous composite. The constitutive relation is hereby established between the average masonry strain and average masonry stress, mainly obtained by tests on a sufficient scale. This approach focuses more on global structural behaviours than local interactions between the units and mortar joints.

The macro-modelling is implemented based on the smeared crack model in FE analyses. And the micro-modelling is based on the discrete crack model. Both the smeared crack model and the discrete crack model are originally developed for the concrete fracture behaviour by Ngo and Scordelis [10] and Rashid [11]. They are later extended to the field of masonry simulation. For in-plane behaviour, see Anthoine [1] and Lourenço [6], and for out-of-plane behaviour, see Ferreira, et al [4]. For this thesis, only in-plane behaviour is discussed.

In the simulation practice of masonry structure, the smeared crack model is generally used to evaluate the overall performance of the entire structure. The discrete crack model focuses more on the local effect, but it is not limited to local analyses, as mentioned in section 1.1.

To enhance the robustness of the smeared crack model used in masonry simulation practice, based on the Total Strain Constitutive Model, the Engineering Masonry Model is developed in the Delft University of Technology and applied in the DIANA FEA package [8], which is widely acclaimed in the industry. Note that from both the theoretical and the engineering practice point of view, the Engineering Masonry Model is more robust and accurate in masonry modelling than the Total Strain Model with rotating cracks, as validated by Schreppers, et al [14].

However, for the discrete crack model, studies to improve the robustness and accuracy of the constitutive model relatively stagnate. Hence, for this master project, the main content will target the development of a robust constitutive model for the interface element, which is for the simplified micro-modelling strategy. Accordingly, the macro-modelling strategy and smeared crack model will not be further discussed in the following chapters.

2.2. Failure modes of masonry

On the micro level, the failure mechanisms of the masonry include the following five modes, namely (a) joint tension cracking, (b) joint slip, (c) unit direct tension crack, (d) unit diagonal tension crack and (e) masonry crushing specified by Lourenço and Rots [7], as shown in figure 2.2.

- The joint tension cracking is the most common failure mode when the masonry pier is in tension;
- The joint slip is the sliding along the bed or head joints under low-value normal stress;
- The unit direct tension crack occurs when the units are in tension in the longitudinal direction;

- The diagonal tension cracking is the shear failure of the units when the normal stress is sufficient to develop friction in the mortar joints;
- The masonry crushing is the splitting of units in tension as a result of mortar dilatancy under high-value compressive stress.

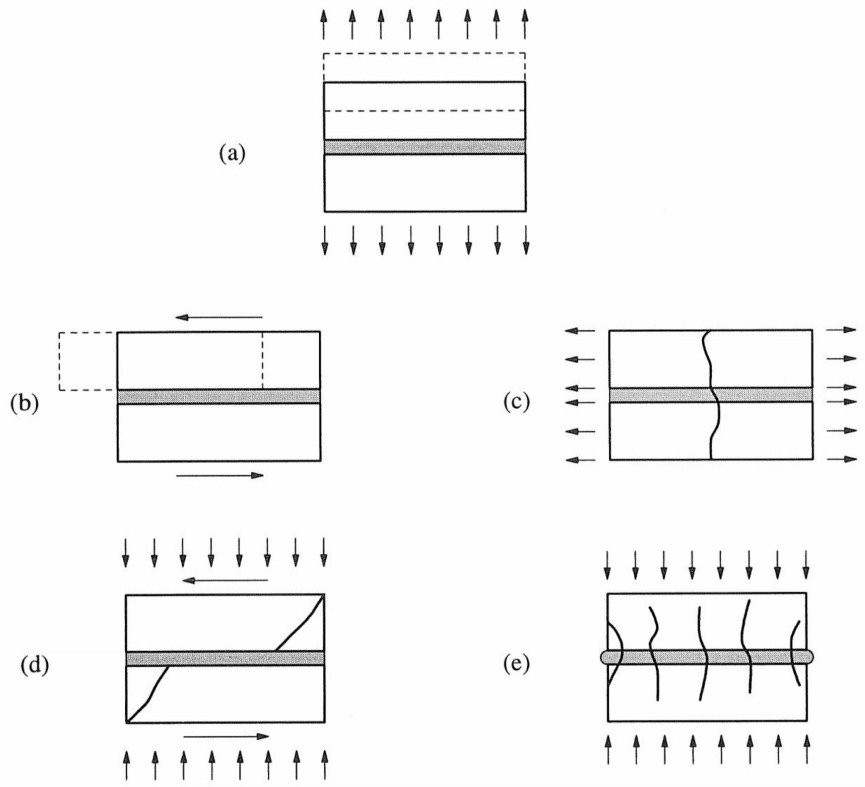

Figure 2.2: Failure mechanisms of masonry (a) Joint tension cracking (b) Joint slip (c) Unit direct tension crack (d) Unit diagonal tension crack (e) Masonry crushing

On the macro level, the masonry walls are usually divided into piers by the existing openings. Under vertical and horizontal loads, the failure mechanisms of the masonry piers as a whole are mainly the rocking failure, sliding shear failure, diagonal cracking failure, and toe crushing [9].

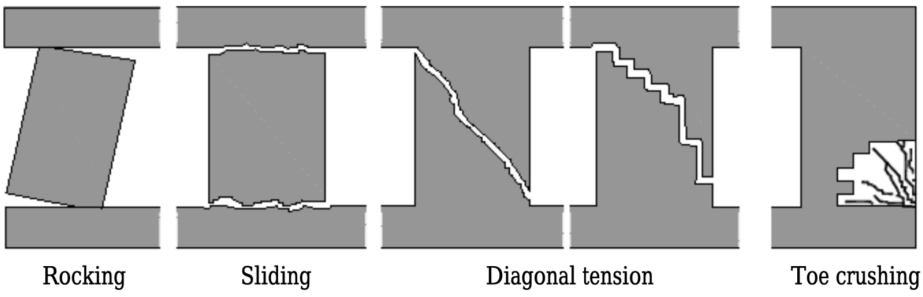

Figure 2.3: Failure modes of masonry piers (a) Rocking (b) Sliding shear failure (c) Diagonal tension cracking (d) Toe crushing

- The rocking failure occurs with wide tensile cracks at the top or bottom tensile zone of the piers where the moment maximizes;

- The sliding shear failure is associated with the sliding along the cracks in the bed joints, due to the lack of frictional resistance;
- The diagonal cracking failure is due to excessive shear stresses. As a consequence, the inclined diagonal cracks form along the mortar bed and head joints, or go through the units;
- The toe crushing occurs when the principle compressive stress caused by moment and axial compression causes crushing of the bed joints or splitting of units at the corners.

Note that the in-plane failure of masonry structures is usually the combination of these modes, depending on the overall behaviour, specifically the flexural behaviour, the shear behaviour, or the combination of them.

In flexural behaviour, if the vertical load is relatively low compared to the horizontal load, the induced moment produces tensile cracks at the corner, and the entire pier will rotate around the compressed corner, which is the rocking mechanism. If the vertical load is high and the compressed corner is crushed, then the combination of rocking and toe crushing occurs.

In shear behaviour, the bed joints on a certain height may not be able to resist the shear force especially when the cracks of that bed joints initiate and develop due to the normal tensile stress as we see at the beginning of the rocking behaviour, such that the failure occurs sliding on the cracked bed joint. The diagonal tension cracking happens when the principle tensile stress due to shear load exceeds the strength of the masonry. Whether the crack propagate through the joints or the units depends on the strength of the mortar joints, the units and the interface between them.

2.3. Constitutive models for interface element

2.3.1. Combined Cracking-Shearing-Crushing

The Combined Cracking-Shearing-Crushing model is a plane stress interface cap model of masonry structure formulated by Lourenço and Rot [7]. This model, as shown in figure 2.4, is based on the multi-surface plasticity model bounded by a composite yield surface that includes the Coulomb friction model, a tension cut-off, and an elliptical compression cap. The elastic domain is defined by $f_i < 0$ where f_i is the yield functions of tension, shear and compression failures. The loading and unloading can be written as the condition in the Kuhn-Tucker form as follows

$$\dot{\lambda}_i \geq 0, f_i \leq 0 \quad \text{and} \quad \dot{\lambda}_i f_i = 0 \tag{2.1}$$

where λ_i is the plastic multiplier.

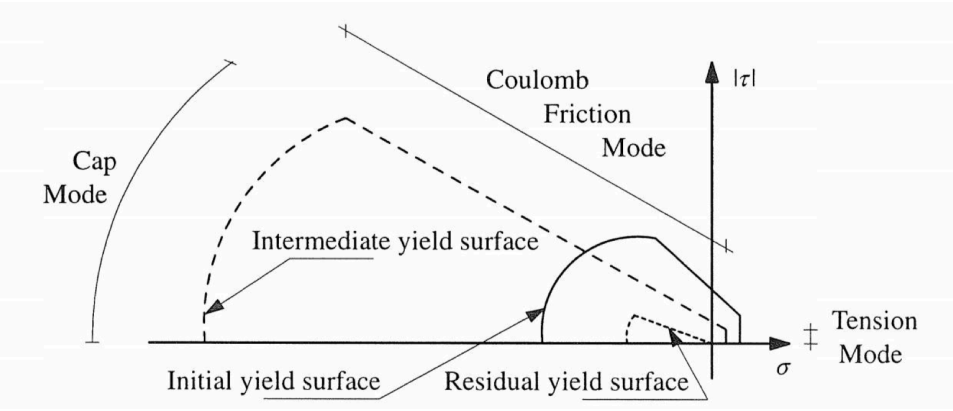

Figure 2.4: Two-dimensional interface cap model

The yield function is assumed to be as follows

$$f_i(\boldsymbol{\sigma}, \kappa_i) = \Phi_i(\boldsymbol{\sigma}) + \Psi_i(\kappa_i) \tag{2.2}$$

where κ_i is the amount of hardening or softening; and Φ and Ψ are the generic functions. The detailed description of the yield functions is specified by Lourenço and Rots [7]. As it is a plasticity based model, the total relative displacement rate $\dot{\boldsymbol{\varepsilon}}$ is decomposed into an elastic part $\dot{\boldsymbol{\varepsilon}}^e$ and a plastic part $\dot{\boldsymbol{\varepsilon}}^p$.

$$\dot{\boldsymbol{\varepsilon}} = \dot{\boldsymbol{\varepsilon}}^e + \dot{\boldsymbol{\varepsilon}}^p \tag{2.3}$$

The elastic constitutive matrix is then defined as below only related to the elastic part $\dot{\boldsymbol{\varepsilon}}^e$

$$\dot{\boldsymbol{\sigma}} = \boldsymbol{D}\dot{\boldsymbol{\varepsilon}}^e \tag{2.4}$$

The rate of the plastic relative displacement component for non-associated plasticity materials such as mortar is defined as

$$\dot{\boldsymbol{\varepsilon}}^p = \dot{\lambda}\frac{\partial g}{\partial \boldsymbol{\sigma}} \tag{2.5}$$

where g is the plastic potential.

Experience has shown that the Combined Cracking-Shearing-Crushing model is not robust enough if the size of the masonry walls is relatively large compared to the unit size and when its layout is complicated. The reason for this problem in convergence is that when the trial stresses in the iterations are so high that they are already out of the area bounded by the yield surfaces, mapping back to the yield surfaces might cause difficulties. This situation generally exists for plasticity based model and becomes worse when trying to map back to the corner of the yield surfaces.

2.3.2. Nonlinear Elasticity

The nonlinear elasticity model is essentially an elastic model. It is physically realistic for some materials to undergo large deformation, for example, rubber or some polymer materials, which are different from normal construction materials. The strains of the construction material are usually very small, and within the elastic regime, the elastic modulus almost remains constant. When the strains exceed a small yield strain, the materials turn into the plastic stage. In contrast, materials such as rubber can be in the elastic stage even under large deformation; however, the stiffness is no longer a constant, and the stress-strain curve in the elastic regime becomes nonlinear. Of course, because the materials are still in the elastic stage, the unloading and reloading follow the same curve, and no residual strain is produced.

Although the nonlinear elasticity model is developed for elastic analysis, it can also be used in plastic analysis if the entire analysis process does not include any unloading or reloading. This is because the curve defined in nonlinear elastic constitutive relation is basically the same as the nonlinear stress-strain curve, including the elastic part and the plastic softening or hardening.

If the convergence problem occurs when using the Combined Cracking-Shearing-Crushing model for a monotonic analysis, the nonlinear elasticity model could be a good alternative as it is numerically more stable. For instance, a simple way to do this is by decoupling the shear and normal components, such that two corresponding stress-relative displacement curves could be defined respectively in shear and normal directions for interface elements. The model with interface elements using this simple nonlinear elasticity constitutive relation is very robust and could well mimic the behaviour of the masonry under monotonic load. The reason for the robustness is that, different from the plasticity model, the total relative displacement of the interface element is not decomposed into an elastic part and a plastic part. The calculation of the stresses is straightforward as the stresses are directly related to the total relative displacements based on the predefined decoupled nonlinear constitutive relations. No mapping back to the yield surface is needed; therefore, the numerical difficulties are avoided.

However, providing that the unloading and reloading follow the same path as loading, the cyclic energy dissipation and plastic damage is not realistic when the nonlinear elasticity model is used for plastic

analysis. Therefore, the nonlinear elasticity model cannot be used for nonlinear cyclic or transient dynamic nonlinear analyses. This also emphasizes the need for a total relative-displacement model that includes more realistic unloading and reloading behaviours.

2.3.3. Summary

The Combined Cracking-Shearing-Crushing model is a sophisticated plasticity based constitutive model for interface elements. It has already included all the micro failure mechanisms mentioned in section 2.2. The reliability of this model was proved by comparing the simulation results with the experiments. However, due to the nature of the conventional elastoplastic model, the FEA program needs to map the trial stresses back onto the yield surface. Although numerous methods are introduced to overcome the potential difficulties during the mapping-back process, the performance is still not robust enough, especially when the structure becomes large and complicated. Besides, as it is a sophisticated model, in order to capture the real behaviour of the structure, a significant number of input material parameters need to be calibrated, which is not a straightforward task for normal engineers without enough experience and experimental data.

In comparison, the Nonlinear Elasticity is a straightforward model for nonlinear plasticity simulation, including the hardening and softening processes. The stresses are uniquely related to the set of shear and normal strains provided. The mapping-back process is no longer needed, and the shear and normal directions are completely decoupled, so the analysis becomes unconditionally stable. It is significantly more robust than the plasticity-based model with fewer parameters to calibrate. The computation is also less demanding. But the local failure mechanisms are not as well duplicated as the Combined Cracking-Shearing-Crushing model. Of course, the nonlinear elasticity model can never mimic the realistic plastic unloading or reloading, neither the cyclic behaviours (e.g., the degradation of forces and dissipation of energy), but it does provide some insights into the way to overcome numerical difficulties by eliminating the mapping back process.

The constitutive model developed in this thesis has 3 assumptions that determine how and to what degree the shear and normal direction are coupled. They are listed as follows.

- The incremental displacements in normal and shear directions are applied sequentially instead of simultaneously to calculate the corresponding tractions in these two directions, for the sake of simplicity. This is discussed in detail in section 3.5.
- The model is based on a multi-surface failure criterion which includes the Mohr-Coulomb criterion, which means the stress state in normal direction will influence the stress capacity in the shear direction and vice versa, which will be discussed below.
- The model assumes a fully coupled behaviour between loss of cohesion in shear direction and the loss of tensile strength in normal direction, which means they decade with exactly the same rate (in terms of proportion).

The multi-surface failure criterion that includes tensile, compressive and shear failure are shown in figure 3.9. The interface degrades in tension and shear with softening, as shown in the uni-axial tensile and shear constitutive curves (figure 3.7 and 3.8). And it fails in compression with firstly hardening and then softening, as shown in the parabolic compressive curve or modified Engineering Masonry Model compressive curve (figure 3.5 or 3.6). Specifically, the softening in tension and shear results in shrinking of the yield surface to the origin. The hardening in compression causes the compression cut-off to move left first, and them move right for the following softening.

The “new” constitutive model will try to combine the advantages of these two existing models detailed above. To be more specific, the stresses of the integration points on the interface elements will be calculated with an iterative algorithm that does not involve the mapping back process. Its performance

at the corner of the yield surface should be as robust as if it is not at the corner. The shear and normal stress components will only be partially coupled to reduce the complexity of the model but still need to be implicitly correlated, considering the multi-surface plasticity criterion. The loading, unloading, and reloading behaviours for tension, compression and shear will also be taken into account. The new model can trade off some precision for the gain in robustness and ease of parameter calibration. Nevertheless, it still should be reliable overall.

3

Theories and assumptions

As mentioned in section 2.1, this thesis focuses on the constitutive model for interface elements used in a discrete crack model. In essence, this constitutive model calculates the stress of the interface element based on the given increments of relative displacements. Also, the uni-axial loading algorithm and the iterative damage calculation algorithm will be introduced as the core concepts to update the stress state and the corresponding damage, which is different from the conventional plasticity model.

Before getting into the core concept, to better understand the stress-relative displacement relation of the brick-mortar joint, a mechanical model of two bricks and one mortar layer in between, where crack only occurs in the mortar layer with a certain thickness, will first be introduced to represent the mechanical behaviour of the real structure. And this relatively detailed mechanical model will be further simplified to a small discrete crack model where material nonlinearity of bricks, mortar layers and the interface between them are lumped at the predefined zero-thickness interface element. This is to facilitate the FEM simulation and reduce the computational cost. They are discussed in section 3.1.

The following content in section 3.2 and 3.3 will explain the uni-axial constitutive properties of the interface element, and how they are related to the mechanical model and the experimental results. Some assumptions are further made to consider the influence of Mohr-Coulomb Criterion when updating stresses in the uni-axial plastic calculations in normal and shear directions sequentially.

Section 3.4 is to tackle the biggest challenge. That is to reasonably determine the extra amount of damage to the interface with an iterative manner each time after the uni-axial plastic calculation in normal or shear direction.

In section 3.5, the concept of sub-increments is introduced to consider the influence of the loading history on the plastic calculation.

Note that the main subject of this model in the thesis is masonry, but it should not be limited to masonry only, as discussed in section 1.1.

3.1. Detailed mechanical model and simplified discrete crack model

For orthotropic structures which tend to crack or crush along weak surfaces, such as the mortar layers in the case of masonry, it is reasonable to assume that all the plastic deformations are concentranted at the weak joints, which are, for masonry structures, the mortar layers and the bonded interfaces between the mortar and the brick units. Therefore, a detailed mechanical model is introduced herein, as shown

on the left of figure 3.1. To make the illustration more straightforward, the head joints are neglected temporarily such that the structure is simply composed of two units and one joint in between.

We further assume that there is a horizontal cross-section in the joint with the highest amount of imperfection that becomes the weakest cross-section of the entire mechanical model. Therefore, that horizontal cross-section in the joint will reach its strength first, as its tensile or shear stress increases. Then, only one crack will initiate along that cross-section. And the stresses in that cracked interface, as well as the adjacent mortar layers and the units, will not further increase but decrease according to the amount of softening in that crack. So far, the assumptions of the mechanical model are all introduced. And this mechanical model will facilitate the derivation of the properties of the zero-thickness interface elements afterwards.

For Finite Element Analysis (FEA), it is suitable to use a simplified micro model with interface elements modelling the joints of the mechanical model including the mortar layer and the interfaces between the mortar layer and the units as a whole. For this simple structure with two units and one joint, the simplified FE model is just as shown on the right of figure 3.1, which balances the computational cost and the details of the FE model. The bold red line represents the interface element with zero thickness representing the joint of the detailed mechanical model.

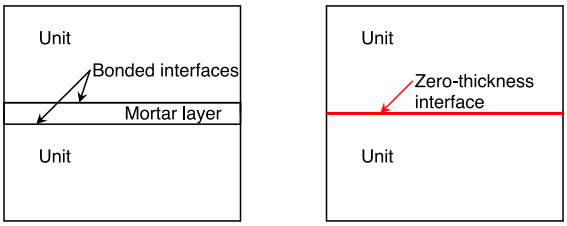

Figure 3.1: The detailed mechanical model of the structure and its simplified discrete crack model

In FE analysis, the simplified micro model also assumes that the nonlinear behaviour is concentrated at the zero-thickness interface element, whereas the units are always in elasticity. This assumption agrees with most of the experimental results, that most of the deformation of the masonry is contributed by the mortar layer and the adhesive interface between the mortar and the unit. Cracks also more often occur along the joint instead of going through the unit, as the bond strength of the interface between mortar and units and the strength of the mortar itself are usually lower than the tensile strength of the units. Of course, if cracks do initiate and propagate through the units, additional dummy interface elements can be added in the units. Or alternatively, smeared crack properties can be added to the units but the computation cost as well as the difficulties in convergence will significantly increase. Because of the relatively low probabilities of nonlinearity in the units, it is reasonable to assume that they remain elastic throughout the analyses in this thesis. It is important to realize that the cracked surface in the mechanical model does not necessarily share the same line with the zero-thickness interface element of the FE model, which is proved in section 3.3.

As the upper and lower units are assumed to be always elastic, only the elastic modulus, Poisson's ratio and density are needed. They can be obtained through the material test of the unit. For the material properties of the joints composed by mortar layer and its interfaces with the adjacent units (they are called the joint afterwards to be more concise), they cannot be tested directly. And also these properties need to be further translated (calculated) for the simplified interfaces with zero-thickness. For example, the equivalent elastic and plastic properties of the zero-thickness interfaces element are actually calculated from the compression test of a small wall built with units and mortar layers. This will be discussed in detail in section 3.3. The relevant material properties are listed below.

- E_{unit} Elastic modulus of the masonry unit (positive);
- ν_{unit} Poison's ratio of the masonry unit;

- K_t Uni-axial constitutive array of the interface in tension;
- K_c Uni-axial constitutive array of the interface in compression;
- K_s Uni-axial constitutive array of the interface in shear;
- $K_{t,e}$ Elastic stiffness of the interface in tension (positive);
- $K_{c,e}$ Elastic stiffness of the interface in compression (positive);
- $K_{s,e}$ Elastic stiffness of the interface in shear (positive);
- $K_{t,so}$ Constant softening stiffness of the interface in tension (negative);
- $K_{c,so}$ Constant softening stiffness of the interface in compression (negative);
- $K_{s,so}$ Constant softening stiffness of the interface in shear (negative);
- $G_{f,t}$ Fracture energy of tension (positive);
- $G_{f,c}$ Fracture energy of compression (positive);
- $G_{f,s}$ Fracture energy of shear (positive);
- c Cohesion (initial shear strength) of the interface (positive);
- f_t Tensile strength of the interface (positive);
- f_c Compressive strength of the interface (positive);
- ϕ Friction angle of the interface (positive);
- w Damage factor of the crack due to the tensile and shear plastic loading;
- w_c Damage factor of crushing due to compressive plastic loading.

Note that K_t, K_c, K_s are the uni-axial constitutive arrays that comprise the coordinates (in terms of stress and relative-displacement) of the critical points of the uni-axial constitutive curves. Also note that $K_{c,so}$ (constant softening stiffness, compressive) will not be defined if the constitutive curve of the interface in compression is parabolic, as detailed in section 3.3.2, with a varying softening stiffness during the softening process.

It is important to realize that, throughout the entire loading process, the units in the mechanical model are always overlapped with the corresponding part of the units in the FE model (the parts that are not originally the mortar layer). Figure 3.2 can also give a hint. This property ensures that the FE model will have the same load-displacement relation with the mechanical model to simulate the real structural behaviour to some extent. And it is also very crucial for the derivation in the following sections.

For the neglected head joints, the properties are similar to the bed joints. They will also be modelled using zero-thickness interface elements with the same kind of properties shown above. The values of these properties for head joints are usually softer or lower due to the lack of pre-compression.

3.2. Properties of the units

In the context of masonry structures, the units could usually be one of the various kinds of bricks. As in both the detailed mechanical model and the discrete crack FE model, we assume a fully elastic behaviour of the unit, only elastic properties are needed for the plane stress elements modelling the brick.

Notice that because of the zero-thickness interface elements, in the FEM discrete crack model, the heights of the units should be adjusted to

$$h_{u,FEM} = h_u + \frac{h_{j,upper}}{2} + \frac{h_{j,lower}}{2} \tag{3.1}$$

where

h_u: height of the unit of the real structure;
$h_{j,upper}$: height (thickness) of the adjacent (mortar) joint of the real structure above that unit;
$h_{j,lower}$: height (thickness) of the adjacent (mortar) joint of the real structure beneath that unit.

This is to ensure that the moment distribution along the height of the FE model is consistent with the real structure.

3.2.1. Elastic properties

The elastic properties of the bricks are Young's modulus and Poisson's ratio.

The Young's modulus E_u, also called the elastic modulus, is usually obtained by a flexural strength test of a single masonry unit assuming a linear stress distribution over the height of the brick's cross-section.

The Poisson's ratio ν is obtained from the compressive test of the small masonry wall, built with mortar and masonry units. It is determined in the elastic phase as the ratio between the lateral strains, which are evaluated in the direction perpendicular to the loading one, and the normal strains. This value is used as a universal value for both the masonry units and the mortar. Although this is not that precise for a single unit, it could still be a good prediction especially for masonry structure as a whole.

The shear modulus G_u can be calculated with the Poisson's ratio ν and Young's modulus E_u.

3.3. Properties of the interfaces

The interface here means the zero-thickness interface element in the FEM model. Due to the simplification of the real joints with a certain thickness, as it is in the mechanical model, to this zero-thickness interface elements, it is important to determine the equivalent constitutive curves for the interface elements in each direction. This is to ensure that the overall mechanical behaviour of the FEM model is consistent with the detailed mechanical model as well as the real structure.

3.3.1. Elastic properties

Before discussing the entire constitutive curves, let us first focus on the elastic modulus of each direction. Consider the simple structure proposed in figure 3.1. For such a structure loaded elastically in shear at the top of the upper unit, the deformed shapes of the mechanical model and the FEM model are illustrated with orange solid line and red dashed line respectively in figure 3.2 below.

For elastic behaviour, the deformed shape of the FE model is not exactly the same as the detailed mechanical model that represents the real structure, because the interface element in the FE model is zero-thickness. As a result, each unit (plane stress element) of the FE model can be divided into two parts. One is with the height of h_u as the brick in the mechanical model. The other is with the height of $h_j/2$ as half of the mortar layer in the mechanical model. The so-called consistency of mechanical behaviour of these two models is, in essence, their identical load-displacement curve during the loading process. To achieve that, the former part of the unit (plane stress element) in the FE model with

the height of h_u should overlap with the brick in the mechanical model. The latter part of the unit in the FE model with the height of $h_j/2$ deforms differently from the mortar layer in the mechanical model, and therefore this difference should be compensated by the relative deformation in the zero-thickness interface element. Accordingly, the equivalent elastic stiffness of the zero-thickness interface is calculated.

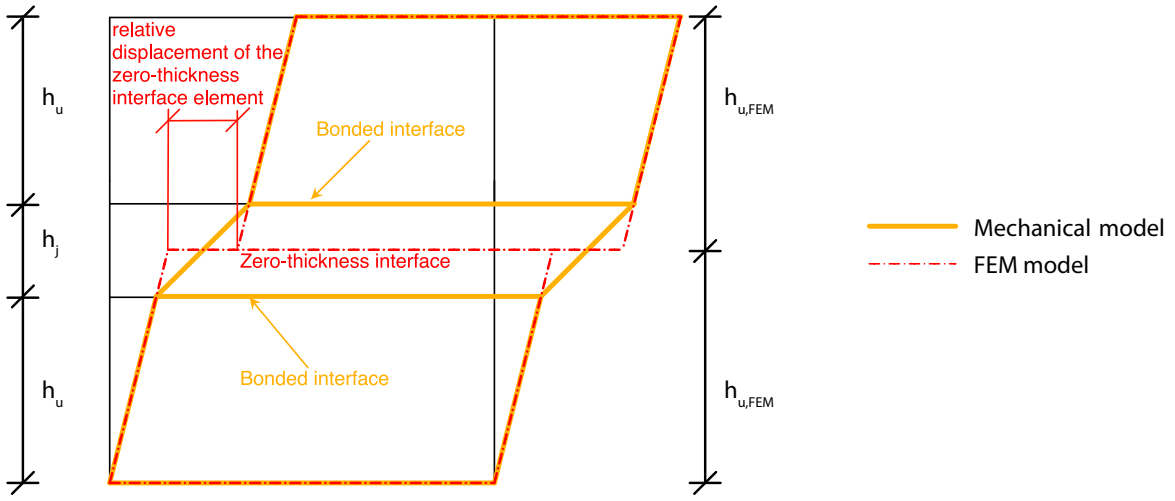

Figure 3.2: Detailed mechanical model loaded in shear (orange) and its FE model (red) before cracked

Given the same displacement at the cross-section of the bonded surface, the compatibility equation writes

$$h_j \frac{\tau}{G_u} + \frac{\tau}{K_{s,e}} = h_j \frac{\tau}{G_j} \tag{3.2}$$

where
$K_{s,e}$: elastic shear stiffness of the zero-thickness interface element;
h_j: height of the (mortar) bed joint;
τ: horizontal shear stress applied on the structure;
G_u: elastic shear modulus of the units;
G_j: elastic shear modulus of the mortar bed joint.

Eliminating the stress gives an equation of stiffnesses, which is

$$\frac{1}{K_{s,e}} = \frac{h_j}{G_j} - \frac{h_j}{G_u} \tag{3.3}$$

This equation also shows that this is just a problem of replacing the spring of the mortar bed joint by two springs in series, which are the spring of the interface element and the spring of the units. Finally, the equivalent stiffness of the zero-thickness interface element writes

$$K_{s,e} = \frac{G_u G_j}{(G_u - G_j)h_j} \tag{3.4}$$

And if the $G_u >> G_j$, we simplify the equation 3.4 to

$$K_{s,e} = \frac{G_j}{h_j} \tag{3.5}$$

The elastic shear modulus of the mortar bed joint G_j is usually obtained by a triplet test as figure 3.3 shows below.

However, if the shear modulus of the bed joint G_j cannot be directly obtained from an experiment, it could be also calculated from text of a small masnory shear wall with the overall shear elastic modulus G_m, with the equation below using spring theory in series.

$$\frac{h_j^t}{G_j} = \frac{h_j^t + h_u^t}{G_m} - \frac{h_u^t}{G_u} \tag{3.6}$$

where
h_j^t: total height of all the (mortar) joints with shear deformation, $h_j^t = n \times h_j$;
h_u^t: total height of all the units with shear deformation, $h_u^t = m \times h_u$;
n: number of the joint layers with shear deformation;
m: number of the unit layers with shear deformation;
h_j: average height of the joint layers;
h_u: average height of the unit layers;
G_m: equivalent elastic shear modulus of the whole structure under shear load.

Figure 3.3: Test set-up for shear-compression test on masonry specimen (Triplet test)[2]

Similarly, in normal direction, the compressive elastic stiffness $K_{c,e}$ and the tensile elastic stiffness $K_{t,e}$, assumed to be the same, could be determined by:

$$\frac{1}{K_{t,e}} = \frac{1}{K_{c,e}} = \frac{h_j}{E_j} - \frac{h_j}{E_u} \tag{3.7}$$

$$K_{t,e} = K_{c,e} = \frac{E_u E_j}{(E_u - E_j)h_j} \tag{3.8}$$

where E_u and E_j are the elastic modulus in normal direction of the units and the joints respectively. If $E_u >> E_j$, the equation can be simplified to

$$K_{t,e} = K_{c,e} = \frac{E_j}{h_j} \tag{3.9}$$

The elastic modulus of the joints E_j usually cannot be determined directly from the compressive test of a thin layer of mortar. Therefore, it needs to be calculated from the compressive test of a small masonry wall as figure 3.4 below. Also note that due to the lack of horizontal pre-compression during the construction of the masonry structure, the elastic modulus of the head joint is different from, usually less than, the one of the bed joint. Therefore, the compressive test of the masonry wall should be performed in both directions. Accordingly, there will be different normal stiffness of the interface elements representing the bed joints and head joints.

And the elastic modulus of the joints E_j can be calculated with

$$\frac{h_j^t}{E_j} = \frac{h_j^t + h_u^t}{E_m} - \frac{h_u^t}{E_u} \tag{3.10}$$

where
h_j^t: total height of all the (mortar) joints with compressive deformation, $h_j^t = n \times h_j$;
h_u^t: total height of all the units with compressive deformation, $h_u^t = m \times h_u$;
n: number of the joint layers with compressive deformation;
m: number of the unit layers with compressive deformation;
h_j: average height of the joint layers;
h_u: average height of the unit layers;
E_m: equivalent elastic modulus of the whole structure under compressive load.

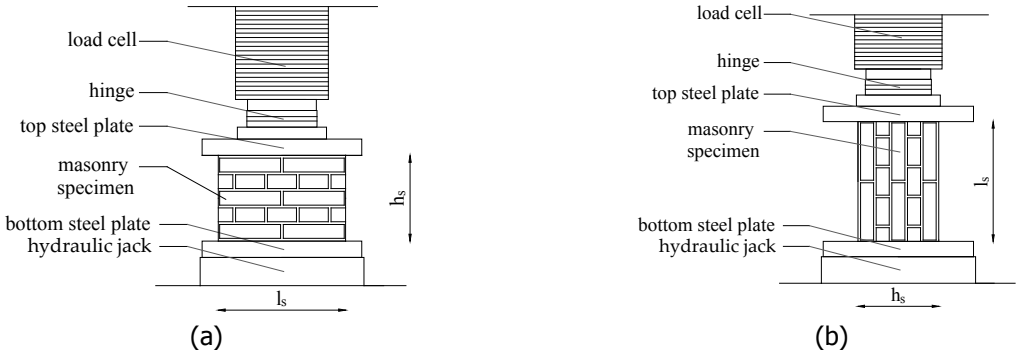

Figure 3.4: Compression test on masonry: (a) vertical configuration; (b) horizontal configuration [2]

Note that, for the head joints, the calculation is not that straightforward, because the layers of head joints are interrupted by the brick units in the vertical direction (3.4b). To calculate an equivalent compressive stiffness of the interface elements representing the head joints, one can calculate the equivalent stiffness for the head joints in each column of the vertical bricklayer, using the equation 3.10 and 3.8. And then calculate the average of the equivalent stiffnesses for all columns to be the final stiffness for the head-joint interface element.

3.3.2. Uniaxial constitutive curves

In this section, the constitutive curves for compression, tension and shear for the zero-thickness interface element in the simplified discrete crack model will be introduced.

3.3.2.1. Compression

Two compressive uni-axial constitutive curves are provided. The first one is a parabolic curve and the second one is a modified version of compressive curve adopted in the renowned Engineering Masonry Model.

The parabolic compressive curve is based on fracture energy, according to Feenstra [3], shown in figure 3.5 below. As the compressive behaviour is assumed to be decoupled from the shear stress state, all the compressive stresses can be calculated directly using this curve below, with any shear stress applied simultaneously on that integration point.

The user defined parameters for the parabolic compressive curve include:

- f_c: Compressive strength of interface element (positive)
- $G_{f,c}$: Compressive fracture energy of interface element under the softening branch (positive)

- $K_{c,e}$: Elastic compressive stiffness of interface element (positive)
- λ: Proportion of unloading and reloading with initial stiffness w.r.t. the entire unloading and reloading process (positive)

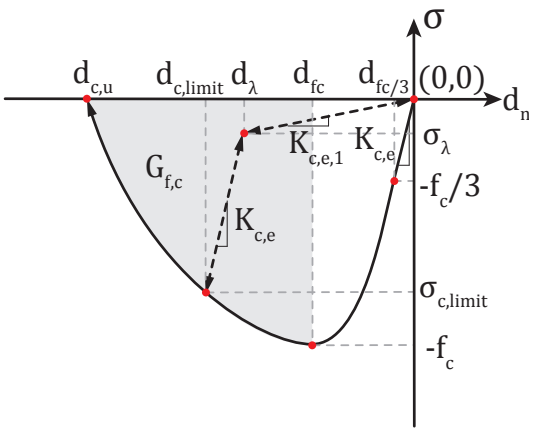

Figure 3.5: Parabolic compressive constitutive curve for the interface element in simplified FEM discrete crack model

In the algorithm of the constitutive model, the critical points illustrated using red dots in the figure will be logged in terms of coordinates in the array K_c for each integration point. They correspond to the origin, the linear elastic limit, the maximum compressive stress and ultimate relative displacement, respectively. The detailed implementation will be discussed in section 4.2. The horizontal coordinates of these critical points are

$$d_{fc/3} = -\frac{1}{3}\frac{f_c}{K_{c,e}} \tag{3.11}$$

$$d_{fc} = -\frac{5}{3}\frac{f_c}{K_{c,e}} = 5d_{fc/3} \tag{3.12}$$

$$d_u = \min\left(d_{fc} - \frac{3}{2}\frac{G_{f,c}}{f_c}, 2.5d_{fc}\right) \tag{3.13}$$

where $G_{f,c}$ is the compressive fracture energy denoted as the area in gray in figure 3.5. The overall curve can be calculated using the formulas below.

$$\sigma = \begin{cases} -f_c\frac{1}{3}\frac{d_n}{d_{fc/3}} & \text{if } d_{fc/3} < d_n \leq 0 \\ -f_c\frac{1}{3}\left(1 + 4\left(\frac{d_n - d_{fc/3}}{d_{fc} - d_{fc/3}}\right) - 2\left(\frac{d_n - d_{fc/3}}{d_{fc} - d_{fc/3}}\right)^2\right) & \text{if } d_{fc} < d_n \leq d_{fc/3} \\ -f_c\left(1 - \left(\frac{d_n - d_{fc}}{d_{c,u} - d_{fc}}\right)^2\right) & \text{if } d_{c,u} < d_n \leq d_{fc} \\ 0 & \text{if } d_n \leq d_u \end{cases} \tag{3.14}$$

The unloading and reloading behaviours follow the same bilinear black dashed line in figure 3.5. The bilinear line shows a combination of unloading and reloading with initial stiffness ($K_{c,e}$) and secant stiffness ($K_{c,e,1}$). Specifically, an unloading and reloading factor λ ($0 \leqslant \lambda \leqslant 1$) is defined such that $\lambda = 1$ corresponds to unloading to zero stress with the initial stiffness $K_{c,e}$ and $\lambda = 0$ corresponds to secant unloading to the origin with stiffness $K_{c,e,1}$. In the general case, the initial stiffness $K_{c,e}$ is applied until the compressive stress level $\sigma_\lambda = (1-\lambda) \times \sigma_{c,limit}$ is reached; then, a secant stiffness $K_{c,e,1}$ to the origin is followed. The reloading follows the same line as the unloading.

The modified Engineering Masonry Model compressive curve is assumed to consist of a sequence of a third-order curve, a parabolic curve up to the compressive strength f_c, and a linear softening curve shown with a black solid line in figure 3.6. The unloading and reloading behaviours are also defined by the bilinear line as same as the parabolic compressive curve, illustrated with black dashed lines. For the specific definition of the unloading and reloading process, please refer to the parabolic compressive curve. Moreover, the modification of this curve compared to the original compressive curve used in Engineering Masonry Model [14] is clearly in the reloading behaviour. According to the compressive test conducted on a small masonry wall[2], it is shown that reloading is more likely to follow the same curve as unloading with initial stiffness.

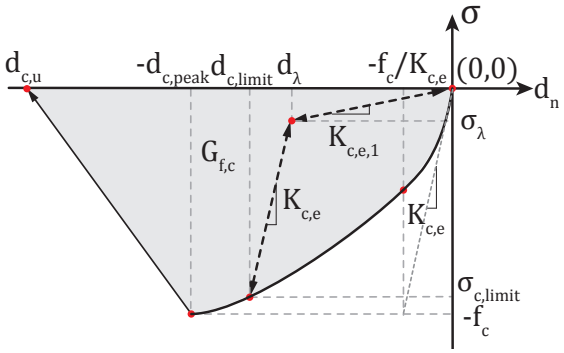

Figure 3.6: Modified Engineering Masonry model compressive constitutive curve for the interface element in simplified FEM discrete crack model

The user defined parameters for the modified Engineering Masonry Model compressive curve include:

- f_c: Compressive strength of interface element (positive)
- $G_{f,c}$: Compressive fracture energy of interface element under the entire curve (positive)
- $K_{c,e}$: Elastic compressive stiffness of interface element (positive)
- $d_{c,peak}$: Relative displacement corresponding to the compressive strength (positive)
- λ: Proportion of unloading and reloading with initial stiffness w.r.t. the entire unloading and reloading process (positive)

The ultimate relative displacement in compression is defined by fracture energy $G_{f,c}$ of interface element under the entire curve

$$d_{n,u} = -d_{c,peak} - \max\left[0, \frac{2G}{hf_c} - \frac{f_c}{A^2 K_{c,e}} - \frac{A+1}{A}\left(d_{c,peak} - \frac{f_c}{K_{c,e}}\right)\right] \tag{3.15}$$

The overall curve can be calculated using the formulas below:

$$\sigma = \begin{cases} B_2\left[\frac{K_{c,e}d_n}{f_c}\right]^3 - B_3\left[\frac{K_{c,e}d_n}{f_c}\right]^2 + K_{c,e}d_n & \text{for } -\frac{f_c}{K_{c,e}} \le d_n < 0 \\ \left(\frac{A-1}{A}\left(\frac{K_{c,e}\left(d_{c,peak}+d_n\right)}{K_{c,e}d_{c,peak} - f_c}\right)^2 - 1\right)f_c & \text{for } -d_{c,peak} \le d_n < -\frac{f_c}{K_{c,e}} \\ \frac{-d_n + d_{c,u}}{d_{c,peak} + d_{c,u}} f_c & \text{for } d_{c,u} \le d_n < -d_{c,peak} \\ 0 & \text{for } d_n < d_{c,u} \end{cases} \tag{3.16}$$

where the constants B_2, B_3 and A can be calculated by:

$$B_2 = \left(\frac{A-2}{A} + 2\frac{A-1}{A}\frac{f_c}{K_{c,e}d_{c,peak} - f_c}\right)f_c \tag{3.17}$$

$$B_3 = \left(\frac{3-2A}{A} - 2\frac{A-1}{A} \frac{f_c}{K_{c,e} d_{c,peak} - f_c} \right) f_c \tag{3.18}$$

$$A = \left(\frac{K_{c,e} d_{c,peak}}{f_c} \right)^{\frac{1}{3}} \tag{3.19}$$

The main difference between these two compressive curves is that, for the parabolic curve, relative displacement corresponding to the compressive stress is fixed given a $K_{c,e}$, while it is more flexible for the modified Engineering Masonry Model compressive curve to allow the user to define a greater relative displacement $d_{c,peak}$ for a more ductile hardening process. If $d_{c,peak}$ is relatively small, then both curves perform similarly. In the current study, it is found that the relative displacement corresponding to the compressive strength is relatively a greater value than the parabolic curve, so the modified Engineering Masonry Model compressive curve is recommended. For the value of $d_{c,peak}$, please refer to chapter 6. In addition, please note that the compressive fracture energy $G_{f,c}$ is defined differently for these two curves. Therefore the value used in the parabolic curve should be usually smaller than that of the modified Engineering Masonry Model compressive curve.

Last but not least, although the compressive stress is decoupled with the shear stress, this model still assumes that the shear stress is coupled with the compressive stress. Therefore, the maximum shear stress that the interface element can carry still depends on the normal stress applied on that integration point of that interface.

3.3.2.2. Tension

The uni-axial tensile behaviour is also based on fracture energy, as shown in figure 3.7. The unloading and reloading in tension follow the dashed line with slope equal to the secant stiffness $K_{t,e,1}$ in the figure. Since the tension behaviour and the shear behaviour are coupled with each other in terms of maximum capacity and damage, this curve is only valid for uni-axial tensile cases. For the cases where both shear and tension are applied on the interface, some modifications must be made to be consistent with the Mohr-Coulomb Criterion. This is discussed in detail in section 3.3.3.

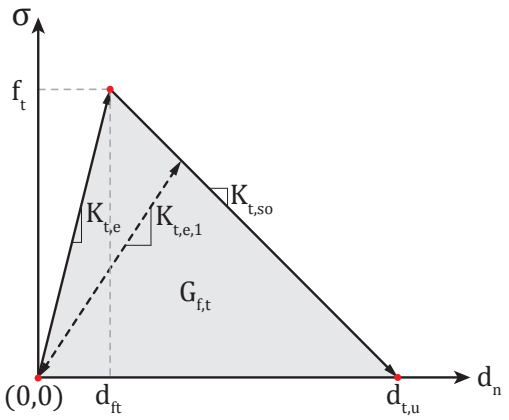

Figure 3.7: Tensile constitutive curve for the interface element in simplified FEM discrete crack model

The user defined parameters for the bilinear tensile curve includes:

- f_t: Tensile strength of interface element (positive)
- $G_{f,t}$: Tensile fracture energy of interface element under the entire curve (positive)
- $K_{t,e}$: Elastic tensile stiffness of interface element (positive)

Similarly, the red dots on the constitutive curve are also logged in the array K_t for other use in the algorithm. They are basically the coordinates of all turning points on the curve. The horizontal coordinates are

$$d_{t,u} = \frac{2G_{f,t}}{f_t} \tag{3.20}$$

$$d_{ft} = \frac{f_t}{K_{t,e}} \tag{3.21}$$

where $G_{f,t}$ is the tensile fracture energy defined by the user. And as the softening behaviour is assumed to be linear, the tensile softening stiffness can be determined as below.

$$K_{t,so} = \frac{f_t}{d_{t,u} - d_{ft}} \tag{3.22}$$

Figure 3.7 can also be expressed using formulas below.

$$\sigma = \begin{cases} K_{t,e} d_n & \text{if } 0 \leq d < d_{ft} \\ f_t + K_{t,so}(d_n - d_{ft}) & \text{if } d_{ft} \leq d < d_{t,u} \\ 0 & \text{if } d_{t,u} \leq d \end{cases} \tag{3.23}$$

3.3.2.3. Shear

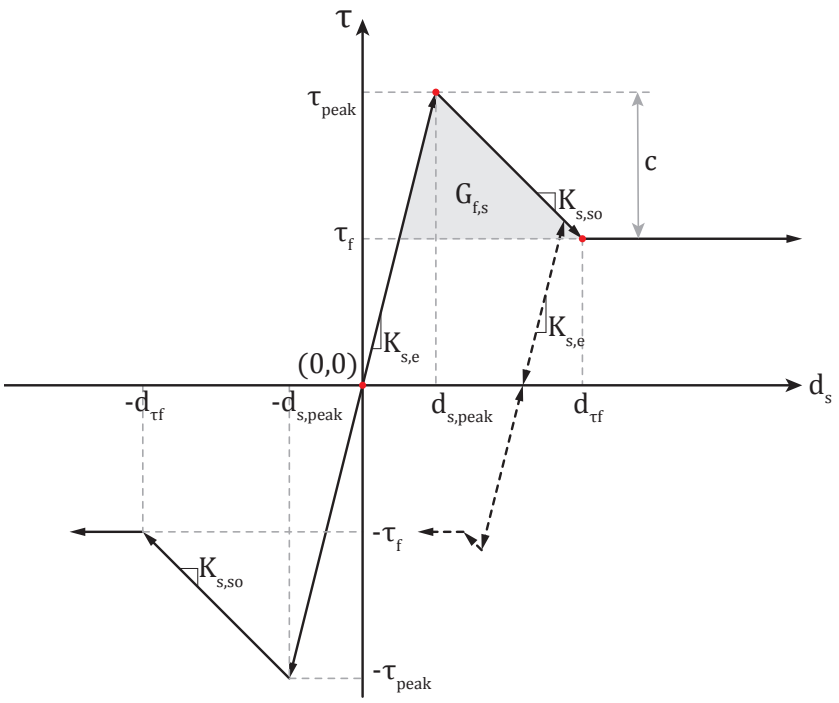

Figure 3.8: Shear constitutive curve for the interface element in simplified FEM discrete crack model

Finally, the shear behaviour is also based on fracture energy, as shown in figure 3.8. Different from the constitutive curve in normal direction, the shear unloading and reloading always follow the initial shear stiffness $K_{s,e}$, as shown with dashed lines in the figure. This curve is valid for pure shear and

the combination of shear and compression. For the situation when the interface is under tension and shear, some modification is needed to be consistent with the Mohr-Coulomb Criterion. Please refer to section 3.3.3.

The user defined parameters for the multi-linear shear curve includes:

- c: Cohesion (initial shear strength) of interface element (positive)
- $G_{f,s}$: Shear fracture energy of interface element contributed by cohesion (positive)
- $K_{s,e}$: Elastic shear stiffness of interface element (positive)
- ϕ: Friction angle of the interface (positive angular degree)

According to the Mohr-Coulomb Criterion, the maximum shear strength of the interface under a certain compressive load can be determined with the formula below. The shear resistance is composed by the cohesion c and the friction τ_f. If the interface is under shear and tension, the constitutive curve will be further modified in chapter 3.3.3.

$$\tau_{peak} = -\sigma_n \times tan\phi + c \tag{3.24}$$

The shear resistance due to the surface friction is:

$$\tau_f = -\sigma_n \times tan\phi \tag{3.25}$$

Similar to the normal direction, all the turning points, marked with red dots in figure 3.8, in the positive shear direction are logged in the array K_s for other use in the algorithm. More information can be found in section 4.2. Their horizontal coordinates are

$$d_{s,peak} = \frac{\tau_{peak}}{K_{s,e}} \tag{3.26}$$

$$d_{\tau f} = d_{s,peak} + \frac{2G_{f,s}}{c} - \frac{c}{K_{s,e}} \tag{3.27}$$

Moreover, as the softening behaviour in shear direction can also be assumed to be linear, the softening stiffness, which is negative, can be calculated as follows.

$$K_{s,so} = \frac{c}{d_{\tau f} - d_{s,peak}} \tag{3.28}$$

where $G_{f,s}$ is the shear fracture energy defined by the user. The constitutive curve in figure 3.8 can be written in terms of formulas below.

$$\tau = \begin{cases} d_s K_{s,e} & \text{if } 0 \le |d_s| \le d_{s,peak} \\ \frac{d_s}{|d_s|}\tau_{peak} + (d_s - d_{s,peak})K_{s,so} & \text{if } d_{s,peak} < |d_s| \le d_{\tau f} \\ \frac{d_s}{|d_s|}\tau_f & \text{if } d_{\tau f} < |d_s| \end{cases} \tag{3.29}$$

3.3.2.4. Summary

The uni-axial constitutive curves discussed in this section are the foundation of the coupling effect that will be introduced in the following sections. An important idea of this constitutive model is to load the pair of relative displacements on the integration point in the normal direction first, and then in the shear direction. Depending on the original stress state and the increments of relative displacements, the coupling effect introduced in the following sections will determine how the uni-axial constitutive curves in normal and shear directions can be used for plastic loading. Of course, for elastic loading, unloading and reloading that happen within the yield surface, these uni-axial curves can be used directly to update the stresses.

3.3.3. Coupling of normal and shear loading

This constitutive model has three assumptions that determine how and to what degree the shear and normal direction are coupled. They are listed as follows.

- The incremental displacements in normal and shear directions are applied sequentially instead of simultaneously to calculate the corresponding tractions in normal directions, for the sake of simplicity. This is discussed in detail in section 3.5.
- The model is based on the multi-surface failure criterion that includes the Mohr-Coulomb criterion, which means the stress state in normal direction will influence the stress capacity in the shear direction and vice versa. This section will discuss the details of this criterion.
- The model assumes a fully coupled behaviour between loss of cohesion in shear direction and the loss of tensile strength in normal direction, which means they decade with the exact same rate (in terms of proportion).

The multi-surface failure criterion that includes tensile, compressive and shear failure is illustrated in figure 3.9. The interface degrades in tension and shear with softening, as shown in the uni-axial tensile and shear constitutive curves (figure 3.7 and 3.8). And it degrades in compression with firstly hardening and then softening, as shown in the parabolic compressive curve or modified Engineering Masonry Model compressive curve (figure 3.5 or 3.6). Specifically, the softening in tension and shear results in shrinking of the yield surface to the origin. The compression cut-off moves left first because of the hardening, and then moves right for the following softening.

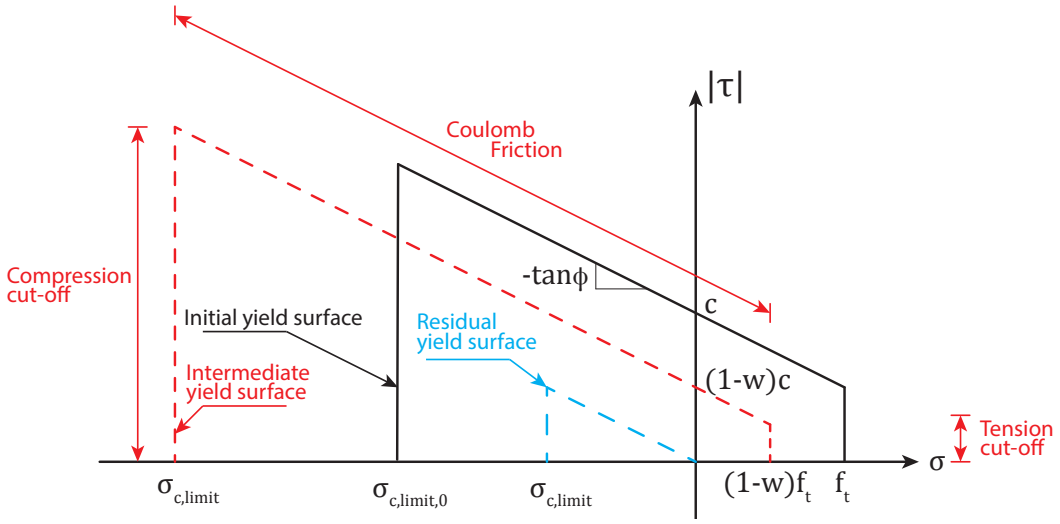

Figure 3.9: Multi-surface plasticity criterion for interface elements

Figure 3.9 can also be expressed with three yield functions below.

$$\begin{cases} f_1 = |\tau| + \sigma \times tan\phi - c(1-w) \\ f_2 = \sigma - (1-w)f_t \\ f_3 = \sigma_{c,limit} - \sigma \end{cases} \tag{3.30}$$

where
w: the damage factor of cracking caused by tension and shear softening, with initial value equal to 0. $0 \leq w \leq 1$;
w_c: the damage factor of crushing caused by compression, with initial value equal to 0. $0 \leq w_c \leq 1$ and w_c will remain 0 during the hardening and increases to 1 during softening;

$\sigma_{c,limit}$: elastic limit of compressive stress. If the interface is intact in compression, for parabolic compressive curve, the initial value $\sigma_{c,limit,0} = -f_c/3$. For modified Engineering Masonry Model compressive curve, $\sigma_{c,limit,0} = 0$. The value of $\sigma_{c,limit}$ is updated and marked as a special point in the uni-axial compressive constitutive array after each plastic loading process. The constitutive arrays will be introduced in table 4.1 and 4.2 in section 4.1 as a numeric representative of the uni-axial constitutive curves.

All the stress states (combinations of σ and τ) should be on or within the yield surfaces such that the values of function f_1, f_2 and f_3 satisfy

$$f_1 \leq 0, \quad f_2 \leq 0, \quad f_3 \leq 0 \tag{3.31}$$

During the plastic loading, the nonlinear effect leads to the evolution of the yield surfaces as a result of softening or hardening. The softening of tension and shear is reflected by a damage factor w and the softening of compression is shown with w_c. In this constitutive model, we assume that the damage in tension and shear is fully coupled such that the tensile strength and the cohesion reduce with same rate and finally reach 0 simultaneously. This is reflected in the equation 3.30 that both f_1 and f_2 use same damage factor w. Also, the tensile stress can affect the maximum shear stress capacity of the interface and vice versa through the Mohr-Coulomb yield surface in figure 3.9. In contrary to the mutual influence between tension and shear, the damage of compression and shear are only one-way correlated. Only the change in the compressive stress can affect the maximum shear stress capacity of the interface while the change of shear stress does not influence the maximum compressive stress capacity.

As the damage due to tension and shear softening is fully coupled, it is important to discuss the way to achieve plastic loading that keeps the calculated stress state always on the yield surfaces while the yield surfaces are shrinking at the same time. Hereby two plastic calculation processes are introduced as the core of this constitutive model.

- The first process is the non-iterative uni-axial plastic loading process in normal direction and shear direction. They are used in a sequential way: normal direction first, then shear direction. It is discussed in the following of this section with two Coupling Options.
- The second process is the iterative algorithm to calculate extra damage caused by the uni-axial plastic loading process in shear or normal direction. It will be introduced in section 3.4.

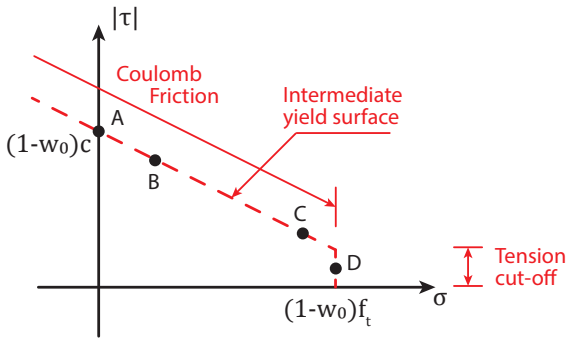

Figure 3.10: Illustration of four possible stress states after last loading process

For a more straightforward demonstration of the first process, assume that there are four stress states as shown in figure 3.10, namely A, B, C and D, which are already on the yield surface. Given the multi-surface failure criterion has limited the maximum stress in one direction given the stress in the other direction, the following paragraph will explain the assumption made to further plastically load the interface (integration point) in tension when the original stress states are A, B and D, and to plastically

load the interface in shear when the original stress states are C and A. Accordingly, two Coupling Options are proposed to determine the corresponding increase of damage factor and reduction of stress. The first option is to determine the increase of damage based on the increment of plastic relative displacement. In the second option, the increase of the damage is based on the fictitious reduction of stress.

Note that w_0 and $w_{c,0}$ are used to represent the damage factors of the previous update and w_1 and $w_{c,1}$ are the damage factors obtained from current update.

3.3.3.1. Option 1

For the option 1, two principles are assumed as below:

1. The softening stiffness is preserved when calculating the current stress value, however, the ultimate relative-displacement changes.

2. The amount of damage is calculated based on the increment of plastic relative-displacement.

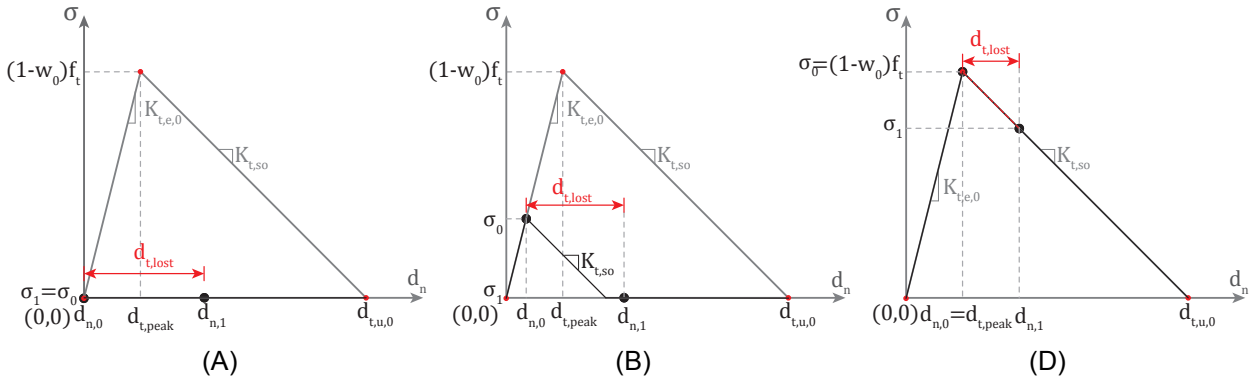

Figure 3.11: Plasticity loading process in tension of option 1

where
$d_{n,0}$: the total relative normal displacement of the last update;
$d_{n,1}$: the total relative normal displacement of the current update;
σ_0: the total normal (tensile) stress of the last update;
σ_1: the total normal (tensile) stress of the current update;
$K_{t,e,0}$: the (softened) elastic tensile stiffness of the last update;
$K_{t,so}$: the (softened) elastic tensile stiffness of the last update;
$d_{t,lost}$: the increment of plastic relative displacement in tension. $d_{t,lost} = d_{t,1} - d_{t,0} \geq 0$.

And the current damage factor w_1 shared between tension and shear is determined with

$$w_1 = min(w_0 + \frac{d_{t,lost}}{f_t/K_{t,so}}, 1) \tag{3.32}$$

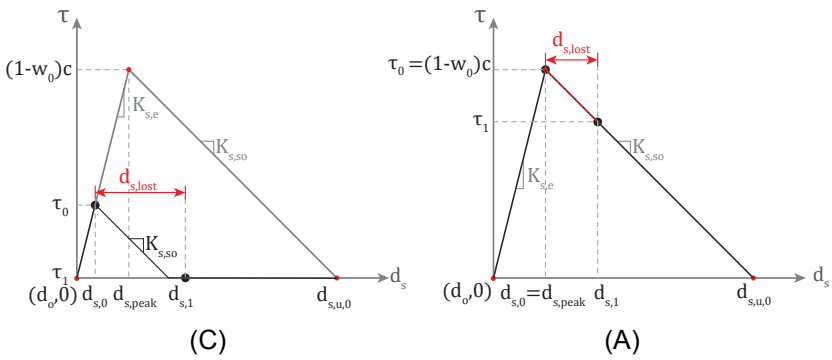

Figure 3.12: Plasticity loading process in shear of option 1

where
$d_{s,0}$: the total relative shear displacement of the last update;
$d_{s,0}$: the total relative shear displacement of the current update;
τ_0: the total shear stress of the last update;
τ_1: the total shear stress of the current update;
$K_{s,e,0}$: the (softened) elastic shear stiffness of the last update;
$K_{s,so}$: the (softened) elastic shear stiffness of the last update;
$d_{s,lost}$: the incremental plastic relative displacement in shear. $d_{s,lost} = d_{s,1} - d_{s,0} \geq 0$.

And the current damage factor w_1 shared between tension and shear is determined with

$$w_1 = min(w_0 + \frac{d_{s,lost}}{c/K_{s,so}}, 1) \tag{3.33}$$

3.3.3.2. Option 2

For the option 2, two principles are assumed as below:

1. The the ultimate relative-displacement $d_{s,u,0}$ of the last update is preserved. Accordingly, two special stiffness, namely $K_{t,path}$ and $K_{s,path}$, connecting the stress state of the last update to the stress state where stress drops to zero are introduced. The reduced stress in either tension or shear direction is determined with these two stiffness.
2. The amount of damage is calculated based on the fictitious reduction of stresses w.r.t. the fictitious peak stress σ_{peak}.

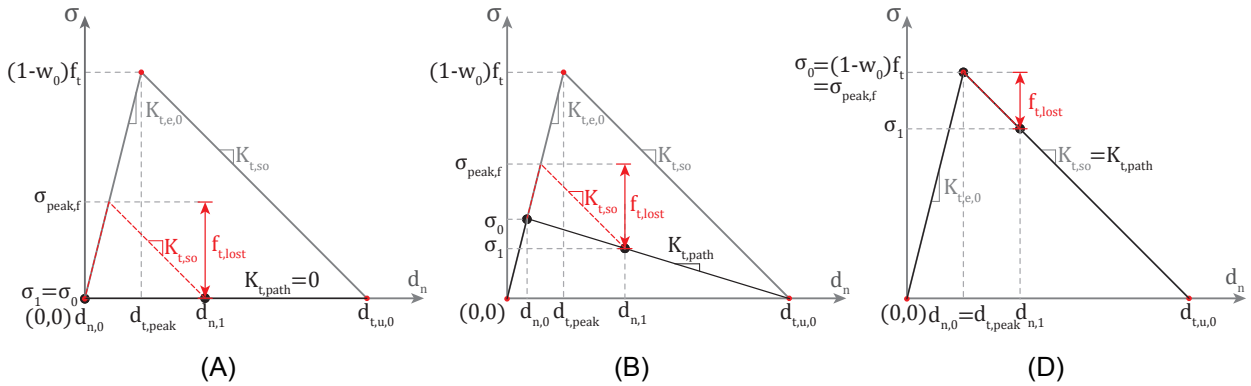

Figure 3.13: Plasticity loading process in tension of option 2

where
$K_{t,path}$: slope of the plastic loading path which connecting tensile stress state of the last update to the ultimate stress state where stress is equal to 0. $K_{t,path} = \sigma_0/(d_{t,0} - d_{t,u,0})$;
$\sigma_{peak,f}$: fictitious tensile stress at the intersection between the elastic branch of the uniaxial tensile curve and the extended line from the updated tensile stress state with the slope of the tensile softening stiffness;
$f_{t,lost}$: the amount of reduction of tensile stress. $f_{t,lost} = \sigma_{peak,f} - \sigma_1$.

Note that if the $d_{n,1}$ is larger than $d_{t,u,0}$, σ_1 is set to be 0. And the current damage factor w_1 shared between tension and shear is determined with

$$w_1 = w_0 + \frac{d_{s,lost}}{f_t} \tag{3.34}$$

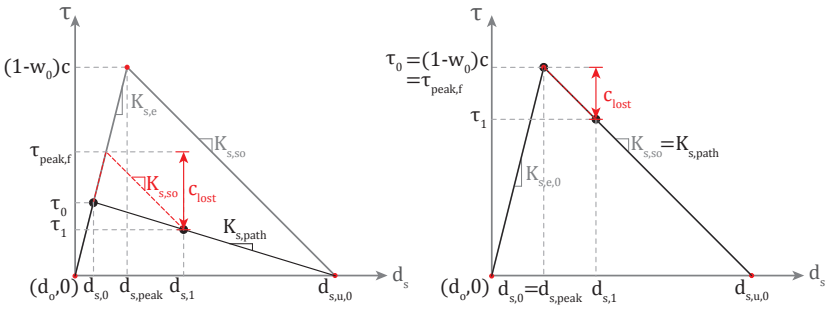

Figure 3.14: Plasticity loading process in shear of option 2

where
$K_{s,path}$: slope of the plastic loading path which connecting shear stress point of the last update to the ultimate stress point where stress is equal to $max[0, (1-w_0)c-\sigma_1 tan(phi)] = 0$. $K_{s,path} = \tau_0/(d_{s,0}-d_{s,u,0})$;
$\tau_{peak,f}$: fictitious shear stress at the intersection between the elastic branch of the uniaxial shear curve and the extended line from the updated shear stress state with the slope of the shear softening stiffness;
$f_{t,lost}$: the amount of reduction of shear stress. $c_{lost} = \tau_{peak} - \tau_1$.

And the current damage factor w_1 shared between tension and shear is determined with

$$w_1 = w_0 + \frac{c_{lost}}{c} \tag{3.35}$$

3.3.3.3. Summary

In conclusion, for plastic shear loading at stress state A and plastic tensile loading at stress state D, Option 1 and Option 2 are exactly the same. For the other stress states, the stress updated with Option 1 is always lower than Option 2. Option 1 also returns a higher value of increment of damage than Option 2. However, do not mistakenly conclude that Option 2 is less conservative. Option 2 only seems to be less conservative after this uni-axial plastic loading calculation (process one), but it might actually result in more damage and a lower stress value after the iterative extra damage calculation (process two), which will be discussed in the verification section on integration point level (section 5.2).

Furthermore, in this section, the Coupling Options are discussed for the coupling between shear and tension. For the one-way coupling between shear and compression, these Coupling Options will also

be used to calculate the shear stress, whereas the compressive stress will be calculated directly through the uni-axial constitutive curve introduced in section 3.3.2. This is because the maximum shear stress will be influence by the compressive stress based on the Coulomb friction criterion; however, in the other way around, the maximum compressive stress is independent of the shear stress. For calculating shear stress and shear damage based on given compressive strength, both Coupling Option 1 and Coupling Option 2 are exactly the same, which yield identical result through identical calculation procedure, because initial shear stress on the yield surface is always equal to the maximum shear stress $(1 - w_0)c - \sigma_1 tan(\phi)$ and it will soften with the original softening stiffness. This is similar to the plastic loading at stress state A.

More importantly, one should notice that the stress value from the uni-axial plastic loading calculation (process one) in a direction might not be the final stress value. This is because there are usually cases where the softening in one direction reduces the stress capacity in the other direction such that the latter direction cannot even carry its original stress. This means that the currently updated stress state from process one is actually out of the yield surface and its not yet the correct final stress value. In this case, more damage will be triggered, and the extra damage calculation (process two) is hereby proposed to calculate the correct final stress state. This will be discussed in detail in the next section 3.4.

3.4. Extra damage calculation

In the previous section, we defined the way to calculate the reduced stress and the amount of damage uni-axially. The procedure is that the maximum tensile capacity is first calculated according to the Mohr-Coulomb Criterion with the shear stress from the previous update. Then, with the increment of relative normal displacement applied, either Option 1 or Option 2 is used to calculate the new normal stress and update the damage factor. However, before repeating the same procedure for shear direction, an additional step is taken to check, given the new damage factor shared between tension and shear, if that integration point is still able to take the original shear stress according to the Mohr-Coulomb Criterion. If it cannot, an additional process is needed to calculate the extra damage caused by this gap between shear load and shear capacity. This process, mentioned as process two in the last section, is derived and formulated in this section.

To be more general, the unloading in compression, softening in compression or tension, or just elastic loading in tension might make that integration point unable to carry its original shear stress. And before the current incremental relative shear displacement of the interface is applied, the original shear stress of the last step might be already larger than the shear capacity. Therefore, an extra amount of shear softening might occur in order to reach a new equilibrium between the shear load and the shear capacity, in other words, the external shear force applied on the interface and the internal shear force of the interface.

A similar situation also exists after elastic loading in shear or softening in shear. The tensile capacity reduces, according to the current shear stress. And if the tensile capacity is not able to carry the tensile stress, and damage in tension will occur before applying the current increment of relative displacement in normal direction. All these influences of one direction on the other direction can repeat like a loop until no more new damage can occur anymore. These loops determine that the calculation should be iterative.

Note that in the model, the loading or softening in shear is assumed to be decoupled from the capacity in compression. Also note that all the above-mentioned damage only occurs for plastic loading taking both directions into account instead of any elastic process. This could be identified using an elastic predictor and the Mohr-Coulomb criterion. This will be further discussed in section 4.3.

Although these cases seem to be complicated and interconnected, essentially they all lead to two problems, which are also similar to each other. They are listed below:

1. How much cohesion will be lost if the maximum shear capacity, determined by Mohr-Coulomb Criterion, is not able to resist the shear stress of the last update? What will be the residual shear stress after this cohesion loss?
2. How much tensile strength will be lost if the maximum tensile capacity, determined by Mohr-Coulomb Criterion, is unable to resist the tensile stress of the last update? What will be the residual tensile stress after this strength loss?

Let us focus on problem one first. Again, consider the simple mechanical model composed of two units and a mortar joint as it has been introduced in figure 3.1. Assume that in the previous step, the structure has been loaded until the crack is partially developed, just as its mechanical model shows with green solid line in figure 3.15. The blue dashed line shows the corresponding deformation of the FE discrete crack model with a zero-thickness interface element representing the entire joint. The shear stress of the FE model is τ_0 at that moment. This stress state and the loading history of that step are also illustrated on the constitutive curve on the left plot of figure 3.16 with black lines. Note that the horizontal axis represents the relative displacement of the interface element in the FE model.

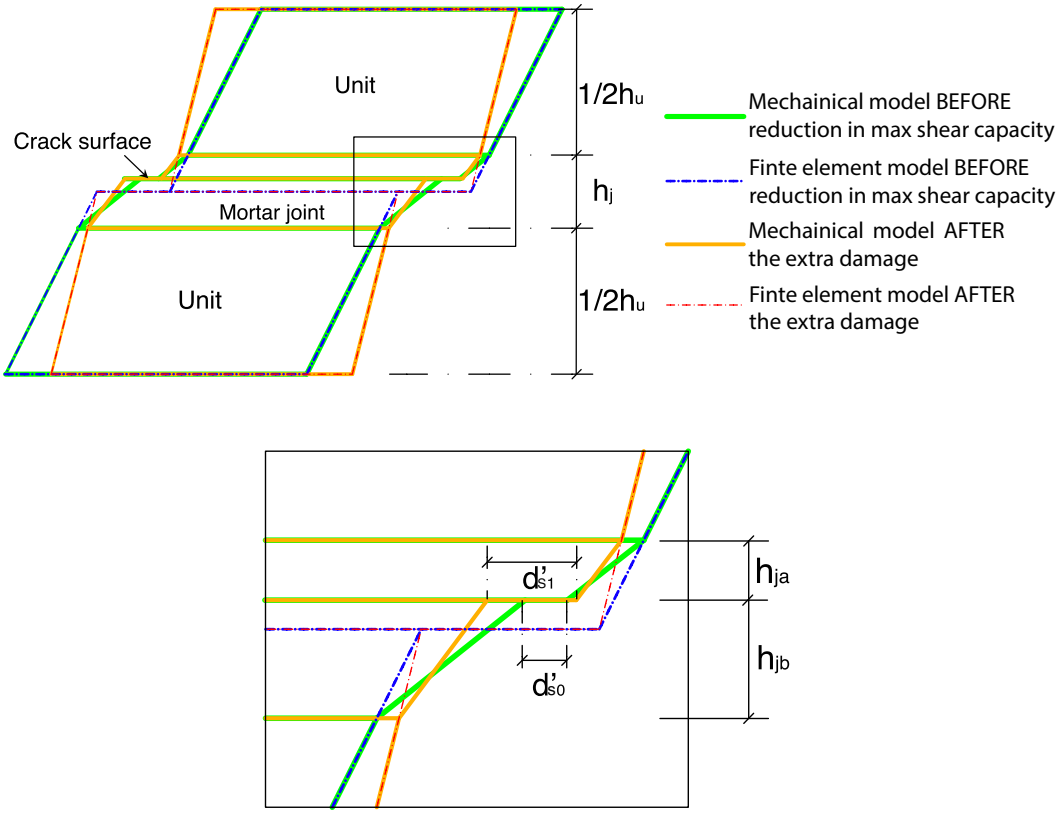

Figure 3.15: Illustration of the extra damage process of the partially cracked mechanical model and FE model

Then, the application of the current increment of relative normal displacement reduces the maximum shear capacity of the interface element. Also, if the current increment of relative displacement in shear direction will not reduce the original shear stress τ_0 to a value that is lower than the reduced maximum shear capacity, then it is a plastic loading and the crack will further develop. Assume that after the application of the increment of relative displacement in normal direction, the maximum shear capacity of the interface reduces to τ_{max}, which is less than the original τ_0. At this moment, the relative displacement in shear direction of the interface element (red dashed line) should be the same as the previous step (blue dashed line), as shown in the middle of figure 3.15, because the constitutive model is to return the stress value corresponding to the provided relative displacement. However, the internal shear stress of the interface element in the current step must be less than that of the previous step, that

is why the plane stress element representing the units of the current step (red dashed line) rebound a little bit compared with its original shape (blue dashed line). This is to reach a new equilibrium between the internal force of the plane stress element and the external force applied by the interface element to the plane stress element. In other words, for the interface, a new equilibrium between the internal force of the interface element and the external force applied by the plane stress element to the interface element will be formed.

During this rebound process, a certain amount of additional softening must have taken place. To calculate the reasonable value of softening and the shear stress after that softening, we need to look back to the rather detailed mechanical model. The deformed shape of the mechanical model after the softening is plotted with orange solid line in the scaled figure. We can see that clearly the relative displacement of the crack is now increase to $d'_{s,1}$ from $d'_{s,0}$, which is illustrated in the lower plot of figure 3.15. Given that the relative shear displacement of the interface element does not change and the overlapping properties of the units between mechanical model and FE model, which has been discussed at the end of section 3.1, the value of $d'_{s,1}$ can be calculated using the geometrical compatibility equation as follow:

$$d'_{s,1} = d'_{s,0} + \frac{\tau_0}{G_j}h_j - \frac{\tau_0}{G_u}h_j + \frac{\tau_{1,e}}{G_u}h_j + \frac{\tau_{1,e}}{G_j}h_j \tag{3.36}$$

where

$d'_{s,1}$: the relative displacement of the cracked surface in shear direction in the mechanical model after the additional softening;
$d'_{s,0}$: the relative displacement of the cracked surface in shear direction in the mechanical model before the additional softening;
$\tau_{1,e}$: the elastic shear stress in the intact mortar layer during the rebound process of the additional softening;
τ_0: the shear stress before the additional softening;
G_u: the shear modulus of the unit in the mechanical model;
G_j: the shear modulus of the mortar joint in the mechanical model;
h_j: the total height of the mortar joint in the mechanical model.

Note that all the stresses are the same for both the mechanical model and the FE model.

Combined with the equation 3.3, equation 3.36 can be further simplified to

$$\Delta d'_s = d'_{s,1} - d'_{s,0} = h_j(\frac{1}{G_u} - \frac{1}{G_j})(\tau_{1,e} - \tau_0) = -\frac{1}{K_{s,e}}(\tau_{1,e} - \tau_0) \tag{3.37}$$

where

$\Delta d'$: the increment of the relative displacement of the cracked surface in the mechanical model;
$K_{s,e}$: the elastic stiffness of the zero-thickness interface element in FE model in shear direction.

The above equation indicates the relation between the shear stress in the intact mortar layers and the increment of the relative displacement of the cracked surface during the rebound process. The internal shear stress in the intact mortar layers is also the external shear stress applied on the cracked surface. Now we need another equation to relate the internal shear stress of the cracked surface during its softening process to the increment of the relative displacement of that surface. That is:

$$\tau_{1,so} = max(\tau_{max} + K'_{s,so}\Delta d'_s, \tau_f) \tag{3.38}$$

where

$K'_{s,so}$: the softening stiffness of the cracked surface in mechanical model in shear direction (negative). Its value can be calculated using equation A.3 derived in appendix A;
$\tau_{1,so}$: the shear stress in the cracked surface during the additional softening;
τ_{max}: the shear stress capacity after the increase of stress or softening in normal direction, according to the Mohr-Coulomb Criterion;

$$\tau_{max} = -tan\phi \times \sigma_0 + c * (1 - w_0)$$

w_0: damage factor of the crack caused by shear and tension before the additional softening, $0 \leq w_0 \leq 1$.
τ_f: the shear stress caused by the coulomb friction, which is positive in compression and 0 in tension ($\tau_f = max(-tan\phi \times \sigma_1, 0)$);
σ_1: the normal stress on the cracked surface;
ϕ: friction angle of the interface (positive).

The equation 3.37 and 3.38 are plotted in figure 3.16 in blue and green respectively.

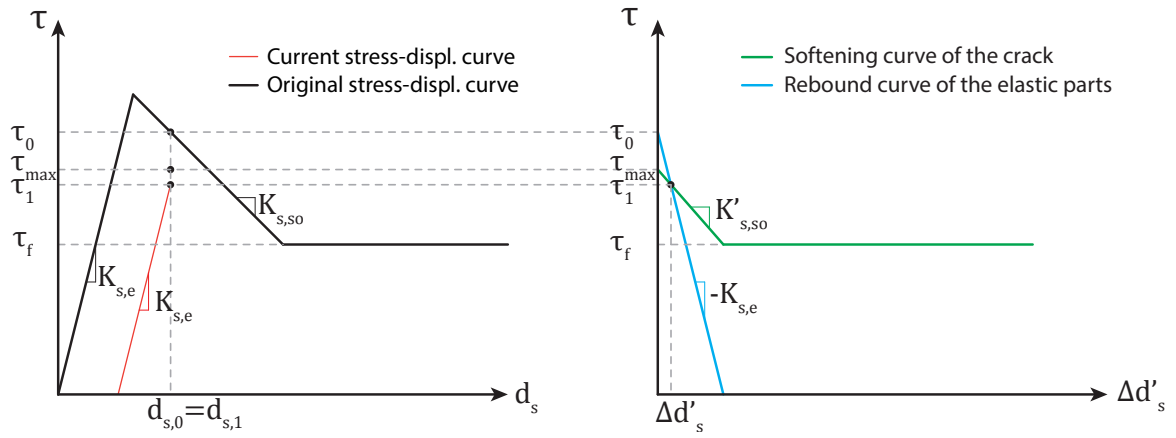

Figure 3.16: Relation between amount of softening at the interface element and the relative displacement of the real crack in shear

Known that the internal and the external stresses of the cracked surface must be equal to each other,

$$\tau_{1,so} = \tau_{1,e} = \tau_1 \tag{3.39}$$

τ_1 can therefore be calculated as the intersection of these two lines. This can be solved by combined these two equations (3.37 and 3.38). Further combined with equation A.3, τ_1 can be written as

$$\tau_1 = max(\tau_0 - (1 - \frac{K_{s,so}}{K_{s,e}})(\tau_0 - \tau_{max}), \tau_f) \tag{3.40}$$

where τ_1 is the shear stress in the current step after the additional softening (extra damage). And the cohesion lost accordingly is

$$c_{lost} = \tau_{max} - \tau 1 \tag{3.41}$$

Therefore, the damage parameter w which reflects the development of the crack shared between shear and tensile can be updated as:

$$w_1 = w_0 + \frac{c_{lost}}{c} \tag{3.42}$$

where

w_0: damage parameter in shear and tensile directions before the additional softening;
w_1: damage parameter in shear and tensile directions after the additional softening;
c_{lost}: amount of cohesion lost due to the softening in shear direction;
c: original intact cohesion (initial shear strength).

At this moment, the residual cohesion and tensile strength write

$$c_r = c * (1 - w_1) \tag{3.43}$$

$$f_{t,r} = f_t * (1 - w_1) \tag{3.44}$$

Looking back to the left side of figure 3.16, the point with shear stress equal to τ_1 shows the stress state after the additional softening process. The red line indicates the path if the interface is unloaded in the future with initial shear elastic stiffness. The constitutive curve if the structure is further loaded in shear is not plotted in this figure. This will be discussed in detail in section 4.2.

Up to here, we solve the first problem. The second problem regarding the additional softening (extra damage) in tensile direction is actually very similar to the one of the shear direction. We assume that the tensile softening and the shear softening share the same crack. And in tension, the crack also develops in the same ways as it does in shear. For instance, the plastic deformation in tension also concentrated at the cracked surface in the detailed mechanical model, as is introduced in figure 3.1. The increase of shear stress or softening in shear direction also induces the reduction of maximum tensile stress capacity. If the maximum tensile capacity is unable to carry the tensile stress from the last update and the current increment of relative tensile displacement will not reduce the tensile stress to a level lower than this maximum tensile capacity, additional softening (extra damage) in tension will occur. The softening in tension also contributes to the development of the one and the only crack, both for tension and shear. Therefore, the softening in the tensile direction and the stress in normal direction can be calculated in a similar manner.

$$d'_{t,1} = d'_{t,0} + \frac{\sigma_0}{E_j}h_j - \frac{\sigma_0}{E_u}h_j + \frac{\sigma_{1,e}}{E_u}h_j + \frac{\sigma_{1,e}}{E_j}h_j \tag{3.45}$$

where

$d'_{t,1}$: the relative displacement of the cracked surface in tensile direction in the mechanical model after additional softening;
$d'_{t,0}$: the relative displacement of the cracked surface in tensile direction in the mechanical model before additional softening;
$\sigma_{1,e}$: the elastic tensile stress in the intact mortar layer during the rebound process of the additional softening;
σ_0: the tensile stress before the additional softening;
E_u: the elastic modulus of the unit in the mechanical model;
E_j: the elastic modulus of the mortar joint in the mechanical model;
h_j: the total height of the mortar joint in the mechanical model.

$$\Delta d'_t = d'_{t,1} - d'_{t,0} = h_j(\frac{1}{E_u} - \frac{1}{E_j})(\sigma_{1,e} - \sigma_0) = -\frac{1}{K_{t,e}}(\sigma_{1,e} - \sigma_0) \tag{3.46}$$

where

$\Delta d_t'$: the increment of the relative displacement in tensile direction of the cracked surface in the mechanical model;
$K_{t,e}$: the elastic stiffness of the zero-thickness interface element in FE model in tensile direction.

$$\sigma_{1,so} = max(\sigma_{max} + K'_{t,so}\Delta d'_t, 0) \tag{3.47}$$

where

$K'_{t,so}$: the softening stiffness of the cracked surface in mechanical model in tensile direction (negative). Its value can be calculated using equation A.6 derived in appendix A;
$\sigma_{1,so}$: the tensile stress in the cracked surface during the additional softening;
σ_{max}: the tensile stress capacity corresponding to the increase of stress or the softening in shear direction, according to the Mohr-Coulomb Criterion;

$$\sigma_{max} = min(\frac{c(1-w_0)-\tau_0}{tan\phi}, f_t(1-w_0))$$

where f_t is the original tensile strength of the interface.

Given the equilibrium between the external and internal tensile stress on the cracked surface,

$$\sigma_{1,so} = \sigma_{1,e} = \sigma_1 \tag{3.48}$$

where σ_1 is the tensile stress after the additional softening. Therefore, solving the equation 3.46, 3.47, 3.48 and A.6 gives

$$\sigma_1 = max(\sigma_0 - (1 - \frac{K_{t,so}}{K_{t,e}})(\sigma_0 - \sigma_{max}), 0) \tag{3.49}$$

and the lost of tensile strength writes

$$f_{t,lost} = \sigma_{max} - \sigma 1 \tag{3.50}$$

Therefore, the damage parameter w that is same for shear and tensile directions can be updated as:

$$w_1 = w_0 + \frac{f_{t,lost}}{f_t} \tag{3.51}$$

And same as the problem 1, the residual cohesion and tensile strength write

$$c_r = c * (1 - w_1) \tag{3.52}$$

$$f_{t,r} = f_t * (1 - w_1) \tag{3.53}$$

Similarly, the equation 3.46 and 3.47 can be illustrated as the right side of figure 3.17 below, with blue line and green line respectively.

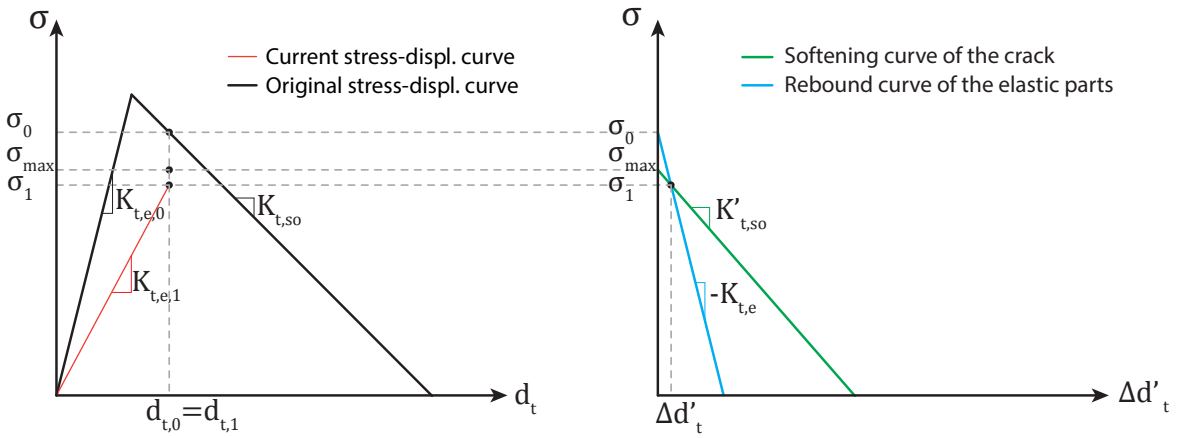

Figure 3.17: Relation between amount of softening at the interface element and the relative displacement of the real crack in tension

The left side of the figure shows the original stress state in tension before the additional softening, and the loading history of the previous step with black lines. The point with tensile stress equal to σ_1 indicates the stress state after the additional softening. The red line shows the secant unloading path if the interface element is unloaded in the future. The path for the tensile loading in the future is not plotted here as a more detailed demonstration of this part will be in section 4.2. Note that from this figure, it is easy to notice that the for the black line, the slope of the $K_{t,e,0}$ is not necessarily the same as the elastic modulus of the interface $K_{t,e}$. This is because the softening might have happened before the previous step, and secant unloading is implemented for normal direction. As it will be mentioned in section 4.2, the code of this constitutive model actually update the uni-axial constitutive array representing the uni-axial constitutive curve after elastic or plastic calculation for the future loading and unloading process. Therefore, $K_{t,e,0}$ could be a softened unloading stiffness that is less than the original $K_{t,e}$. However, please realize that for the figure on the right side, the blue line still uses the original elastic modulus $K_{t,e}$, because for the intact mortar layer above or below the cracked surface, softening has never occurred.

Also note that for problem 1, it is applicable for the calcaltion of shear stress due to the change in tensile and compressive stress, while the problem 2 is only for the calculation of the tensile stress due to the change in shear stress. The compressive stress and compressive damage is not coupled to the shear direction.

So far, we have solved the second problem. Last but not least, one should notice that the additional softening in shear and normal directions are actually interconnected. Specifically, the additional softening in shear direction will also reduce the maximum tensile stress capacity of the interface, and might further lead to additional softening in normal direction, and vice versa. Both of the softening in these two directions contribute to the development of the crack, or in other words, the damage factor w until $w = 1$. Therefore, the iterative calculation in loops that consider their influence on each other is performed until no more softening occurs, which means the final stress stage is exactly on the updated yield surface. For the details of implementation, refer to section 4.6.3.

3.5. Loading path and sub-increments

It is well known that for most of the materials, the stress changes within or along the yield surface, namely the elastic loading, unloading or reloading, are path-independent. That is, different loading histories of strains (or relative displacements in the current context) will lead to one and only final stress state, as long as all these loading histories have same final strain (relative displacement) in each direction.

In contrast, the plastic loading can be path-dependent, if we assume a fully coupled behaviour for stresses and strains in all directions. To be more specific, one cannot determine the final stress state just based on final strain (or relative displacement) state in each direction. One-to-one correspondence does not exist between them. To determine the final stress state, one needs to know the loading path of the previous plastic loading history.

For example, there is a stress state ”a” on the yield surface, as shown in figure 3.18. The elastic unloading is plotted with dashed lines. The blue dashed line first unloads in tension and then unloads in shear, and the purple unloads in the other way around. The red dashed line unloads in shear and tension simultaneously. All these three unloading processes lead to an identical stress state ”c” because they have the same final strains (or relative displacements) in shear and tension. For the plastic loading, the increments of strains (or relative displacements) cause the final stress state to be out of the yield surface if the final stresses are calculated with the elastic stiffnesses in each direction, which is also called as the elastic predictor. The elastic predictors are plotted with solid lines, in the same figure.

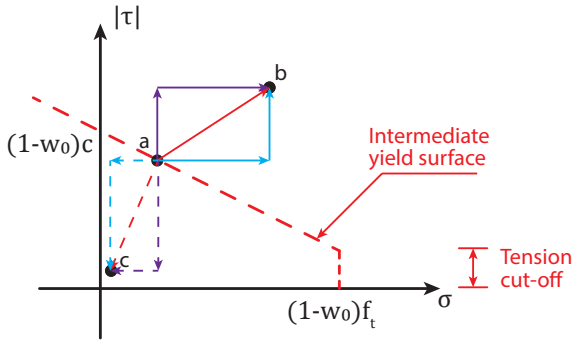

Figure 3.18: Plastic loading and elastic loading

However, although the elastic predictors for different loading processes finally point to the same point, this is not the case if we calculate final stress states in a plastic manner, which means that the final stress state must stay on the updated yield surface. And loading in tension first, loading in shear first, or loading in tension and shear simultaneously will not have the identical final stress state, which means they will be at different locations on the yield surface. Even the amount of shrinking of the yield surface can be different for these three plastic loading processes. In a nutshell, the plastic loading path will influence the final stress state.

The above-described situation is true for some of the tension and shear combinations in this proposed constitutive model because, in this model, shear and tension are partially coupled. Not all the cases are path-dependent because they are just not completely coupled as the real structure. The assumption of the so-called fully coupled damage factor w shared between tension and shear are just a tip of an iceberg of the coupling effect of shear and tension in reality. However, for the combination of compression and shear, the plastic calculation is usually path-independent, as we assume that only the compressive stress can influence the maximum shear stress capacity.

In the proposed constitutive model, we do not apply the incremental shear and tension relative displacement simultaneously because it dramatically increases the difficulty to determine the current stress state. Instead, we try to apply the increment of relative displacement in normal direction first and then apply the increment of relative displacement in shear direction subsequently, using the formulas derived in this chapter. As is discussed above, this should be fine for all loading, unloading and reloading within the elastic regime, and applicable for most of the combined shear and compression plastic loading case. However, for the combination of shear and tension, this is clearly not correct.

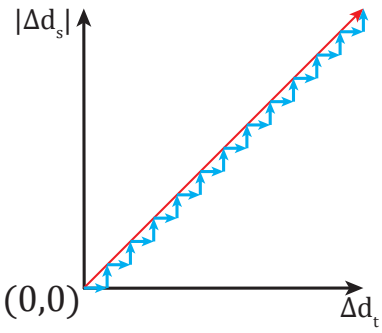

Figure 3.19: Sequence of applying sub-increments of the increments of relative displacements in shear and tensile direction

Therefore, to compensate this disadvantage, for the given increments of relative displacements in shear and tension, this constitutive model assumes that the determined current stress state should converge to the stress state as if they are applied simultaneously. To achieve this, the increments of relative displacements in shear and tensile directions are divided into more sub-increments. They are applied in the way shown in figure 3.19 with blue arrows.

As the amount of sub-increments increases, the determined current stress states will converge to the stress state calculated with the red arrow in figure 3.19. The maximum quantity of the sub-increments can be determined by the user to balance the numerical accuracy and the computational cost. The model itself can check if that much sub-increments are needed simply by performing the plastic calculation with 2 and 3 sub-increments and compare their results. If they are the same, then no more sub-increments are needed for this step at this integration point. Otherwise, the user-defined number of sub-increments will be adopted in the plastic calculation to get a reliable result.

In reality, the increments of relative displacements in different directions might not be really applied simultaneously. However, in FEM analysis, as we divide the external load into small enough load steps or time steps, for each step, we can still assume that the increments of relative displacements are applied simultaneously.

Also, one might ask that if it is necessary to have sub-increments for each increment if we could just use smaller step size and accordingly smaller increments of relative displacements in both directions. The answer is that using smaller steps size will be much more computationally expensive than using larger steps size with sub-increments, because after each step, the stiffness matrix might be updated and more numerical calculations are involved. Furthermore, if the sub-increments are not adopted but path dependency does exist, then the result will be more step-size dependent than using sub-increments. It will take more time for computation and more effort for someone to perform sensitivity analysis to determine a reasonable step size.

3.6. Summary

In a nutshell, this constitutive model tries to calculate the stresses in normal and shear directions sequentially but also consider a certain degree of coupling effect between them. In a plastic calculation, the given pair of increments of relative displacements in shear and normal direction is divided into n pairs of sub-increments to consider the possible path dependency. Each time one pair of sub-increments in shear and normal direction will be applied.

In the first pair of sub-increments, the sub-increment of relative normal displacement will be applied uni-axially first with one of the two Coupling Options. Then the extra damage will be calculated in shear direction first, to consider the reduction of maximum shear capacity due to change of normal stress and

possibly increase of damage factor. Next, the extra damage in normal direction will also be calculated due to the extra damage just calculated for shear. The extra damage calculation will be performed iteratively until no more damage occurs in normal and shear direction. Till here, the application of sub-increment of relative normal displacement is finished, and the normal and shear stresses, as well as the damage factor, are updated. The updated stress state is on the updated yield surface.

Secondly, the first sub-increment of relative shear displacement will be applied uni-axially with the same Coupling Option as the normal direction. Subsequently, the extra damage in normal direction will be calculated to consider the possible reduction in maximum tensile strength as a result of the change of shear and the possible increase of damage factor. And then the extra damage in shear direction will be calculated as the result of the extra damage just calculated for tension. This two extra damage calculations will be repeated until no more damage occurs. Till here, the application of sub-increment of relative shear displacement is finished, and the shear and normal stresses, as well as the damage factor, are once again updated.

After finishing applying the first pair of sub-increments, the rest of the pairs of sub-increments are applied in the exact same way. The final normal stress σ_1, shear stress τ_1 and the damage factor w and w_c will be returned to the FE program as the outcome of this proposed constitutive model. Also, the 2×2 stiffness matrix will be returned to the program with diagonal terms based on the tangential slope on the normal (tensile or compressive) uni-axial constitutive curve and the shear uni-axial constitutive curve corresponding to the latest relative displacements. The off-diagonal terms are set to be zero for simplicity, which is why we emphasize that the normal and shear directions are not explicitly coupled but only partially coupled.

Last but not least, the main reason why the idea of total strain method of the Engineering Masonry Model, which inspired this constitutive model a lot, is not adopted in this thesis as total-relative displacement method is because of the adoption of sub-increments. If sub-increments are only needed for plastic calculation, then using some of them for elastic calculation process will be a waste of computational power. Therefore, if the original stress state is within the yield surface, and the increment of the relative displacement will undergo a plastic process according to the elastic predictor, then this constitutive model is designed to firstly calculate to the elastic limit stress state on yield surface before the start of the plastic process, with the Elastic Limit Finder that will be introduced in section 4.5. Then, it fully utilizes all the sub-increments for the plastic calculation for a more accurate result.

4

Implementation of the constitutive model

In this chapter, all the theories and assumptions introduced in chapter 3 will be implemented as a user defined sub-routine for Diana. The subroutine is written with modules. To visualize the code, the subroutine is also illustrated with flow charts in this chapter. The following section will first introduce the overall structure of the subroutine and then introduce each module involved in that structure.

4.1. Overview

The overall structure of the user defined subroutine is shown in figure 4.1. The chart flows in this chapter are illustrated according to the rules in ISO 5807. The flowcharts flow from the top to bottom and left to right. Additionally, the shapes filled in red represent the main components of the chart. The yellow shapes are the inputs, and the blue shapes are the outputs. The green shapes are the less important value assignments to some variables.

The inputs of the user subroutine include the stresses and relative displacements in shear and normal directions of the last step, the increments of the relative displacements of the current step, and all the material properties introduced in section 3.1. The superscript 0 and 1 stand for the input and output values of the subroutine, respectively. The subscript 0 and 1 also stand for input and output values, but for the intermediate variables of the modules of the subroutine only.

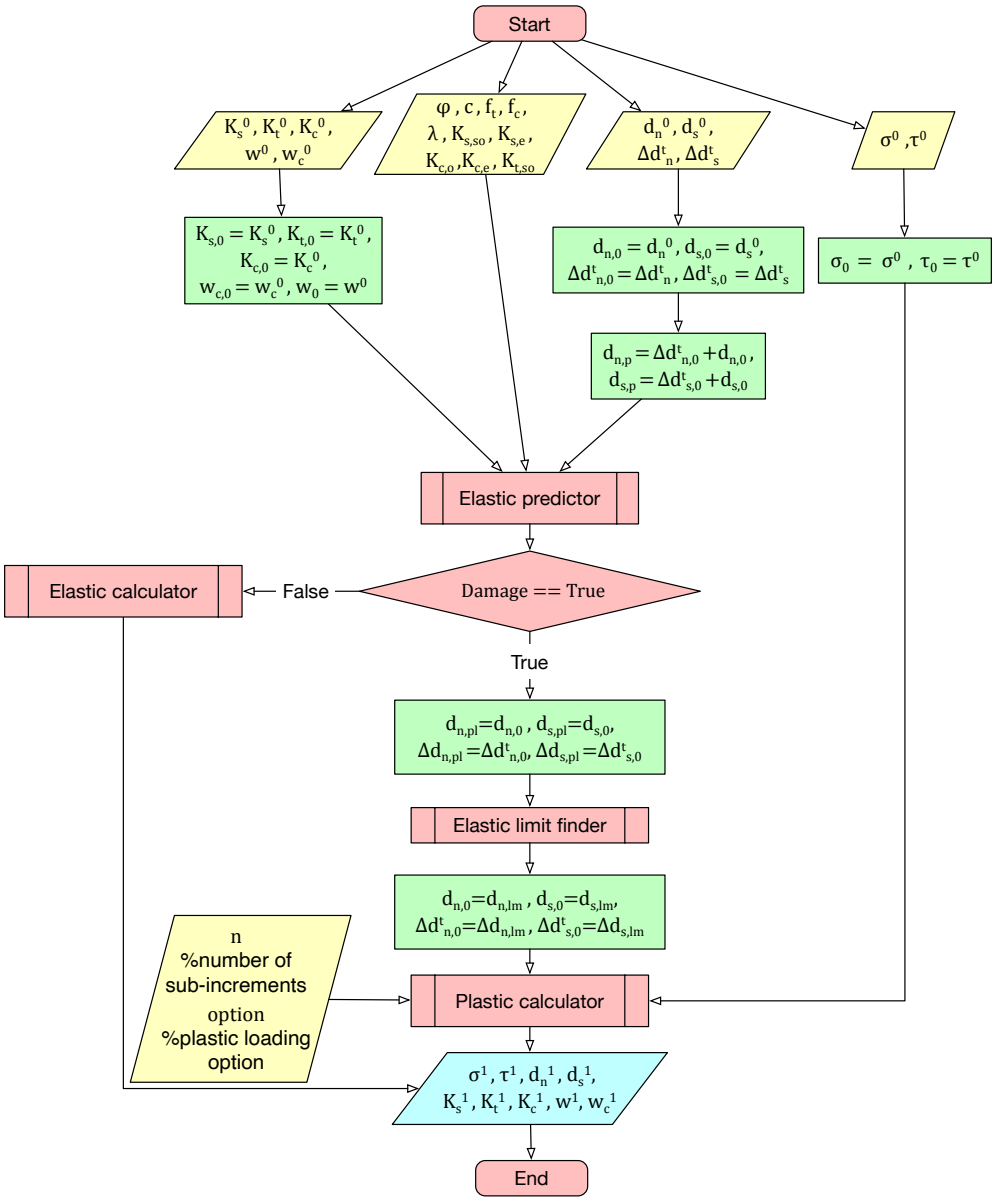

Figure 4.1: Overview of the structure of the constitutive model

The uni-axial constitutive arrays in tension, compression, and shear are special arrays defined in this constitutive model. The tension and shear arrays K_t and K_s include all the value of stresses and relative displacements of the turning points that compose the corresponding multi-linear uni-axial constitutive curve. For the compression array K_c, it contains the critical points that make the uni-axial parabolic compressive curve or the modified uni-axial Engineering Masonry Model compressive curve. For the initial state, they can be as listed in table 4.1 below. Note that the shear array only has its positive part. In this constitutive model, all negative shear stress will be converted to positive with its corresponding relative shear displacement for further calculation.

However, after each elastic or plastic process, these three uni-axial constitutive arrays are re-constructed, as will be discussed in section 4.2. Both the compression and shear arrays will keep its original size, but the size of the tension array might change, as listed in table 4.2. This is the result of the full coupling between the shear and tension, as well as the secant unloading principle. The coupling of shear and tension has been discussed in section 3.3.3 and 3.4. The shear stiffness still remains its original size because the unloading follows initial elastic stiffness $K_{s,e}$. Note that the updated compressive array K_c

is already at the post-peak stage.The details of these changes will be discussed in section 4.2. The initial tension, shear, and compression arrays are automatically composed by the constitutive model with the input parameters translated from the material tests. For how to translate (calculate) the material properties obtained from the tests to the input parameters for the constitutive model, please refer to section 3.2, 3.3, and chapter 6.

Table 4.1: Initial tension, shear and compression arrays

K_t

0	0
d_{ft}	f_t
$d_{t,u}$	0

K_s

0	0
$d_{s,peak}$	τ_{peak}
$d_{\tau f}$	τ_f

K_c

0	0
0	0
$d_{c,limit} = d_{fc/3}$	$\sigma_{c,limit} = -f_c/3$
$d_{fc/3}$	$-f_c/3$
d_{fc}	$-f_c$
$d_{c,u}$	0

Table 4.2: Updated tension, shear and compression arrays

K_t

0	0
...	...
...	...
$d_{t,peak}$	$f_t(1-w)$
$d_{t,u}$	0

K_s

d_o	0
$d_{s,peak}$	τ_{peak}
$d_{\tau f}$	τ_f

K_c

0	0
$d_{c,\lambda}$	σ_λ
$d_{c,limit}$	$\sigma_{c,limit} = -f_c(1-w_c)$
$d_{c,limit}$	$\sigma_{c,limit} = -f_c(1-w_c)$
$d_{c,limit}$	$\sigma_{c,limit} = -f_c(1-w_c)$
$d_{c,u}$	0

4.2. Constitutive Array Re-constructor

The module Constitutive Array Re-constructor, as shown in figure 4.2, is used to update the uni-axial constitutive arrays, K_t, K_c and K_s after each loading, unloading or reloading process. It contains two sub-modules of Normal Constitutive Array Re-constructor and Shear Constitutive Array Re-constructor. The former one takes charge of the tension and compression arrays K_t, K_c, and the latter one takes charge of the shear array K_s.

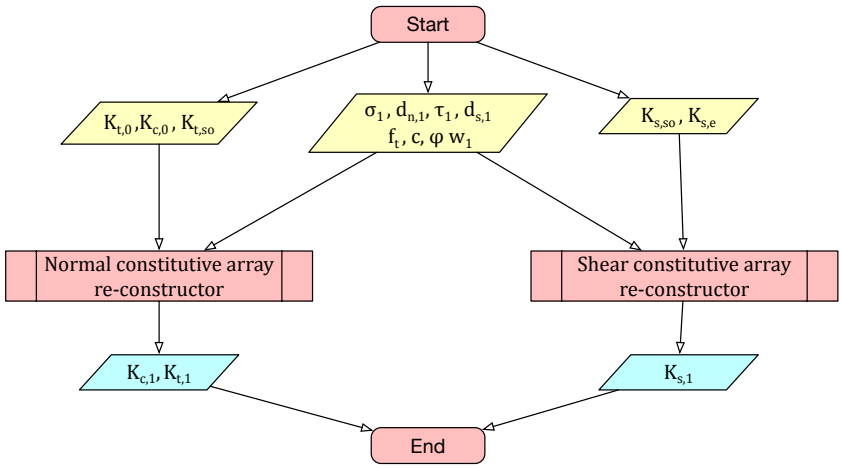

Figure 4.2: Constitutive array re-constructor

Before discussing the details of the sub-module, let us look into the special properties of the tension array K_t. Unlike the compression array K_c and the shear array K_s which always remain their size, the tension array K_t might change its size after loading, unloading and reloading processes, as shown in table 4.1 and 4.2 in section 4.1. Two necessary conditions for the property of changing array size are listed below:

- The integration point unloads in that direction with a stiffness other than the initial stiffness (in this case the secant stiffness);

- The maximum stress capacity of that direction of an integration point depends on the stress in the other direction.

Only the tension array satisfies these two conditions, so the K_t cannot always maintain its size. In other words, the segments before the peak of the stress-relative displacement curve of tension might be multi-linear with more than one slope. Four possible examples of change shape of the stress-relative displacement curve are shown in figure 4.3 below. The gray lines stand for the original shape of that curve before the update of tensile stress. The red dot with a dark circle around it represents the current tensile stress, and the red lines are the current stress-relative displacement curve after running this module of Constitutive Array Re-Constructor. The current relative displacement d_n and the stress σ of each red dot at the turning point of the red lines are stored in the tension array K_t.

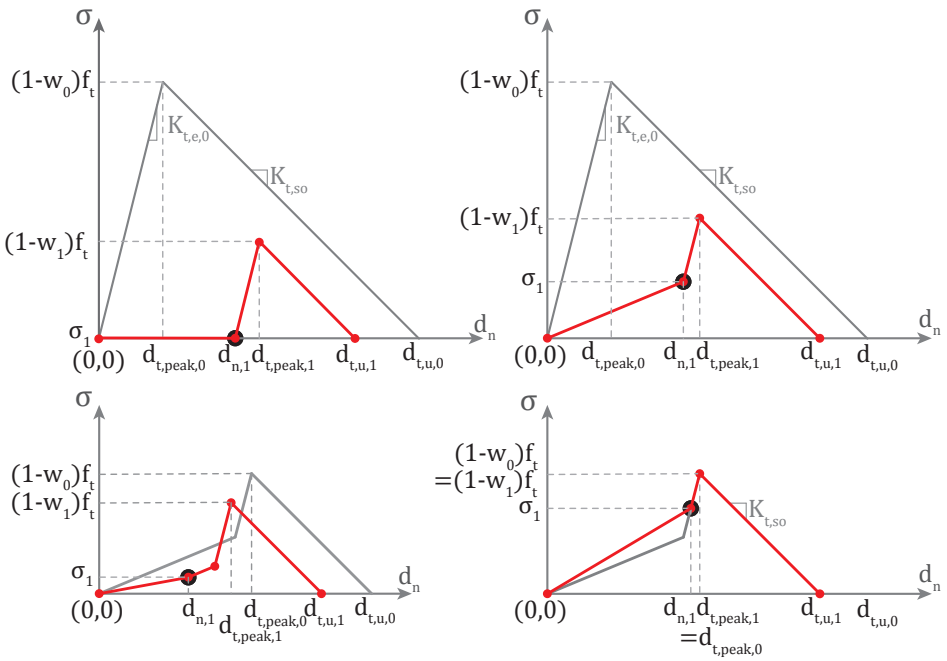

Figure 4.3: Examples of change of tension array K_t

The procedure for the tension array re-construction is simply vertical and horizontal translation, as shown with green arrows in figure 4.4 below. The vertical translation shifts the original curve downward to meet the new stress peak $\sigma_{peak,1} = (1 - w_1)f_t$, and the following horizontal translation shifts the curve until it goes through the current stress point $(d_{n,1}, \sigma_1)$. Finally, a secant line links the current stress point to the origin, and the new tensile stress-relative displacement curve is re-constructed.

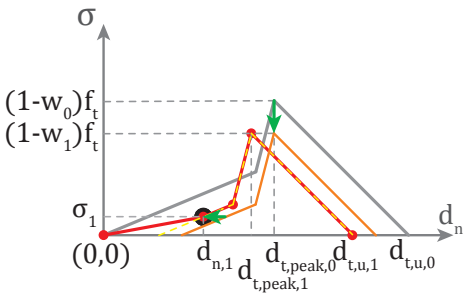

Figure 4.4: Example of the process of updating tension array K_t

The changes of the shear and compressive stress-relative displacement curve are illustrated in figure 4.5 below, with the size of the uni-axial constitutive arrays K_s and K_c unchanged all the time. Note that for the compression, the parabolic curve is used. And for simplicity, the unloading and reloading factor λ introduced in section 3.3.2.1 is assumed to be 0 here such that unloading and reloading follow secant stiffness. Examples of the uni-axial constitutive arrays K_s and K_c can be referred to table 4.1 and 4.2.

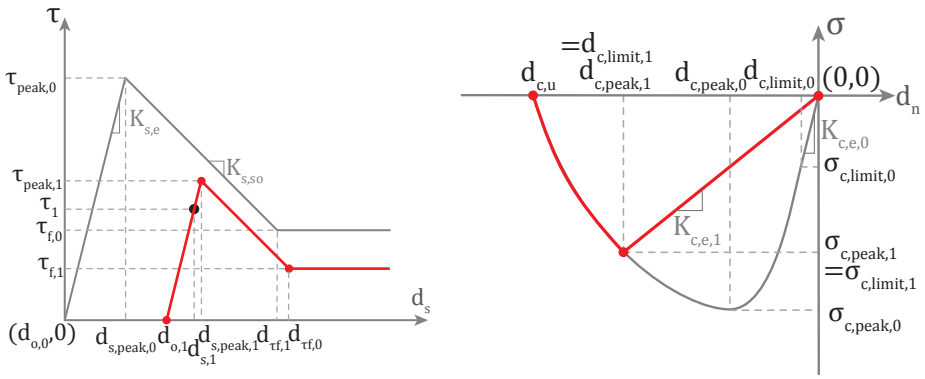

Figure 4.5: Examples of change of shear array K_s and compression array K_c

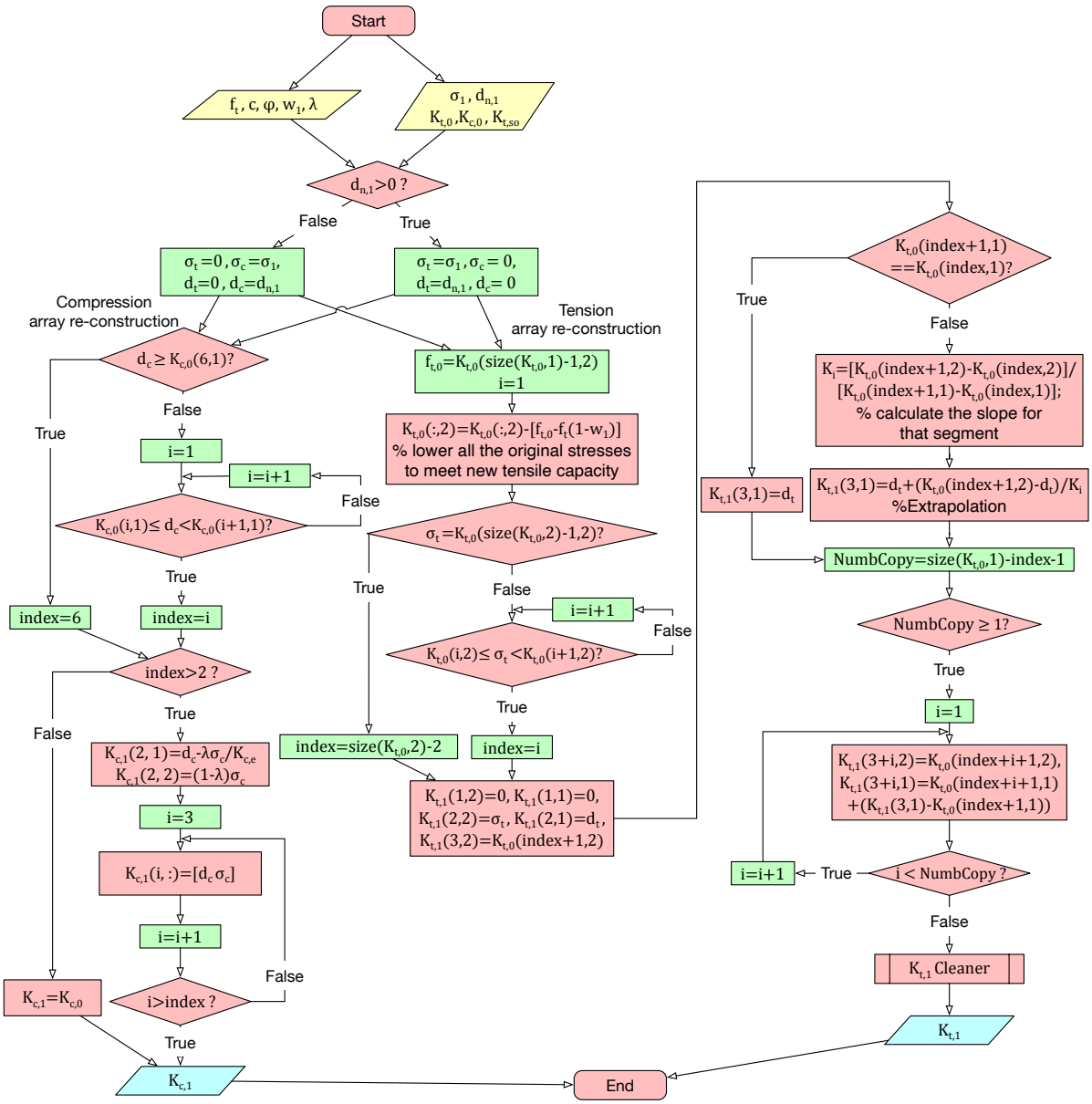

Figure 4.6: Normal constitutive array K_t K_c re-constructor

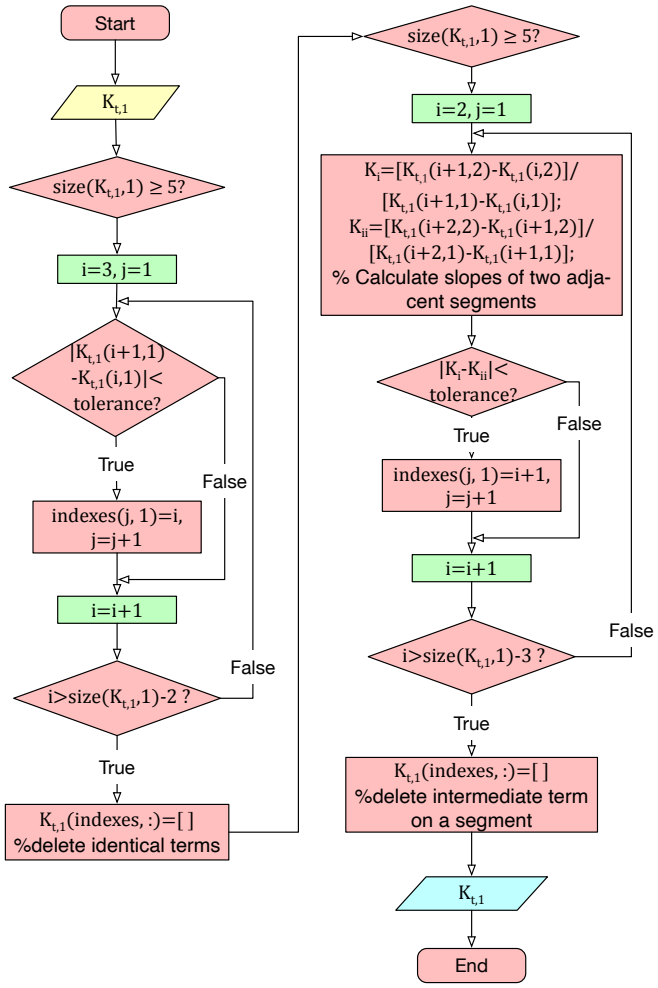

Figure 4.7: Tension constitutive array $K_{t,1}$ cleaner

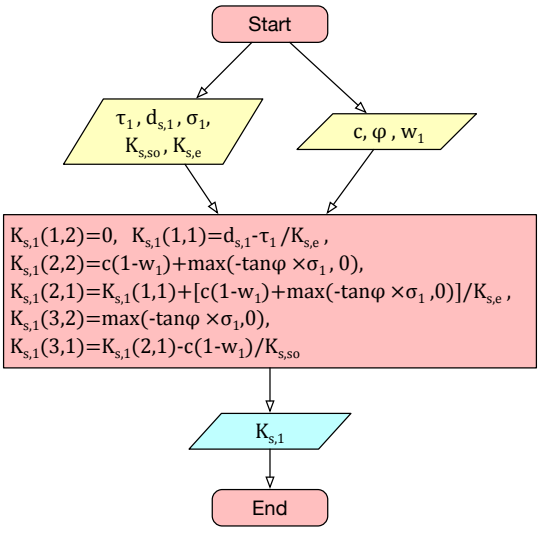

Figure 4.8: Shear constitutive array K_s re-constructor

The updating procedures for the normal direction mentioned above are written into the module of Normal Constitutive Array Re-constructor with the structure shown in figure 4.6 above. The most left column

of the figure is for compression, and the right two columns are for tension. Because of the complication of the tension array K_t, a sub-module of $K_{t,1}$ cleaner is introduced to reduce the size of the tension array with very closely located stress points or with three stress points almost on the same line, as shown in figure 4.7. It can also reduce the memory usage of the analyses. Note that for the cleaning process, the second row of the K_t must not be deleted as it contains the current relative displacement of tension and current tensile stress. Deleting this row will lead to numerical errors that the updated stress state is slightly out of the updated yield surface. Last but not least, the straightforward updating procedures for shear is shown in figure 4.8.

4.3. Elastic Predictor

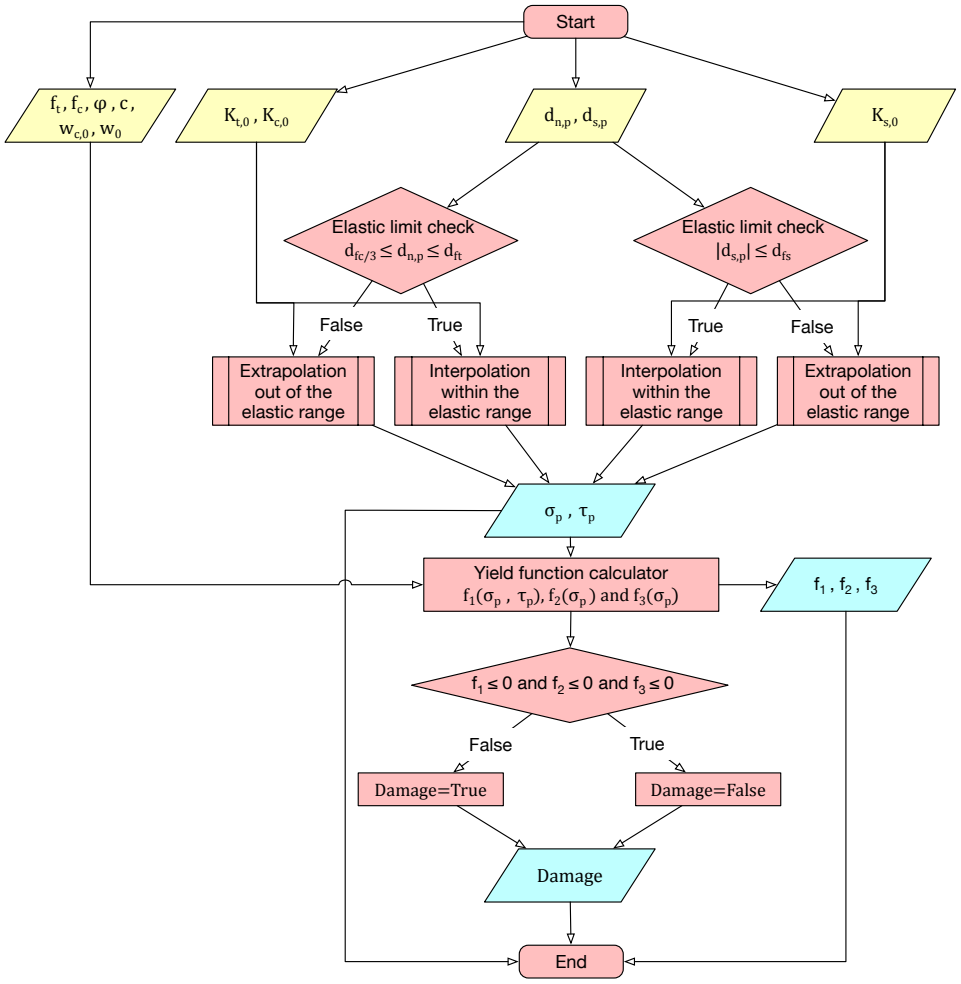

Figure 4.9: Module of Elastic Predictor

The module of Elastic Predictor, as shown in figure 4.9, is to predict the possible stresses in both shear and normal directions assuming that the structure will always be loaded with elastic stiffnesses. To calculate the corresponding elastic stresses of the predicted total relative displacements $d_{n,p}$ and $d_{s,p}$, linear interpolation or extrapolation is used. For both of them, the data in the first row to the second last row of the tension, compression and shear arrays will be used. Especially, for the tension array K_t, the third last row to the second last row will be used for slope calculation in extrapolation. After obtaining the predicted stresses σ_p and τ_p, they will be used as inputs for the yield function f_1, f_2 and f_3, as mentioned in equation 3.30. Based on the values of these yield functions, the boolean variable $Damage$ will be outputted depending on whether these predicted relative displacements will enter plasticity or not.

Note that in this constitutive model, we consider all the relative displacements and its corresponding stresses within the elastic regime if the increments of the relative displacements do not further induce plasticity, or in other words, if softening or hardening does not occur. Therefore, for compression, only the linear line of the beginning of parabolic curve is considered as elastic part, while no elastic part exists for the modified Engineering Masonry Model compressive curve. After some hardening, the elastic part of the compressive curve will enlarge. For tension, the multi-linear segments of the tension array before the peak are all considered as within the elastic regime, as is shown in figure 4.3. These multi-linear segments can be identified as two parts. The first part is a linear line connecting the origin $(0, 0)$ to the current stress state $(d_{n,1}, \sigma_1)$, which reflects the possible stress-relative displacement

relation if secant unloading happens. And the second part, that is the possibly multi-linear segments connecting the current stress state $(d_{n,1}, \sigma_1)$ to the peak $(d_{t,peak,1}, (1-w_1)f_t)$, tells the stress-relative displacement relation if elastic loading occur. This is also the beauty of these tension, compression and shear constitutive arrays, which includes all the stress-relative displacement relations no matter it is loading, unloading or reloading.

4.4. Elastic Calculator

If the total relative displacements $d_{n,p} = \Delta d^t_{n,0} + d_{n,0}$ and $d_{s,p} = \Delta d^t_{s,0} + d_{s,0}$ in both directions are inputted as predicted relative displacements into the Elastic Predictor and it returns $Damage == False$, the increments of relative displacements in shear and normal directions will not increase the amount of plasticity of the structure. Therefore, the predicted stresses σ_p and τ_p are just the real stresses of the structure. This is illustrated in figure 4.10 below.

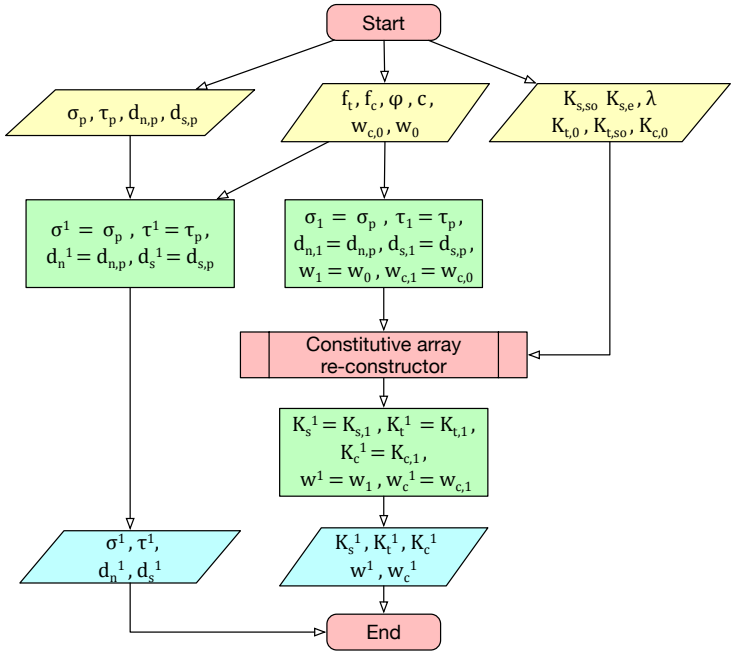

Figure 4.10: Module of Elastic Calculator

Moreover, the shear, tension and compression arrays will be updated to provide a right stress-relative displacement relation if unloading occurs in the future step, with the module of Constitutive Array Re-constructor in section 4.2. One might doubt the necessity of updating these arrays K_t, K_c and K_s even after an elastic loading. And it is indeed not necessary to update them except K_t. This is because, in this constitutive model, the elastic region of the stress-relative displacement curve in tension is assumed to be convex multi-linear function. This is also discussed in detail in section 4.2. For example, we can look at the middle of figure 4.3. If the current stress state in tension is plotted at $(d_{n,1}, \sigma_1)$ and in the future it is loaded elastically. To correctly capture the secant unloading relation afterwards, the tension array K_t should be updated.

The damage factor w and w_c do not change in this module of Elastic Calculator.

4.5. Elastic Limit Finder

If the total relative displacements in both directions are inputted as predicted relative displacements into the Elastic Predictor and it returns $Damage == True$, plasticity further develops. In this situation, assuming that the increments of relative displacements in both directions are applied simultaneously as mentioned in section 3.5, a module called Elastic Limit Finder is introduced to find the relative displacements corresponding to limit stress state on the yield surface right before the plasticity process starts, according to the multi-surface failure criterion mentioned in section 3.3.3. And a pair of new increments in both directions is also calculated for plastic calculation. The structure of this module is illustrated in figure 4.11, with a core solver, called Bisection Iteration Solver, as shown in figure 4.12.

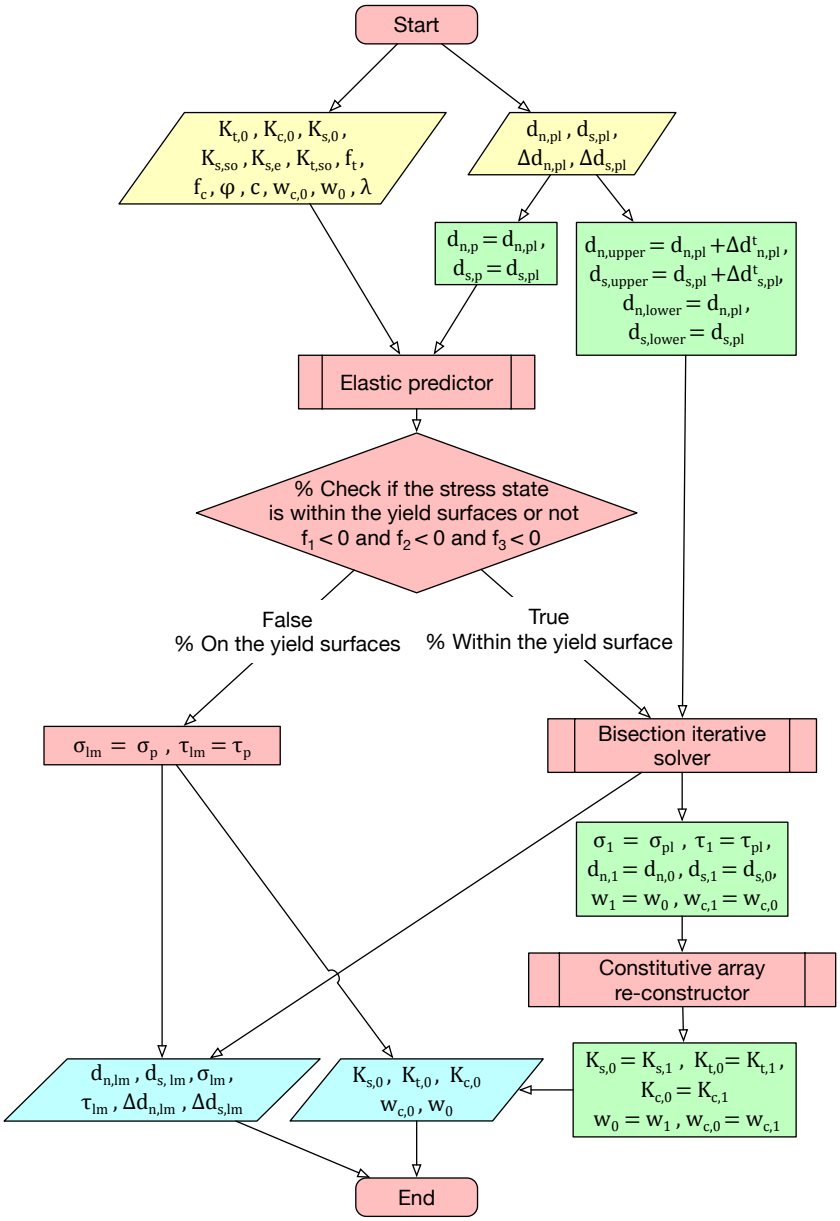

Figure 4.11: Elastic Limit Finder

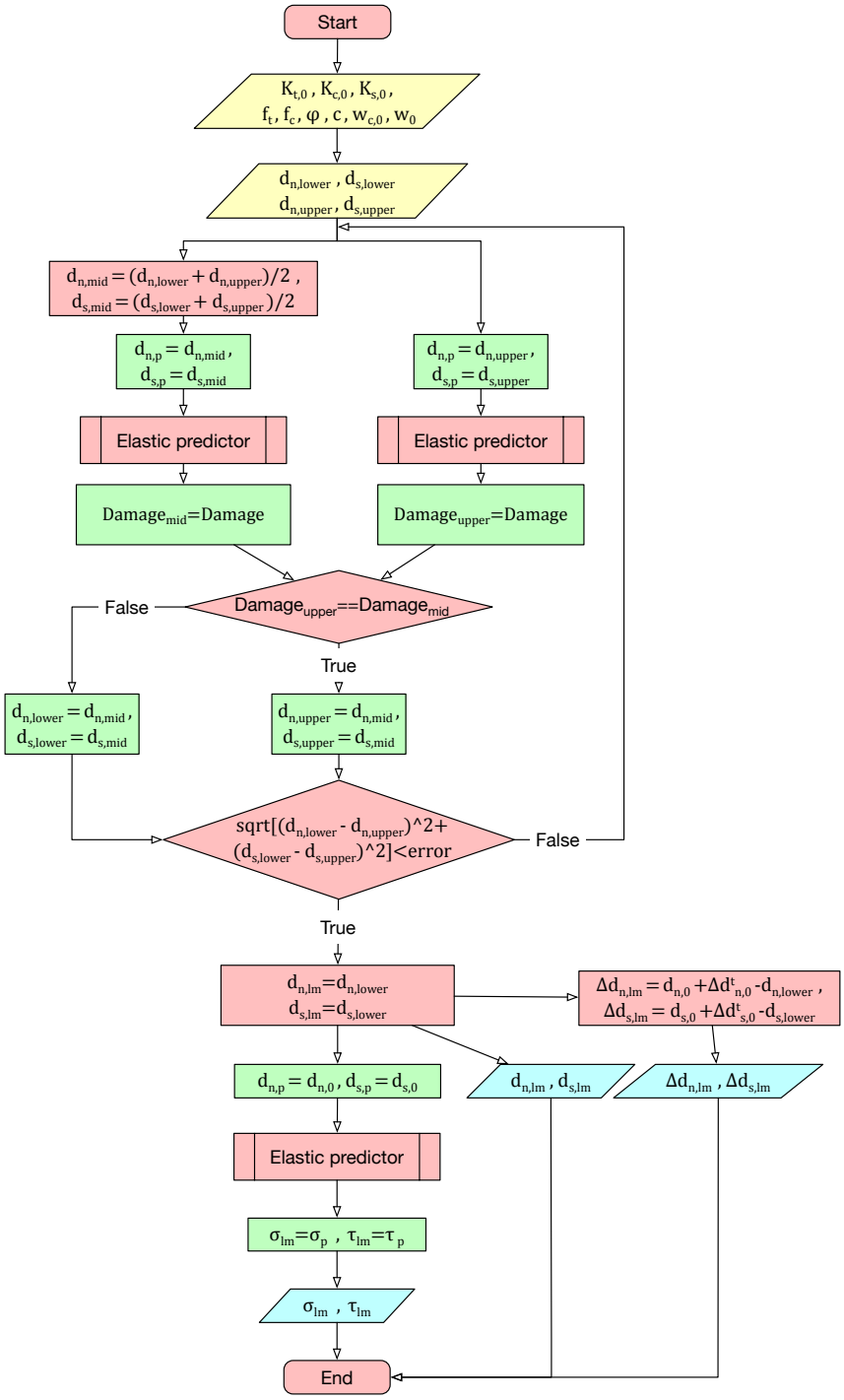

Figure 4.12: Bisection Method Solver

No matter if the initial stress state (σ^0, τ^0) is on the yield surface or within the yield surfaces, the Bisection Iteration Solver will be used to find that limit stress state. This is necessary even for the latter case because two special situations could occur when applying the increments of relative displacements in both directions simultaneously. The first one is that the stress state might go along one yield surface and go through another yield surface such that it enters the plasticity, as illustrated in figure 4.13 with blue line. The other one is that it can even go back within the yield surfaces and go out finally, as illustrated in figure 4.13 with green line. The green and blue dots represent the updated limit stress states after running this module. The latter situation (in green) is due to the multi-linear elastic part of

the tension uni-axial constitutive curve. Furthermore, because the elastic part is a convex function, as shown in figure 4.3, the slope of the green line can only become more gentle with the normal stress increases. This module is necessary because if these two situations are calculated with the Plastic Calculator mentioned in section (4.14) before reaching the limit stress state, the output will include some unrealistic plastic damage. Of course, using more and smaller sub-increments can reduce the unrealistic plastic damage, it can be more computationally demanding than directly finding a correct elastic limit.

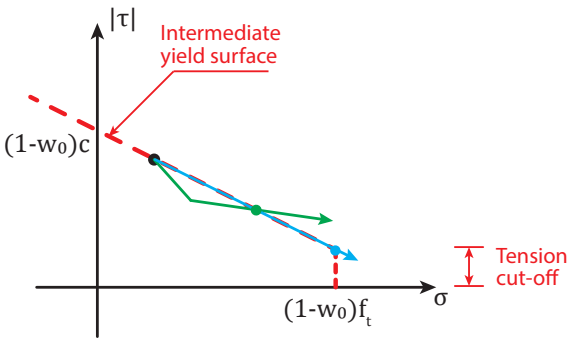

Figure 4.13: Two special cases of plastic loading

The Bisection Iteration Solver is based on the Bisection Method. The method consists of repeatedly bisecting the interval defined by these values and then selecting the subinterval in which the function changes sign, and therefore must contain a root. The initial interval is bounded by the original and current total relative displacements before and after applying the relative-displacement increments. The sign is the value of the Boolean Variable $Damage$ returned from the Elastic Predictor, assuming that it is positive for $True$ and negative for $False$. The root is the relative displacement $d_{n,lm}$ and $d_{s,lm}$ corresponding to the limit stress state σ_{lm} and τ_{lm} on the yield surface which would be out of the yield surfaces if tiny relative-displacement increments are applied proportionally in both directions. In addition to the limit stresses and the relative displacements, the new increments of relative displacements ($\Delta d_{n,lm}$ and $\Delta d_{s,lm}$) are also calculated for the following plastic calculation. The Bisection Iteration Solver is necessary because the elastic part of the stress-relative displacement relation in tension is not linear but multi-linear, which makes the direct solver less suitable.

Note that this module of Elastic Limit Finder will also be used multiple times in the module of Plastic Calculator.

4.6. Plastic Calculator

After running the module of Elastic Limit Finder, the new initial relative displacements, new initial stresses and the new increments of relative displacements are ready for plastic calculation in the module of Plastic Calculator. The Plastic Calculator is written with the structure illustrated in figure 4.14. The basic idea is to divide the total increments of relative displacements $\Delta d^t_{n,lm}$ and $\Delta d^t_{s,lm}$ into many pairs of small sub-increments Δd_n and Δd_s with the same proportion of sub-increment to the total increment for each direction. This is discussed in detail in section 3.5. For each pair of sub-increments, the integration point is loaded in compression first and then in tension.

Three core sub-modules in the Plastic Calculator containing the Tension Plastic Loader, Compression Plastic Loader and Shear Plastic Loader, which are uni-axial loaders based on the theories mentioned in section 3.3, will be discussed in section 4.6.1 and 4.6.2. The other core sub-module called Damage Calculator, ensuring the identical damage of shear and tension, is based on the theories introduced in section 3.4. It will be discussed in section 4.19.

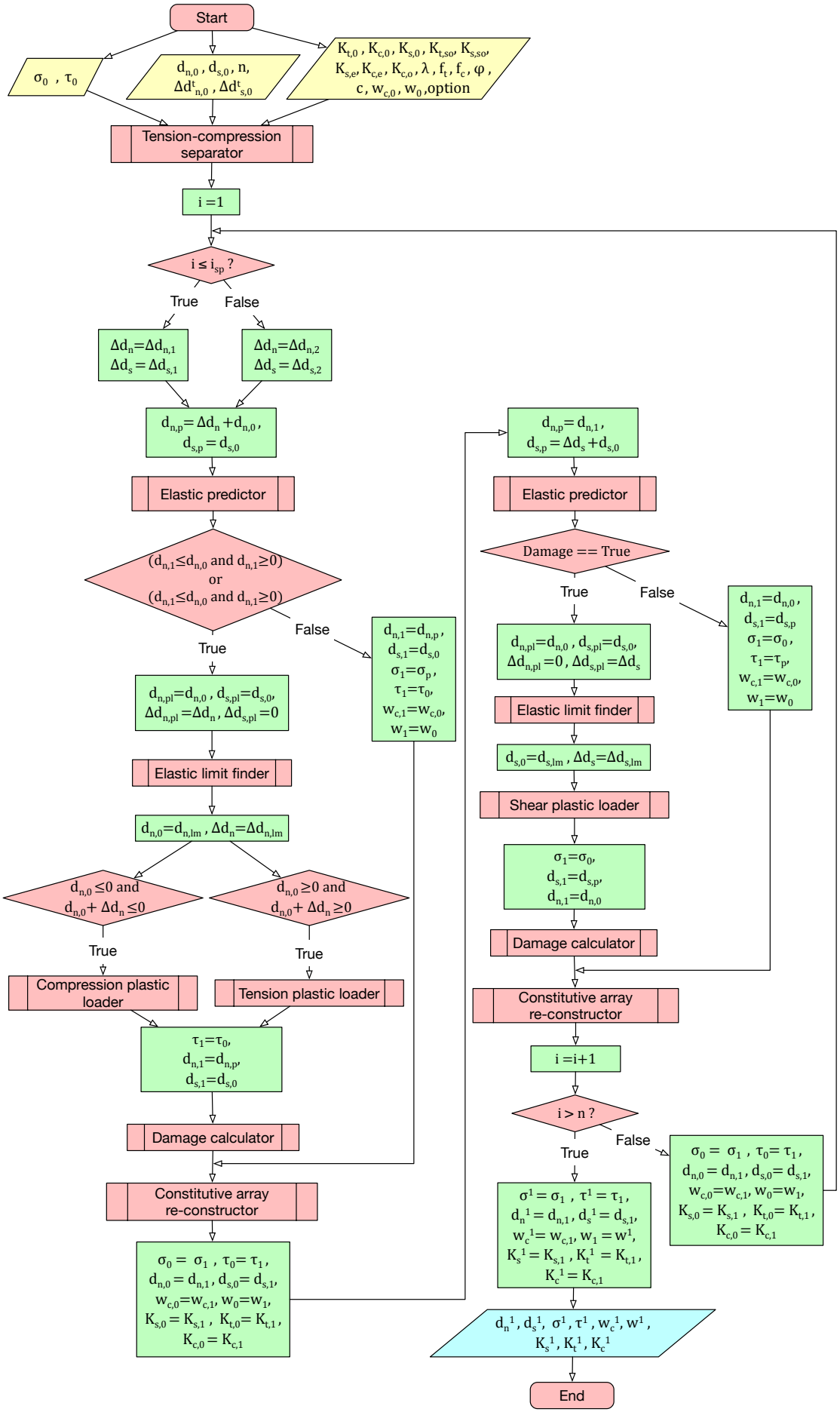

Figure 4.14: Plastic Process Calculator

Additionally, because the calculation of the stress in the normal direction is divided into two sub-modules of tension and compression to take into account their their different coupling relation with the shear direction, as discussed in section 3.3.3, a sub-module of Tension-Compression Separator is introduced to ensure that no sub-increment goes from tensile relative displacement across zero to compression or the other way around. This module is illustrated in figure 4.15.

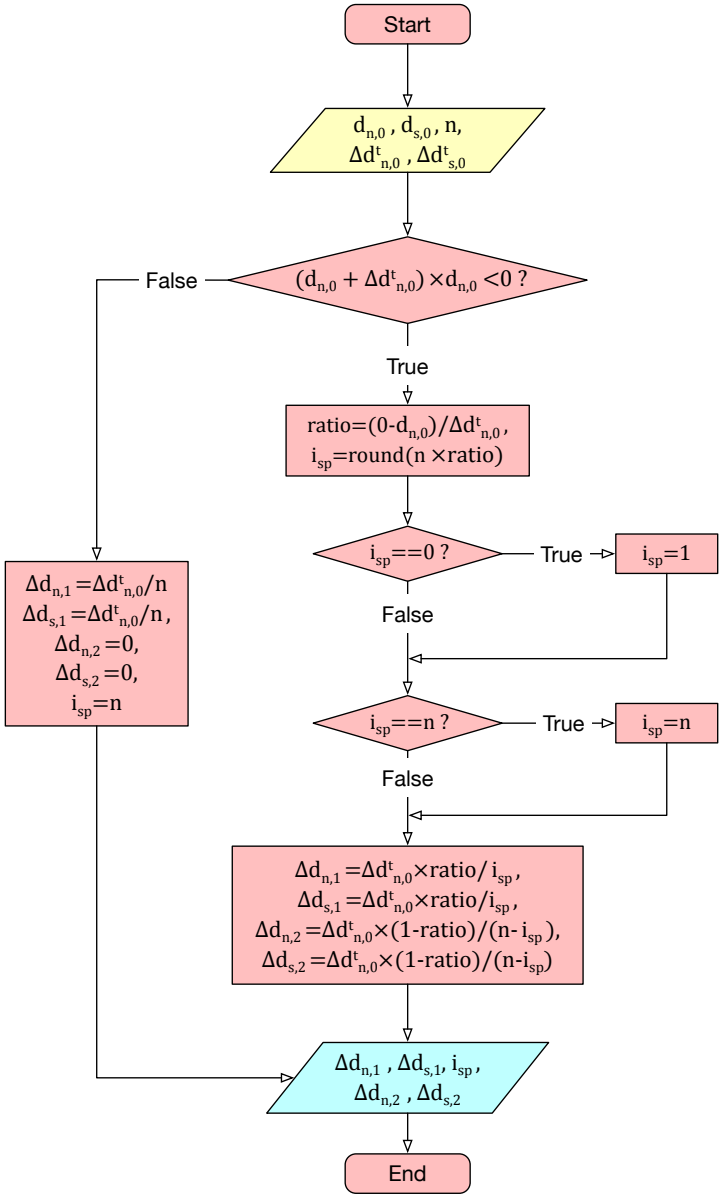

Figure 4.15: Tension Compression Separator

Also note that, even in the Plastic Calculator, two elastic modulus, namely the Elastic Predictor and Elastic Limit Finder, are still needed. This is because the structure might be loaded elastically in one direction while it is loaded plastically in the other direction. To be more specific, although we assume that the increments of relative displacements in both directions are applied simultaneously, indeed, we apply the small portion of increment in the normal direction first and then apply the same portion of shear increments of relative displacements, as is discussed in section 3.5. Therefore, there are situations where the overall plastic process includes some elastic processes. In these situations, the Elastic Predictor and the Elastic Limit Finder are still needed. For example, the structure is unloaded in tension elastically, and then loaded in shear first elastically and then plastically.

4.6.1. Uni-axial Plastic Loader in normal direction

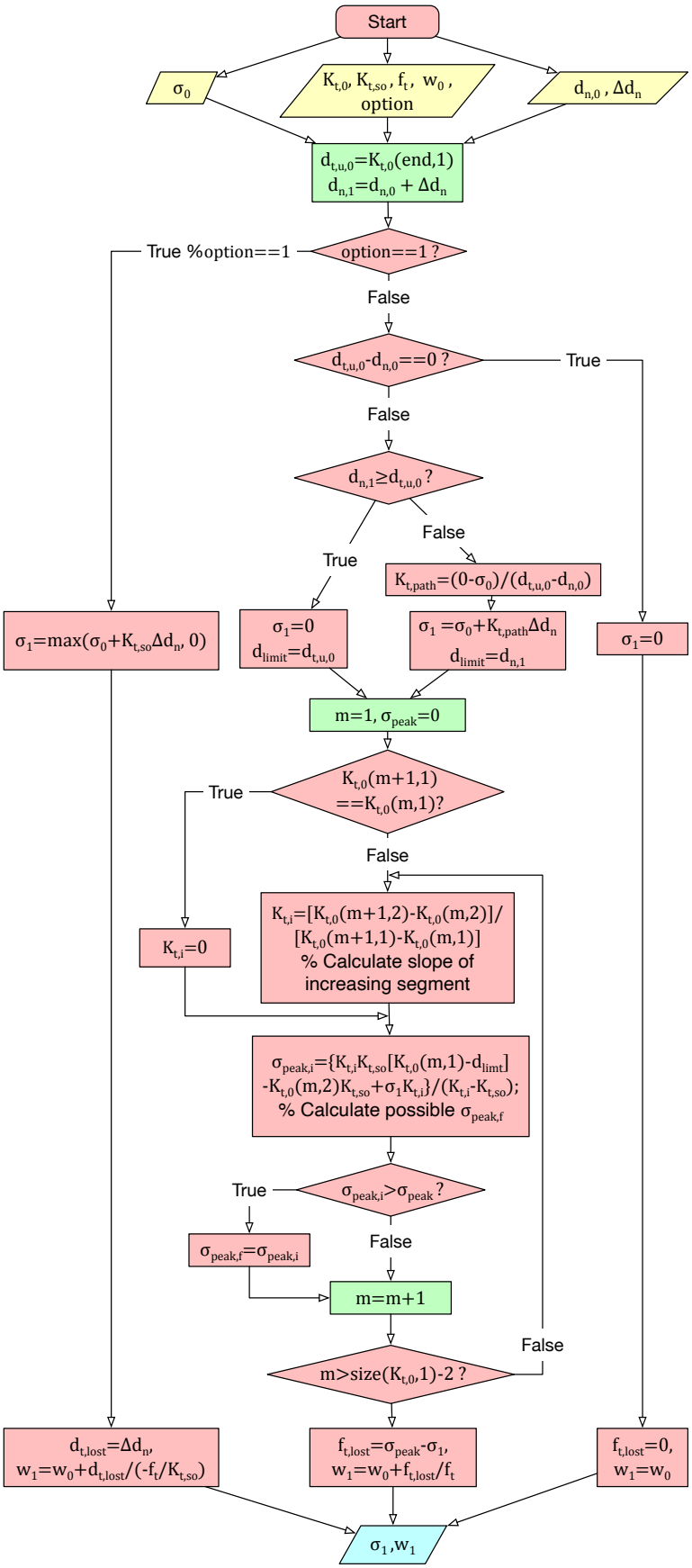

Figure 4.16: Tension Plastic Loader

The plastic loader in normal direction is divided into two modules, namely the Tension Plastic Loader and the Compression Plastic Loader, as shown in figure 4.16 and 4.17. Both the Tension Plastic Loader and the Compression Plastic Loader only contains the loading part after the elastic limit. The unloading parts for both tension and compression are handled by the Elastic Predictor. Especially, the unloading in compression is calculated by the Elastic Predictor because it is an elastic process for compression, even though it will reduce the maximum shear capacity and enter plasticity in shear direction.

The Tension Plastic Loader calculated the stress and the amount of softening in tension with two possible ways, the Option 1 or Option 2, with the maximum tensile capacity determined by the shear stress. This is discussed in section 3.3.3 as Coulomb friction. The Compression Plastic Loader calculates the stress and the amount of damage w_c due to softening by directly reading the value on the parabolic constitutive curve or modified Engineering Masonry Model compressive curve (figure 3.5 or 3.6), because the maximum compressive capacity is assumed to be independent on the shear stress.

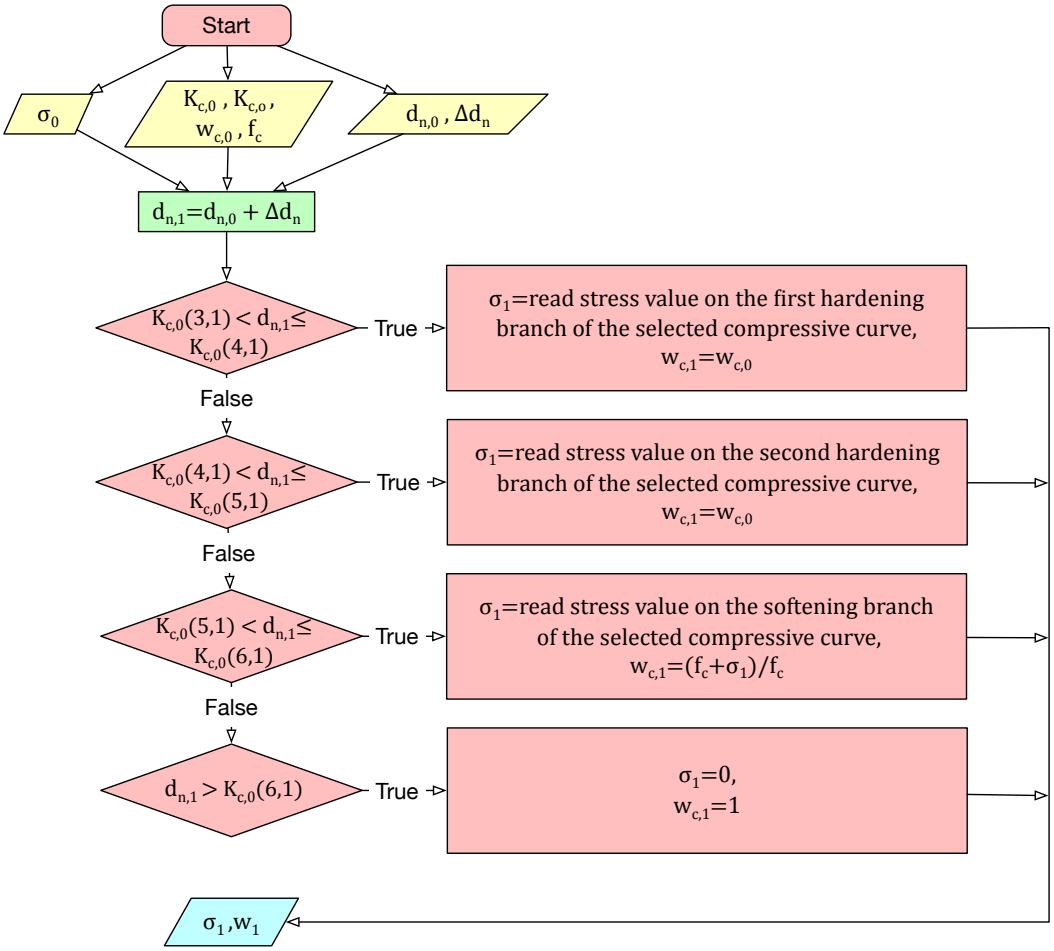

Figure 4.17: Compression Plastic Loader

4.6.2. Uni-axial Plastic Loader in shear direction

The code structure of the module of Shear Plastic Loader is shown in figure 4.18. It is similar to the Tension Plastic Loader that has two ways to calculate the amount of softening and stress. For the option 2, its structure is simpler than the option 2 of the Tension Plastic Loader because in shear direction unloading with the initial stiffness $K_{s,so}$ is used and the elastic part of the constitutive curve is linear while in tension secant unloading is used and the elastic part of the constitutive curve is multi-linear.

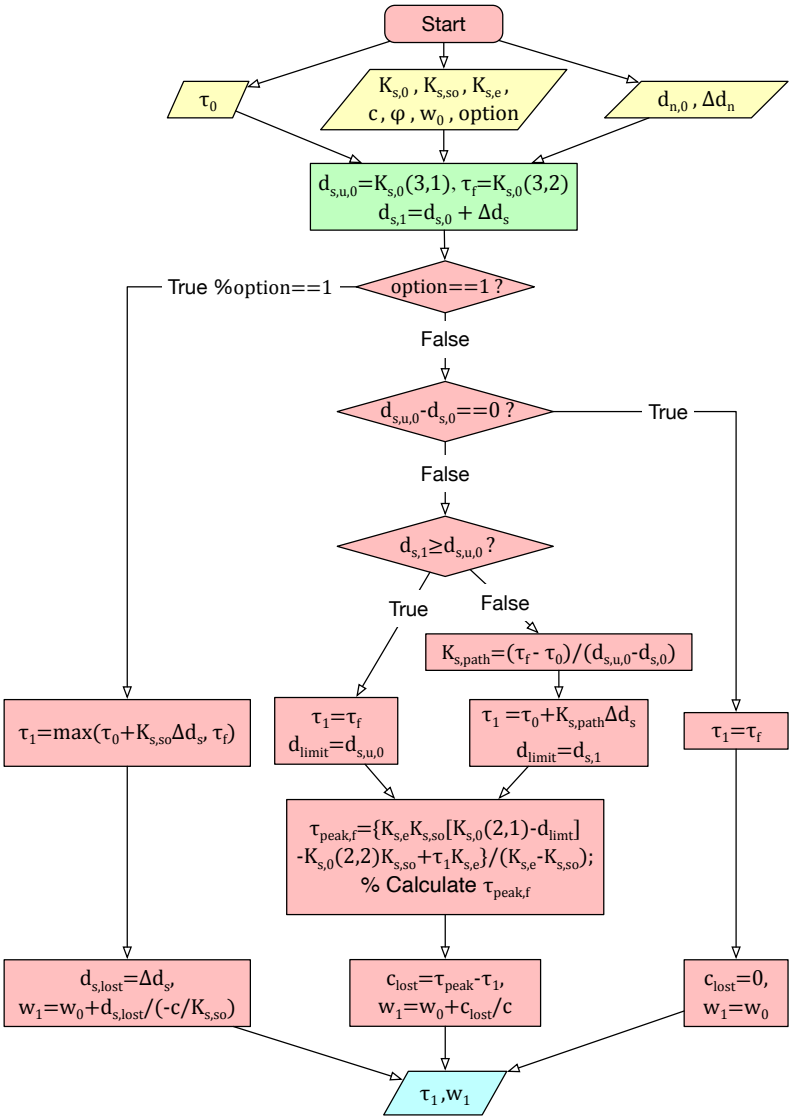

Figure 4.18: Shear Plastic Loader

In conclusion, the Tension, Compression and Shear Plastic Loaders calculate the possible normal stress or shear stress as a result of applying the sub-increment of relative displacement in its corresponding direction. The coupling effect is only considered when calculating the maximum capacity in that direction before applying the sub-increment of relative displacement. However, they do not consider the influence of the softening or the change of stress in one direction, after applying the increment of relative displacement in that direction, on the maximum stress capacity in the other direction. This is tackled with the sub-module of Damage Calculator in the next section.

4.6.3. Damage Calculator

The module of Damage Calculator is to consider the coupling effect after applying the increment of relative displacement in a direction, or in other words, after running the Tensile, Compressive, or Shear Plastic Loader module. The Damage Calculator, as shown in figure 4.19 below, is, in essence, an iterative calculator to calculate the softening effect coupled in tension and shear until the amount softening in shear and tension does not increase anymore. The theories behind each iteration can be referred to the two special cases in section 3.4.

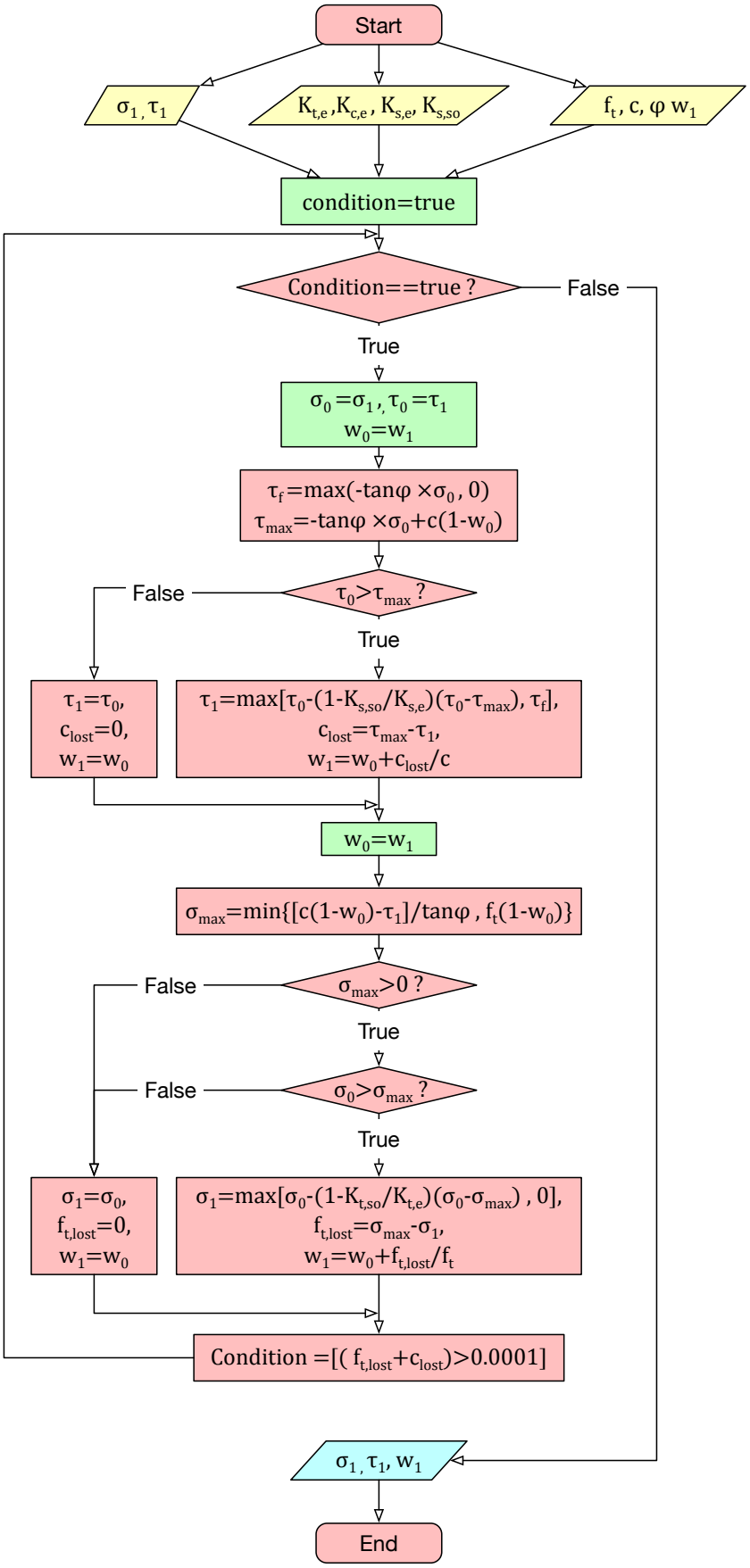

Figure 4.19: Damage Calculator

The structure illustrated above can be explained as the following. After obtaining the new damage factor w and new stresses in a specific direction (assumed to be A direction) by running the model of Tension, Compression or Shear Plastic Loader, the Damage Calculator is run. This module first calculates the maximum stress capacity in the other direction (assumed to be B direction) according to the Multi-surface Plasticity Criteria introduced in section 3.3.3. Then if the initial stress in the B direction is larger than the maximum stress capacity, the stress in B direction and the damage factor w will be recalculated. Similarly, after having the updated stress and the updated damage factor w in B direction, the stress capacity in A direction will be recalculated and be used to check if additional damage will occur in A direction. If it will, the stress in A direction and the damage factor w will also be updated. The calculation in these two directions will be performed iteratively until the value of shear stress, normal stress and damage factor converge. By doing so, the Damage Calculator ensures that each time after running this module, the stresses on both directions are on the yield surface defined by the damage factor w or w_c.

After running the Damage Calculator, a complete calculation process for a sub-increment in either shear or normal direction is finished. The uni-axial constitutive arrays, K_t, K_c and K_s, will be updated for the further elastic or plastic calculations, with the module of Constitutive Array Re-constructor introduced in section 4.2.

5

Qualitative verification on integration point level

In this chapter, this novel constitutive model is verified in single integration point level, which mainly checks if the model aligns with the mechanical understanding on the micro scale. Additionally, it also facilitates the reader to understand how this constitutive model actually works. In the next chapter, the verification of the full-scale FE wall model, with this constitutive model implemented, will be discussed to justify its performance on the macro level. The structure of the code mentioned in chapter 4 is written in both MATLAB and FORTRAN. The MATLAB code is used in this chapter, and the FORTRAN code will be used in the next chapter.

The MATLAB code is used for the verification on integration point level as MATLAB is more capable of plotting various figures to facilitate the verification process. To run the constitutive model, three simple uni-axial constitutive arrays in tension, compression and shear are assumed for a single integration point, as shown in table 5.1. Then, with the initial stresses, initial relative-displacements, and the increments of relative displacements in shear and normal directions, this constitutive model is run in MATLAB to calculate the resulted stresses and damaged for the increments of relative-displacement, as if this is what constitutive model module in FEA program calculates for each integration point. Figures are plotted to show the process of the calculation. Please note that all the values of the inputs and outputs, as well as the values on the axes of figures, do not have any realistic physical meaning. Therefore, they do not have corresponding units. One should not focus on the specific value but pay more attention to the overall mechanical behaviour of this integration point. For simplicity, the parabolic compressive curve is used with secant unloading and reloading ($\lambda = 0$).

The aims of this verification are listed below:

- Check if the resulted stress state and its path during the calculation process are reasonable or not on the plot of the uni-axial stress-relative displacement coordinate and the multi-surface plasticity criterion coordinate.
- Check if the sub-increments of relative-displacement in shear and normal directions are indeed required, or in other words, in which case the path dependency discussed in section 3.18 is true;
- Inspect the difference in terms of softening behaviour between the two Coupling Options introduced in section 3.3.3;
- Inspect the stability of the two iterative algorithms in this model: the Damage Calculator based on section 3.4 and the Bisection Solver in Elastic Finder.

Table 5.1: Initial tension, shear and compression arrays for MATLAB

K_t

0	0
$d_{ft} = 8$	$f_t = 8$
$d_{t,u} = 16$	0

K_s

0	0
$d_{s,peak} = (\tau_f + 20)/1$	$\tau_{peak} = \tau_f + 20$
$d_{\tau f} = (\tau_f + 20)/1 + 10$	τ_f

K_c

0	0
0	0
$d_{c,limit} = -4$	$\sigma_{c,limit} = -4$
$d_{fc/3} = -4$	$-f_c/3 = -4$
$d_{fc} = -20$	$-f_c = -12$
$d_{c,u} = -50$	0

The constitutive arrays shown in table 5.1 are generated with the input parameters listed below, with initial damage parameter in tension and shear $w^0 = 0$ and damage parameter in compression $w_c^0 = 0$.

- $K_{s,e} = 1$, elastic shear stiffness;
- $K_{t,e} = 1$, elastic tensile stiffness;
- $K_{c,e} = 1$, elastic compressive stiffness;
- $G_{f,s} = 300$, tensile fracture energy;
- $G_{f,t} = 64$, shear fracture energy;
- $G_{f,c} = 80$, compressive fracture energy;
- $\phi = 45°$, friction angle, $tan(\phi) = 1$;
- $c = 20$, cohesion;
- $f_t = 8$, tensile strength;
- $f_c = 12$, compressive strength;
- $ratio_{K,r} = 0$, ratio of residual stiffness of shear, tension or compression to their corresponding initial stiffnesses;
- $\lambda = 1$, unloading and reloading factor in compression to determine the proportion of unloading with initial stiffness vs secant stiffness.

These inputs are also the complete set of input parameters required for this constitutive model written in FORTRAN, which is used in the FEA program. In this section, their values are chosen evenly to facilitate the plots such that it would be easier to identify and monitor the calculation process. Therefore, they are not realistic and do not reflect any mechanical property of a masonry interface.

With these parameters, 11 sets of initial relative normal and shear displacements (d_n^0 and d_s^0) and their corresponding initial normal and shear stresses σ^0 and τ^0 are selected, ranging from combined tension and shear to combined compression and shear. Most of them are on the yield surface except for the No.6 and No.11, and all of them are with the damage factor $w = 0$ and $w_c = 0$. Every combination of increments of relative displacements in normal and shear directions leads to an elastic predictor pointing out of the yield surface in every possible direction, in order to test the algorithm of the Elastic Limit Finder and Plastic Calculator. An overview of the initial (d_n^0, d_s^0, Δd_n and Δd_s) and calculated values (σ^0, τ^0, w^1 and w_c^1) of these 11 tests are shown in table 5.2 below.

Table 5.2: Overview of initial and calculated values of tests on single integration point level

No.	Dir.	Original relative displ.	Increment of relative displ.	Need Sub-increments ?	Coupling Option	Identical result for two options?	Number of sub-increments											
							2				20				200			
							σ^1	τ^1	w^1	w_c^1	σ^1	τ^1	w^1	w_c^1	σ^1	τ^1	w^1	w_c^1
1	n	8	1	no	Option 1	yes	0.3333	0.5	0.9583	0	0.3333	0.5	0.9583	0	0.3333	0.5	0.9583	0
	s	12	1	no	Option 2		0.3333	0.5	0.9583	0	0.3333	0.5	0.9583	0	0.3333	0.5	0.9583	0
2	n	4	1	no	Option 1	no	3	9.5	0.375	0	3	9.5	0.375	0	3	9.5	0.375	0
	s	16	1	yes	Option 2		3.0252	9.5189	0.3728	0	3.0195	9.5146	0.3733	0	3.0188	9.5141	0.3734	0
3	n	8	-3	no	Option 1	no	5	9	0.3	0	5	9	0.3	0	5	9	0.3	0
	s	12	6	yes	Option 2		2.8359	6.3542	0.5405	0	2.5965	4.9694	0.6317	0	2.5632	4.7995	0.6319	0
4	n	4	4	yes	Option 1	yes	0	0	1	0	2.4	3.5	0.7	0	2.64	3.95	0.67	0
	s	16	-2	yes	Option 2		0	0	1	0	2.4	3.5	0.7	0	2.64	3.95	0.67	0
5	n	4	3	yes	Option 1	no	2.5	4.375	0.6187	0	3.85	7.4125	0.4331	0	3.985	7.7163	0.4146	0
	s	16	-1.5	yes	Option 2		3.7624	5.3225	0.5082	0	4.6113	7.9835	0.3665	0	4.7011	8.2533	0.3519	0
6	n	8	0.7	no	Option 1	yes	3.9667	5.95	0.5042	0	3.9667	5.95	0.5042	0	3.9667	5.95	0.5042	0
	s	11	1.2	no	Option 2		3.9667	5.95	0.5042	0	3.9667	5.95	0.5042	0	3.9667	5.95	0.5042	0
7	n	-4	3	no	Option 1	yes	-1	9	0.6	0	-1	9	0.6	0	-1	9	0.6	0
	s	24	3	no	Option 2		-1	9	0.6	0	-1	9	0.6	0	-1	9	0.6	0
8	n	-4	-10	no	Option 1	yes	-10.88	14.625	0.8125	-1.719	-10.88	14.625	0.8125	-1.719	-10.88	14.625	0.8125	-1.719
	s	24	15	no	Option 2		-10.88	14.625	0.8125	-1.719	-10.88	14.625	0.8125	-1.719	-10.88	14.625	0.8125	-1.719
9	n	-1	2	no	Option 1	no	0	6.5	0.675	0	0	6.5	0.675	0	0	6.5	0.675	0
	s	21	2	no	Option 2		0	10.25	0.4875	0	0	10.25	0.4875	0	0	10.25	0.4875	0
10	n	-4	4	yes	Option 1	yes	0	13	0.3	0	0	15.7	0.21	0	0	15.97	0.201	0
	s	24	-2	yes	Option 2		0	13	0.3	0	0	15.7	0.21	0	0	15.97	0.201	0
11	n	-4	-25	no	Option 1	yes	-10.92	22.76	0.408	-1.73	-10.92	22.76	0.408	-1.73	-10.92	22.76	0.408	-1.73
	s	20	15	no	Option 2		-10.92	22.76	0.408	-1.73	-10.92	22.76	0.408	-1.73	-10.92	22.76	0.408	-1.73

5.1. Calculation process

This section is to inspect the calculation process of the Plastic Calculator. To better identify the change of shear and normal stresses, three figures were plotted during the process with two sub-increments. For instance, for the Test No.1 with Coupling Option 2, the evolution of the stresses and relative displacements at each stage of calculation, as well as the corresponding uni-axial constitutive curves in shear and tension, are illustrated in figure 5.1 with dots and line, respectively. The left one is in normal direction while the right one is in shear direction. Figure 5.2 shows the change of the yield surface and the corresponding stress state. The common legend for these three graphs is shown in figure 5.3.

To be more straightforward, all the shapes and lines in blue in these figures represent the calculation related to the application of normal sub-increments, while magenta related to the application of the shear sub-increments. All the hollow diamond patterns are the returned stress states related to the uni-axial loading process (the Normal Loader and the Shear Loader), and all the circles are related to the Damage Calculator.

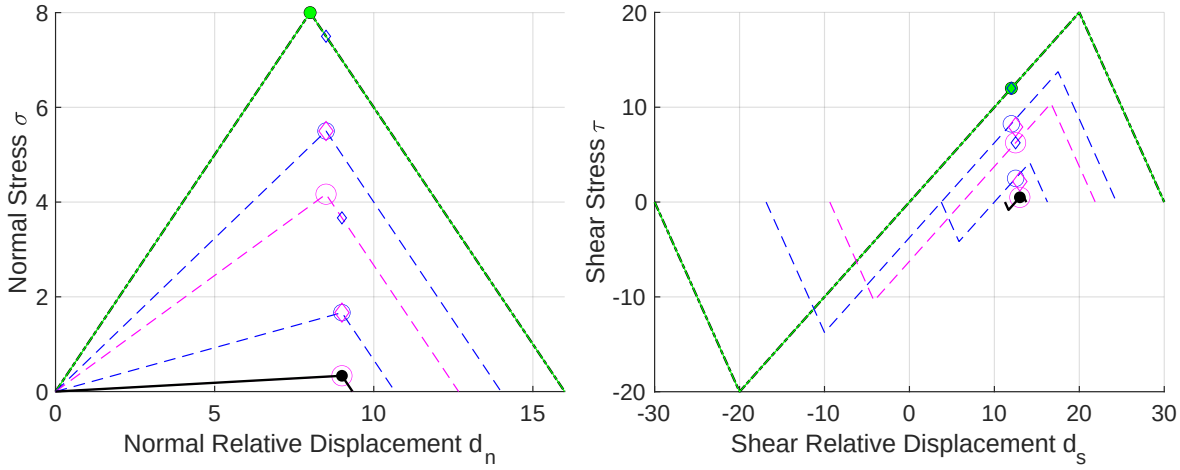

Figure 5.1: Change of stresses in calculation process of Test No.1 with Coupling Option 2 on uni-axial stress-relative displacement coordinate

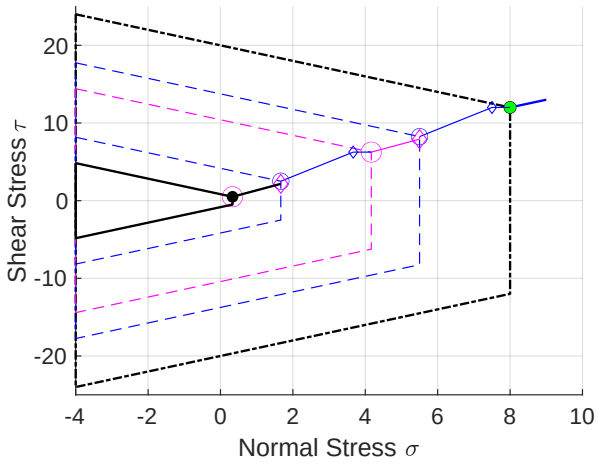

Figure 5.2: Change of stresses in calculation process of Test No.1 with Coupling Option 2 on shear stress-normal stress coordinate

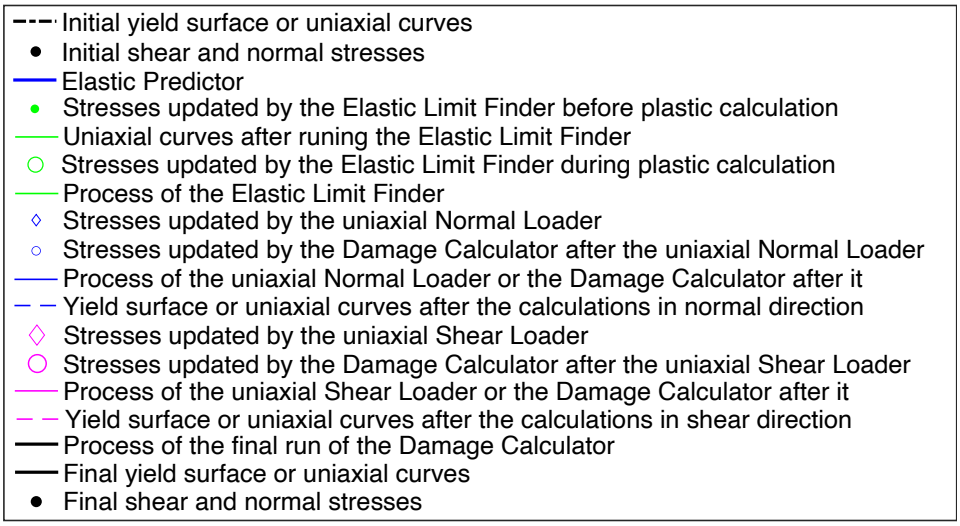

Figure 5.3: Common legend for figures in uniaxial coordinates and shear stress-normal stress coordinate

The black dashed lines represent the initial state of the uni-axial tensile constitutive curve, the shear constitutive curve and the intact yield surface. The green solid dot marks the elastic limit stress state right before it gets out of the yield surface. For all the tests, the initial stress states can actually be represented by these green solid dot, as they are already on the yield surface, which means the black solid dot is overlapped by the green solid dot. The green line on figure 5.1 is just the corresponding uni-axial constitutive curve corresponding to the green solid dot. More generally, if the initial stress state is within the yield surface and it is going to be loaded plastically, the location of the green solid dot and the green lines, which represent the elastic limit stress state on the yield surface, together with its corresponding uni-axial constitutive curves, will be determined by the module of Elastic Limit Finder introduced in section 4.5 with iterative algorithm. In the current case, this is unnecessary.

In addition, due to some very subtle or even no change of location of the patterns, some lines or the patterns might be overlaid by others. And also, some patterns are not shown here as they do not take place in the current case. However, there must be some other cases in these 11 tests that actually show these lines or patterns. Please refer to Appendix B for the results for all the tests.

In the current case, according to the Elastic Predictor, as is discussed in section 4.3, the increments of the relative displacement in normal and shear directions will result in a stress state outside the yield surface, which is shown with a blue solid line pointing outwards in figure 5.2. This triggers the run of the Plastic Calculator introduced in section 4.6. In this situation, conventional Elastoplastic Constitutive Models will usually map the elastic predictor back to the yield surface with some matrix manipulation that is not stable or robust at the corner of the yield surface. This novel constitutive model does not have the mapping back process but uses a combination of sub-increments and some iterative algorithms to achieve a much more robust calculation, which is the essence of this model. This process is drawn in blue and magenta in figures 5.1 and 5.2. Before the plastic calculation starts, the initial increments of relative displacements are divided into two sub-increments, in this case, considering the possible path dependency effect mentioned in section 3.5. This means that the same iterative algorithm will be run twice to get the final result.

In the first round, the first sub-increment in normal direction is applied, and the normal stress is updated with the Normal Loader described in section 4.6.1 with Coupling Option 2. The updated stress is represented by the blue hollow diamond, depicted in the three figures. Particularly in figure 5.2, a short blue line links the green solid dot to the small blue hollow diamond pattern to show the plastic uni-axial loading process in normal direction. The line is horizontal, meaning that the shear stress has not changed for this stage. This could also be double-checked by the completely same location of green solid dot and the blue hollow diamond on the right figure in shear direction of figure 5.1. Then, as is

discussed in section 3.4, the reduction of tensile stress represents some damage to the interface in normal direction, and because the tension and shear damage is coupled in this constitutive model, the slightly damaged interface is no longer able to carry the current shear stress. Therefore, the Damage Calculator is run using an iterative method to calculate the extra damage caused by this overwhelming shear stress that exceeds its capacity. This is introduced in section 4.6.3. The module of Damage Calculator returns a new set of normal and shear stresses, which are plotted with big blue circles in these three figures above. Also, an inclined blue line is plotted linking the small blue diamond to the big blue circle, representing the reduction in shear and normal stress calculated iteratively by the Damage Calculator. Before the calculation of the first normal sub-increment is finished, the last step is to update the uni-axial constitutive arrays using Constitutive Array Re-constructor mentioned in section 4.2. The updated tension and shear arrays are plotted with blue dashed lines in figure 5.1. Additionally, the new yield surface is plotted in figure 5.2 with blue dashed lines, because both the Normal Loader and the Damage Calculator have already updated the damage factor w shared between tension and shear.

Secondly, the first sub-increment of relative shear displacement is applied by the Shear Loader introduced in section 4.6.2 also with the Coupling Option 2. The Shear Loader updates the shear stress while the normal stress remains unchanged, as is shown with big magenta hollow diamonds in all three figures. In the right figure in shear direction of figure 5.1, we could see the magenta hollow diamond is slightly shifted from the blue big circle to its the bottom right corner with slope equal to the softening stiffness. This is exactly what we defined for the Coupling Option 2 in section 3.3.3 when the normal stress limits the maximum shear capacity of the interface at that moment. Looking at the left figure in normal direction, the magenta diamond remains at the same location as the blue big circle because normal stress should not change in the uni-axial loading process. This is also shown in figure 5.2 that the blue big circle moves vertically to become the magenta diamond. As the change of location is so tiny, the plotted magenta solid line vertically linking the blue circle to the magenta diamond can hardly be seen in this plot. After the uni-axial plastic loading in shear, the Damage Calculator is run again to calculate the extra damage, because the damage caused by uni-axial shear plastic loading makes the interface unable to carry the current normal stress. This process then updates the stresses in both directions and the damage factor w. The Damage Calculator is illustrated in figure 5.2 with an inclined magenta solid line ending at the magenta circle representing the final stress state after the application of first shear sub-increment. The updated yield surface is also drawn with magenta dashed lines according to the updated damage factor w in the same figure. The magenta circle is on the updated yield surface, which is reasonable. Also, the tension and shear arrays are updated with Constitutive Array Re-constructor and plotted in figure 5.1 with magenta dashed lines, with the magenta circles on each of them. From both the normal and shear figures, we can see that the magenta circle is shifted vertically downward from its predecessor, the magenta hollow diamond. This verifies that the Damage Calculator can reduce both the tensile and shear stress to ensure that the combination of them, the stress state, is on the new yield surface.

At this moment, the first sub-increments of the relative normal displacement and relative shear displacement have been applied. Afterwards, the aforementioned process is repeated for the second set of sub-increments of the relative normal and shear displacement. If the increments of relative displacements are divided into n sub-increments, this process will be repeated for n times. After the last time that the Damage Calculator is run, black solid lines will be plotted (figure 5.2). And the final yield surface is also plotted with black solid lines to declare the end of the Plastic Calculator process. On the uni-axial coordinate, the final updated uni-axial constitutive arrays are also plotted (figure 5.1). Each of these figures has a black solid dot that represents the final normal stress, final shear stress, or the final stress state as a combination of them after running this constitutive model.

In Appendix B, all figures for the 11 tests with both Coupling Option 1 and 2 are carefully inspected to ensure that the algorithm of this novel constitutive model can be run as expected and without mistake. Because these 11 tests are chosen to cover most of the possible cases of plastic loading process, it can be concluded that the algorithm is stable and robust on the integration point level. Besides, the following observations of all these plastic calculations also tell the consistency between the calculation process and the understanding of the mechanics:

- If the last round of the calculation involves unloading in shear direction, the final stress state (the black solid dot) will be slightly inside the yield surface. This is clearly the case, especially with only two sub-increments, such as Test No.5 and No.10. It is contradictory with respect to the mechanics because, at the end of any plastic process, the final stress state should be nowhere else but on the yield surface. However, as the number of sub-increments increases, the proportion of the final shear unloading becomes smaller and smaller. Finally, with a sufficient number of the sub-increments, the distance between the final stress state and the yield surface is negligible, and we could say that it complies with the principle mentioned above. Of course, for all other cases, the final stress state is literally on the yield surface.
- If the initial stress stage is close to the corner and the elastic predictor points to the corner region, like in Test No.1, No.6 and No.8, after the calculation, the final stress state is exactly at the corner of the updated yield surface. This is consistent with mechanics as both the shear and tension loading processes will damage the interface, and the interface will take the maximum amount of shear or tensile stress it can after softening in both directions. It must be impossible if, after all the damage, the stress state of the interface is on the tension cut-off of the yield surface between two corners, and it still can be further loaded in shear elastically. However, even if the initial stress state is at the corner, the final stress stage could be on the tension cut-off but not at the corner, if it is unloaded in shear. Finally, the final stress state could be on the compression cut-off if it is unloaded in shear or the amount of loading in shear is relatively small, which is the case in Test No.11, thanks to the hardening process of compression that further increases the shear capacity for a while.

The other important observations, namely the convergence and path dependency, will be discussed in detail in the following section.

5.2. Coupling Options

Two Coupling Options introduced in section 3.3.3 directly determine the rate of reduction of stresses and the increase of damage factor w in the uni-axial plastic loading process, namely the Normal Loader and the Shear Loader. Indirectly, these calculated stresses and damage factor influences the further calculation of stresses and damage factor in the Damage Calculator.

To be more specific, the Option 1 uses the initial softening stiffness to calculate the new stresses. These stresses decrease with a faster rate than the Option 2, which maintains the initial ultimate relative displacement and uses a gradually decrease softening stiffness. Therefore, the stresses updated by Option 1 is lower than or equal to Option 2. Accordingly, the damage factor w calculated by Shear Loader or Normal load with Coupling Option 1 is larger than the those with Option 2, meaning that the residual cohesion and tensile strength is lower for Option 1 than Option 2. Then these calculated variables are passed to Damage Calculator. Theoretically, the more difference between the updated stresses and the residual cohesion and tension strength will lead to more extra damage. However, Option 1 has lower stresses but also less residual cohesion and tensile strength, while Option 2 has higher stresses but also more residual cohesion and tensile strength. Therefore it is difficult to tell which of the combinations will induce more extra damage.

Of course, if the elastic limit stress calculated by the Elastic Limit Finder is already at the peak of the uni-axial constitutive curve before it is loaded plastically, both Option 1 and Option 2 will provide exactly the same updated stress and damage parameter. This is because when the initial stress is at the peak, the Option 1 of preserving its initial softening stiffness and the Option 2 of preserving its initial ultimate relative displacement are the same. Also, this is consistent with the understanding of mechanics.

For example,

- Test No.1 (figure B.2 B.3), No.4 (figure B.8 B.9) and No.6 (figure B.12 B.13) provide an identical

final result for both Options, although differences exist during the process.

- Test No.2 (figure B.4 B.5) and No.3 (figure B.6 B.7) show that although the uni-axial plastic loaders of Option 2 provide smaller update stresses and higher damage parameter at first, the damage calculator further reduces the stress from Option-2 uni-axial plastic loader to a very low value which make the final stresses smaller than those with Option 1, which also mean the damage of Option 2 is more serious than Option 1.
- Test No.5 (figure B.10 B.11) shows that both of the Normal Loader and the Damage Calculator causes more damage on Option 1 than Option 2.
- Because the Coupling Options are designed for combined tensile and shear loading problem, it would be no difference between them if the calculation is purely compression and shear, which are Test No.7 (figure B.14), No.8 (figure B.15), No.10 (figure B.18), and No.11 (figure B.19 B.20). For Test No.7, No.8 and No.11, the shear loading processes all begin with the elastic shear limit located at the peak of the uniaxial shear constitutive curve, and the No.10 is shear unloading. Therefore Option 1 and 2 are the same for the entire process.
- Test No.9 (figure B.16 B.17) is special as it shifts from combined shear and compression to combined shear and tension. For the compression part, two Options are the same. For the tension part, it behaves similarly as the Test No.5.

The inspection described above verified that the core components of the plastic calculator perform as expected. However, which of the two Options is more realistic is still too early to say until some validations against experiments are done on structure level where cohesion and tensile strength play a more critical role than friction. Also, note that one of the Coupling Options might be more suitable for some certain types of material while the other Option fits some other materials better.

5.3. Path dependency and convergence rate

As is discussed in section 3.5, the possible path dependency effect is one of the main reasons that this constitutive model introduces sub-increment. For all eleven tests, the same analyses have been conducted with 2, 20 and 200 sub-increments to check in which cases path dependency exists, or in other words, in which case sub-increments are required. The definite conclusion is that it is necessary to implement this idea of sub-increment because it is required in 5 out of 11 tests conducted here. One of the important aims of this model aims is to make it least dependent on the size of the steps in FE analysis. If this constitutive model is implemented without sub-increments, the change of step size will have a more significant influence on the result. In that case, in order to ensure better accuracy, more steps would be required, and that would increase the computational time and memory consumption. It is, therefore, wiser to include these extra sub-increments than to have a model dependent on the step size, that would require experienced users and sensitivity tests in order to achieve good accuracy in the results.

Table 5.2 shows that for most of the cases[1] (9 out of 10) with positive increments of relative displacements in both shear and normal directions[2], they do not need sub-increments. However, Test No.2 with Coupling Option 2 is an exception. For those tests with increments of relative displacements with opposite signs in shear and normal directions, they are usually path-dependent, and sub-increments are required (8 out of 12), except for Test No.3 with Coupling Option 1, Test No.8 and Test No.11. Further studies will be needed to tell why and when they are needed for this algorithm.

In the current implementation, this model will perform the Plastic Calculator analysis with 2 and 3 sub-increments automatically and check if they provide identical outcomes. If they do, the program will

[1] Each of the 11 tests has two cases. One of these two cases is with Coupling Option 1, and the other is with Coupling Option 2. Therefore, in total, there are 22 cases.
[2] Positive increments of relative normal displacement mean unloading in compression and loading in tension.

return these outcomes as the final results. Otherwise, the number of sub-increments defined by the user will be applied to get more reliable results. This helps save computational time.

Naturally, it is not suggested that path dependency does not exist in reality for the cases that do not need sub-increments in the analyses with this constitutive model. The conclusion drawn above is only valid in the context of this constitutive model with the certain amount of coupling effect and damage mechanism assumed. In reality, the coupling effect could be much more complicated, and it could be possible that all plastic processes are path-dependent, as discussed in section 3.5.

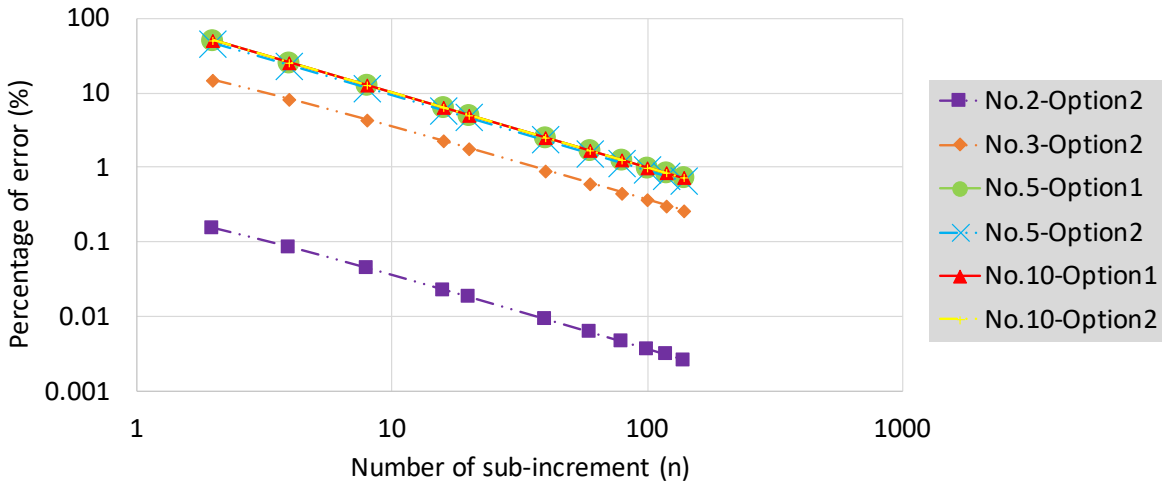

Figure 5.4: Convergence rate of the test required sub-increments

For those cases that sub-increments are required, it is crucial to ensure its stability such that the result will not diverge. All the tests, including those which are not presented in this thesis, have never encountered any divergence problem with the increase of the number of sub-increments. Also, with 2000 sub-increments, the results for all the tests are already extremely close to the exact value, and they are used as a reference value. With the number of sub-increments ranging from 2 to 140, the cases that require sub-increments are run. The percentage of the error with respect to the reference value are plot in figure 5.4 versus the number of sub-increments, in log-log scale. As the error of Test No.4 is exactly the same as Test No.10, they are not drawn in this figure. From the figure, we can see that the convergence rate is $O(n^1)$, and it is acceptable. For the analysis afterwards, the number of sub-increments is set to 100 if it is required.

5.4. Summary

In this chapter, the qualitative verification is conducted on the integration point level to inspect the correctness of the algorithm, the difference in Coupling Options, the path dependency, and the convergence rate of refining the sub-increments. All of them show that the proposed constitutive model runs well and stably as expected in various loading cases. Also, the process of the analysis is visualized with MATLAB plots to show how it really works.

In the next chapter, the verification will be conducted on the full-scale FE wall models, with this constitutive model implemented. This will justify its performance on macro level, by comparing the FEA results with the experimental data.

6

Quantitative verification on wall level

This constitutive model is written as a user-supplied subroutine for DIANA in FORTRAN. The validation of the constitutive model on structural components (walls) is done against the experimental results of three walls tested quasi-statically in-plane at TU Delft. The components chosen have different geometrical and/or boundary conditions, and each one represents a different type of in-plane failure: shear failure, flexural failure, and combined shear and flexural failure. They are named as COMP_4, COMP_3 and COMP_6 respectively. The common specifications of these three analyses conducted in the FEM program DIANA are:

- The discrete crack models of the walls are composed by the linear elastic plane stress elements `Q8MEM`, representing the bricks, and the nonlinear 2D line interface elements `L8IF`, representing the head joints and the bed joints. The dimensions of the plane stress elements are 111.11mm x 40.58mm, whereas the length of the 2D line interface elements is 111.11mm for the bed joints and 40.58mm for the head joints.

- All the walls have the same material properties. The effect of gluing the top and bottom edges of the wall to the frame during the experiment, are not considered here. The top and bottom nodes are tied with the first node on the same edge, assuming that they move identically in the horizontal direction.

- In the first five load steps, the pre-compression and the dead weight are applied. Then, a series of prescribed lateral displacements at the top left corner is applied.

- A quasi-static, implicit, nonlinear analysis is performed with the secant iteration scheme, taking physical nonlinear behaviour into account. The geometrical nonlinearity is neglected as it barely influences the result.

- Both the displacement and force based convergence criterion are applied with standard DIANA tolerance values (0.01). The analysis terminates if it does not satisfy the convergence criterion. However, this does not happen in any of the analyses.

- The numerical results, including the horizontal top displacement-shear reaction force diagram and the crack pattern, are compared with the data obtained from the experiments conducted on these three walls.

- The Compressive Curve of the Engineering Masonry Model is used for compression, and the Coupling Option 1 is used for the coupling effect between tension and shear.

Table 6.1: Input parameters for plane stress elements for bricks

Elastic modulus E_u	Poisson's ratio ν	Density ρ
$8990MPa$	0.14	$1.805 \times 10^{-9} T/mm$

The input parameters for the bricks are shown in table 6.1, assuming they are elastic throughout the analysis. The parameters in table 6.2 are the inputs, namely the USRMATs, for the user-supplied subroutine of interface elements in the discrete crack models. The values of these parameters are estimated based on material tests conducted in TUDelft [2]. The initial shear stiffness $K_{s,e}$ for bed joints could be estimated from the triplet test. The shear stiffness $K_{s,e}$ of the head joints is reduced from the one of the bed joints, considering the lack of pre-compression in the horizontal direction during the construction of the wall. The initial compressive stiffness $K_{c,e}$ for head joints is calculated with equations 3.8 and 3.10 with $E_m = E_2$ and $E_u = E_b$. The E_2 and E_b are the secant elastic modulus of the masonry wall evaluated at 1/10 of the maximum stress and the elastic modulus of the brick respectively derived from the material tests. The $K_{t,e}$ is assumed to be the same as $K_{c,e}$. The $K_{c,e}$ and $K_{t,e}$ of bed joints are calculated in the same manner. For convenience, an overview of the results obtained from the material tests is presented in appendix C.

Table 6.2: Input parameters for zero-thickness interface elements

Parameter	bed joint	head joint	Unit	USRMAT No.
$K_{s,e}$	39.31	16.36	MPa/mm	USRMAT(1)
$K_{t,e}$	121.16	10.44	MPa/mm	USRMAT(2)
$K_{c,e}$	121.16	10.44	MPa/mm	USRMAT(3)
$G_{f,s}$	3.0	0.1	N/mm	USRMAT(4)
$G_{f,t}$	7.75×10^{-3}	7.75×10^{-4}	N/mm	USRMAT(5)
$G_{f,c}$	15.0	34.0	N/mm	USRMAT(6)
ϕ	23.27	23.27	∘ circular degree	USRMAT(7)
c	0.140	0.014	MPa	USRMAT(8)
ft	0.1050	0.0035	MPa	USRMAT(9)
fc	5.93	8.10	MPa	USRMAT(10)
$ratio_{K,r}$	0.0001	0.0001	dimensionless	USRMAT(11)
λ	0.95	0.95	dimensionless	USRMAT(12)
$d_{c,peak}$	0.89727	3.30820	mm	USRMAT(13)

Both fracture energy $G_{f,s}$ and $G_{f,t}$ are assumed with reasonable values. The fracture energy of compression $G_{f,c}$ is calculated to have equivalent energy dissipation as the compression test conducted, logged as G_{f-c} and $G_{f-c,h}$ in the appendix C. The assumption behind is that the energy dissipated in the elastic and hardening regime is contributed by all the mortar joints, while the energy dissipated in the softening branch is concentrated in the mortar layer with the highest imperfection. The friction angle phi and cohesion c of the bed joints are obtained directly from the material test, named as Masonry initial shear strength $f_{v,0}$ and shear friction coefficient μ. The cohesion of the head joints is assumed to be $1/10$ of the bed joints. The tensile strength f_t of bed joints or head joints is assumed to be lower than the corresponding cohesion, but the parameter study in chapter 7 will show that the tensile strength is not important. However, please note that the tensile strength f_t should not be larger than $c/tan\phi$; otherwise, the shape of the multi-surface plasticity criterion will be incorrect.

The compressive strength f_c of the bed joints is obtained from f'_m in the compressive test of the vertical wall. The f_c of the head joints is estimated by the FE model of the horizontal wall, as shown on the left side of figure 6.1, to have the same compressive capacity as the compressive test of the horizontal wall. Therefore the value of f_c is slightly higher than the $f_{m,h}$ from the test as the mortar layers are

interrupted by bricks. The relative displacement where the compressive stress of the bed joints or the head joints reaches the peak, namely the $d_{c,peak}$, is adjusted such that the result of each of the FE analyses shown in figure 6.1 will have same peak location as the corresponding test (figure 6.2). Note that for the model, the orange nodes are tied to the red node on the same horizontal line such that they have identical vertical translation. And the proposed constitutive model is used with all the above parameters as inputs. Note that the parameter $d_{c,peak}$ is only meaningful if the Compressive Curve of the Engineering Masonry Model used.

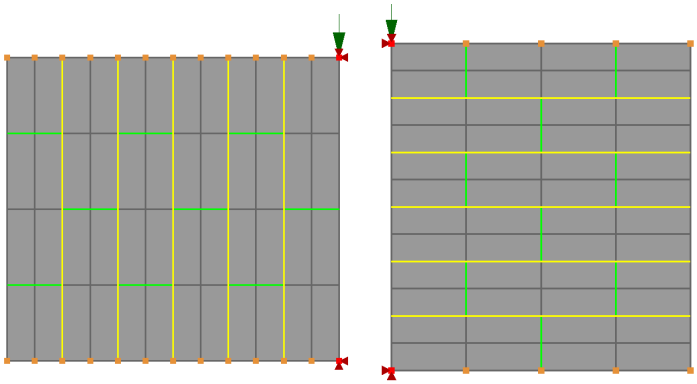

Figure 6.1: FE model of the conducted compressive test of the horizontal wall (left) and vertical wall (right)

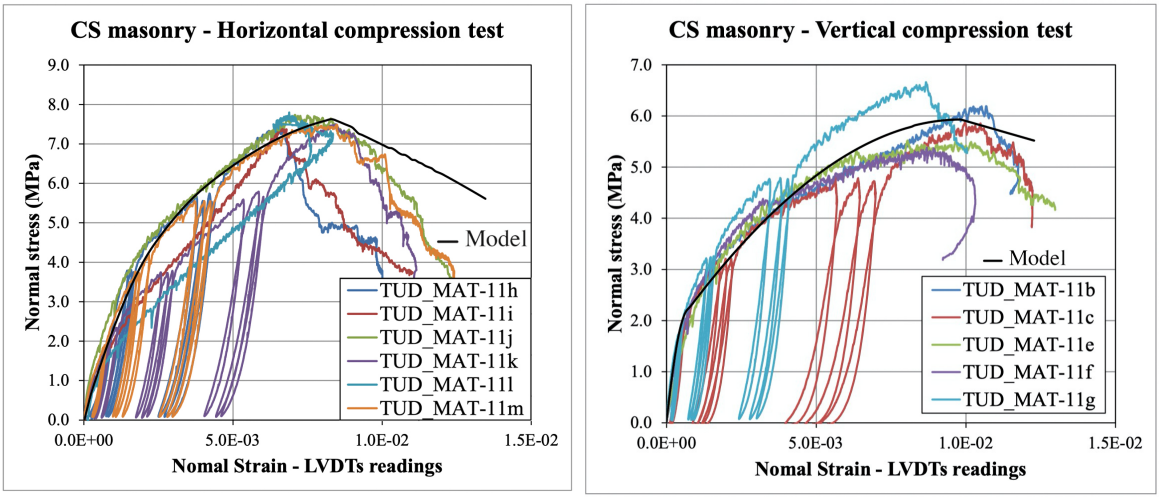

Figure 6.2: Stress-strain curve of the compressive test taking into account their height (Left: horizontal wall; Right: vertical wall).

Also, from figure 6.2, it is clear that the pre-peak curve is consistent with the experiment result. The post-peak branch deviates from the experiment since these two models do not include imperfections and all mortar layers contribute to the post-peak energy dissipation, which makes it unreal here. This hardly happens in the models of COMP_4, COMP_3 and COMP_6.

The parameter $ratio_{K,r}$ is the ratio of residual stiffness to its initial stiffness for shear, tension or compression, when the cohesion, the tensile strength or the compressive strength is completely depleted. It is set to a relatively small value such that it has little influence on the overall result, but more importantly, it mitigates possible ill-conditioning of the stiffness matrix. The parameter λ is the proportion of the unloading process with initial stiffness to the entire unloading process in compression. For the rest of the unloading process, secant unloading will be used until the relative displacement is back to 0. For reloading, it follows the same path as unloading. This parameter is critical for a more accurate prediction of the energy dissipation.

For an example of the input file used for DIANA FE analysis, please refer to Appendix E. All the input material parameters USRMATs, integer indicator variables USRINDs and state variables USRSTAs are explained in Appendix D.

For each analysis, the following aspects are inspected:

- Initial stiffness
- Stiffness at the end of the loading procedure
- Loading capacity
- Energy dissipation
- Crack pattern
- Degradation when loaded 3 times in a cycle
- Failure mechanism

6.1. Shear failure (Double fixed test COMP_4)

COMP_4 is a quasi-static in-plane cyclic test performed at the TU Delft [12]. The specimen is $4.0m$ wide, $2.76m$ high, and $102mm$ thick. The overburden stress of $0.3MPa$ is applied. The wall was tested under double clamped boundary conditions.

For the model of the test COMP_4 (figure 6.3), the bottom edge is tied to the bottom left node with translations restricted in all directions. The nodes along the top edge are tied to the top left corner in both directions to ensure identical horizontal and vertical translation. In the first five steps, the vertical concentrated load (blue arrow) is applied at the top left corner and will be properly distributed to all nodes on the top edge due to the requirement for equal displacements. The deadweight of the wall is also applied in these five steps. After the first five steps, a series of horizontal prescribed displacement (green arrow) is applied to achieve cyclic loading with increasing cycle amplitudes ranging from $0.25mm$ to $5.5mm$.

The green lines and the yellow lines represent the zero-thickness interface elements for the head joints and the bed joints respectively. The proposed constitutive model is used for the interface elements with the 13 parameters listed in table 6.2. The grey plane stress elements are assigned with the linear elastic parameters in table 6.1.

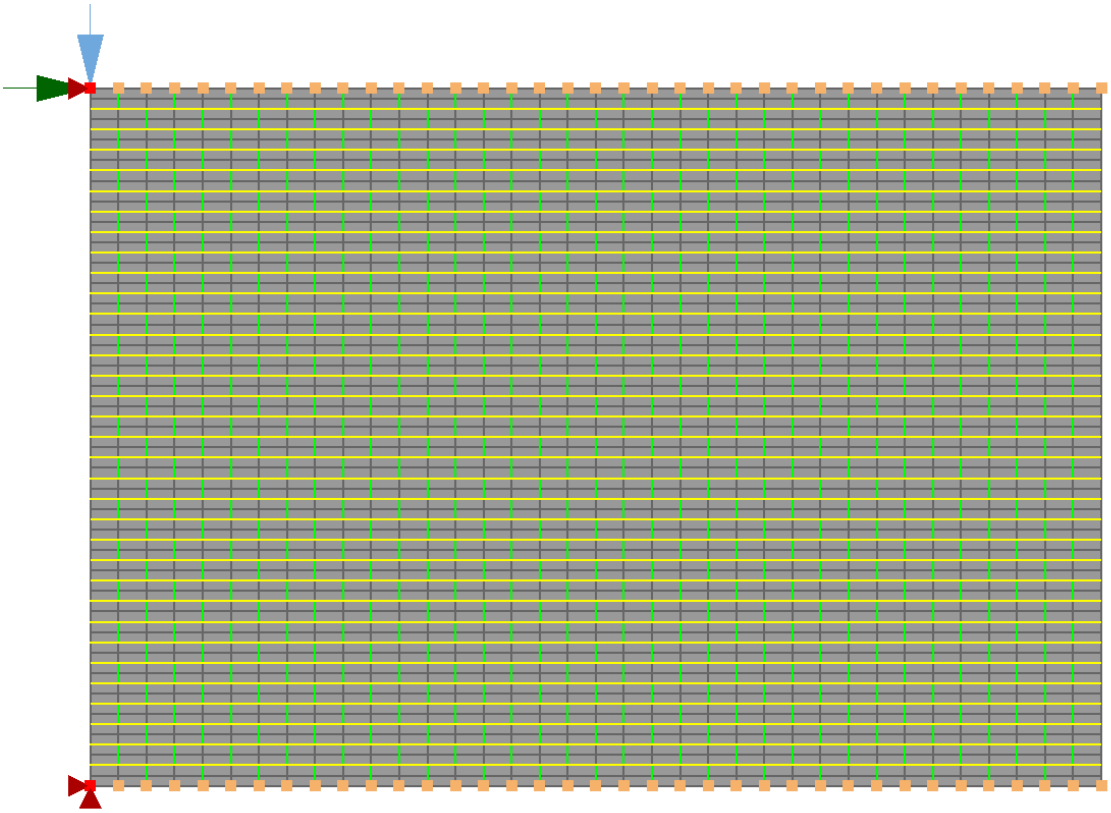

Figure 6.3: Finite element mesh with supports, loading for COMP_4 test

Figure 6.4 shows the crack pattern of the experiment in comparison with the crack in the analysis at the time of the largest lateral displacement ($5.5mm$). In the experiment, very strongly localized staircase cracks extending from the four corners towards the center of the wall can be recognized. The deformed mesh of the analysis also shows concentrated large relative displacements of the interface elements along the diagonal. The maximum value of the relative normal displacements of the interface elements can be regarded as the crack size because it is much greater than the relative displacement

corresponding to the tensile strength of the tensile constitutive curve.

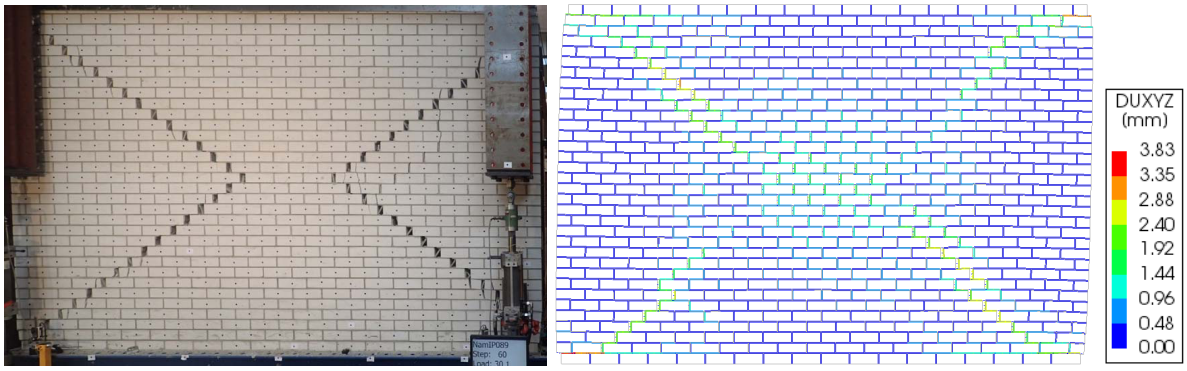

Figure 6.4: Observed crack pattern in experiment of test COMP_4 and the absolute value of relative displacement of the interface in deformed mesh for COMP_4 (scaling factor=10)

To be specific, in the analysis, the relative displacement of the interface in both shear and normal directions of the bed and head joints are illustrated in figure 6.5 and 6.6 respectively. Figures are captured when the wall reaches its maximum shear displacement at the top (5.5mm). From the relative shear displacement of the bed joints and the relative normal displacement of the head joints, we can observe the stair-case cracks developed from the corner. The diagonal crack from the top right to the bottom left corner is smaller than the other diagonal, since the crack is closing when loading the wall in the right direction. The maximum size of the tensile crack (2.89mm) of the head joints seems to be smaller than the experimental one. This can be related to a greater number of dispersed micro-cracks at the center of the wall in the analysis than the experiment. The relatively small values of tensile (0.7mm) or compressive (-0.68mm) relative displacement of the bed joints also confirm that it is a shear failure dominated mechanism.

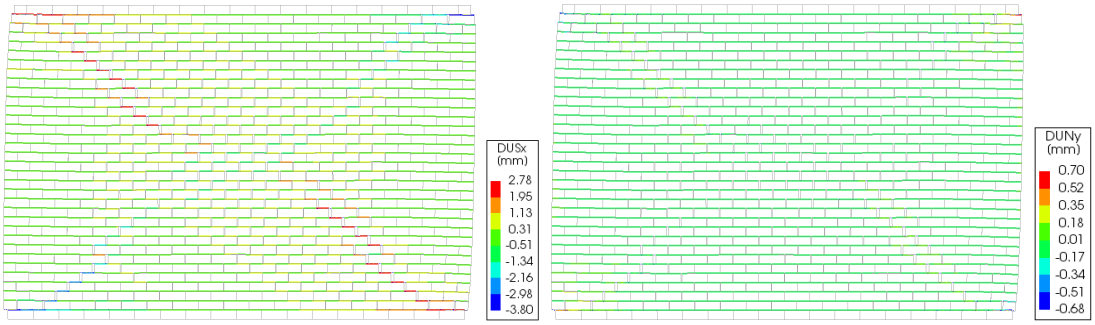

Figure 6.5: Shear (left) and normal (right) relative displacement of bed joints under largest shear deformation in deformed mesh for test COMP_4 (scaling factor=10)

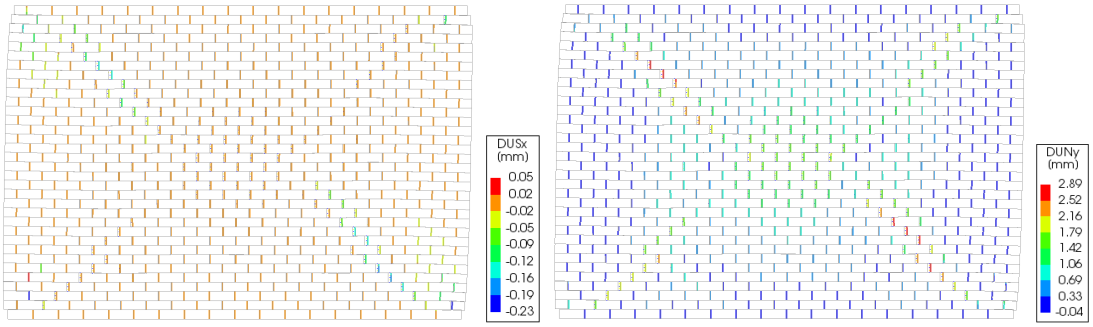

Figure 6.6: Shear (left) and normal (right) relative displacement of head joints under largest shear deformation in deformed mesh for test COMP_4 (scaling factor=10)

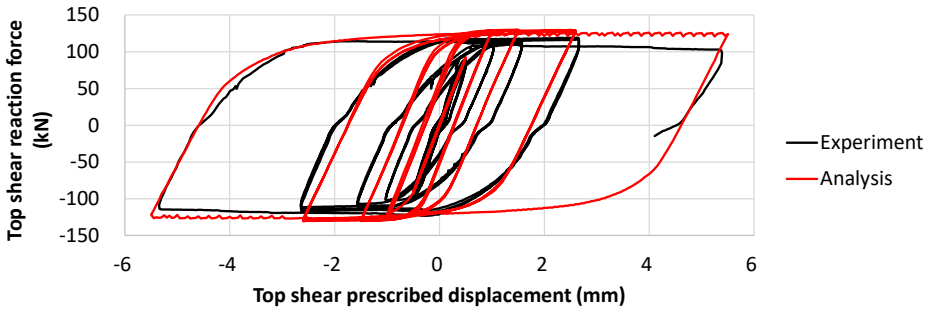

Figure 6.7: Force displacement diagram from DIANA simulation with new constitutive model for COMP_4 test with experimental measurements.

In figure 6.7, the force-displacement diagrams over all load cycles as registered in the experiment and as calculated by DIANA with the new constitutive model are plotted. The initial stiffness, unloading stiffness, and energy dissipation show excellent agreement. The ultimate loading capacity is slightly higher than the experiment but still a good estimation. A small drawback is that the unloading stiffness for the first few loops is slightly overestimated. Another drawback is that the slight softening of the final loop observed during the experiment, cannot be seen in the analysis. Overall, this constitutive model and the input parameters simulate the experiment very well.

Also, in terms of the force-displacement curve, the degradation within each cycle is similar to the experiment. It means that loading the wall three times in both directions in each cycle is similar to loading the wall just one time in each cycle. Note that a single cycle is defined as three times the same applied load or deformation in both directions. In terms of crack patterns of the numerical result, loading the wall three times in each cycle can generate slightly more cracks with slightly larger crack width than just loading it once, which is consistent with mechanical understanding. However, this cannot be validated against the experiment because there is not experiment loaded just one time in each cycle.

Table 6.3: Summary of results for test COMP_4 in comparison to the experiment

	New Constitutive Model
Initial stiffness	Good agreement
Stiffness at the end of the analysis	Good agreement
Loading capacity	Good agreement
Energy dissipation	Good agreement
Crack pattern	Good agreement
Degradation within each cycle	Good agreement
Failure mechanism	Good agreement

6.2. Flexural failure (Double fixed test COMP_3)

COMP_3 is a quasi-static in-plane cyclic test performed at the TU Delft [12]. The specimen is $1.1m$ wide, $2.76m$ high, and $102mm$ thick. An overburden stress of $0.4MPa$ is applied. The wall was tested under double clamped boundary conditions.

For the model of the test COMP_3 (figure 6.8), the bottom edge is tied to the bottom left node with translations restricted in all directions. The nodes along the top edge are tied to the top left corner in both directions to ensure identical horizontal and vertical translation. In the first five steps, the vertical concentrated load (blue arrow) is applied at the top left corner and will be properly distributed to all the nodes of the top edge due to the requirement for equal displacements. The deadweight of the wall is also applied in these five steps. After the first five steps, a series of horizontal prescribed displacements (green arrow) is applied to achieve cyclic loading with increasing cycle amplitudes ranging from $1mm$ to $35mm$.

The green lines and the yellow lines represent the zero-thickness interface elements for the head joints and the bed joints, respectively. The new constitutive model is used for these interface elements with the 13 parameters listed in table 6.2. The grey plane stress elements are assigned with the linear elastic parameters in table 6.1.

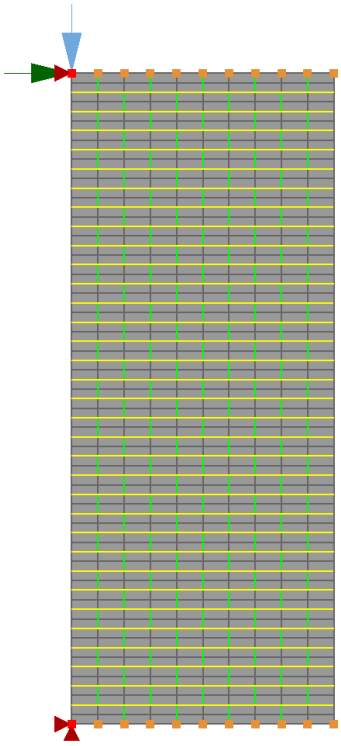

Figure 6.8: Finite element mesh with supports, loading for COMP_3 test

Figure 6.9a depicts the crack pattern of the experiment at the end of the testing protocol, whereas 6.9b depicts the crack pattern and deformed shape for the maximum lateral displacement at the top edge, and 6.9c the crack pattern when the wall is fully unloaded at the end of the analysis. In the experiment small diagonal staircase cracks in various directions and close to the four corners can be noticed. The deformed mesh of the numerical analysis also shows large tensile cracks along the top and bottom bed joints, with smaller cracks in the head joints close to the corners. This is similar to what was observed in the experiment. The current maximum value of the relative displacement of the interface elements can be regarded as the crack size because it is much greater than the relative displacement corresponding to the tensile strength of the tensile constitutive curve.

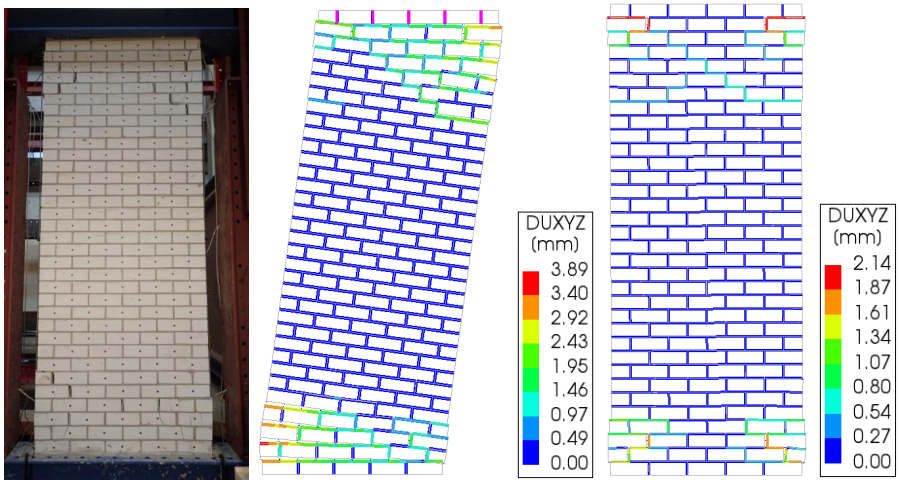

Figure 6.9: Observed crack pattern in the experiment of test COMP_3 and the absolute value of relative displacement of the interface when it is loaded with 35mm lateral displacement and unloaded for COMP_3 (in deformed mesh with scaling factor=10)

To be specific, in the analysis, the relative displacements of the interface in both shear and normal directions of the bed and head joints are illustrated in figure 6.10 and 6.11 respectively. Figures are captured when the wall reaches the maximum lateral displacement at the top ($35mm$). From the relative normal displacement of the bed joints, we can observe major tensile cracks along the top three and bottom three bed joint layers (maximum $3.89mm$). The tensile cracks of the bed joints are smaller than the experiment because the cracks are dispersed over the 3 top and bottom layers, which can be added up to more than $10mm$. Also, a small amount of crushing can be observed at the four corners. The relative normal displacement of the head joints also illustrates some smaller diagonal tensile crack along the head joints around the corners (maximum $2.19mm$). The diagonal cracks of the head joints at the top left corner and bottom right corner are larger than that at the top right and bottom left corner, because this figure is shown when the structure is loaded to the right ($35mm$). When the structure is unloaded at the end of the analysis, the crack size of the head joints in all four corners are similar to each other. The relative shear displacement of the bed joints is relatively smaller, compared with the relative shear displacement of the head joints. All these characteristics mentioned above determine that it is mainly dominated by flexural failure (rocking behaviour) with little sliding and crushing.

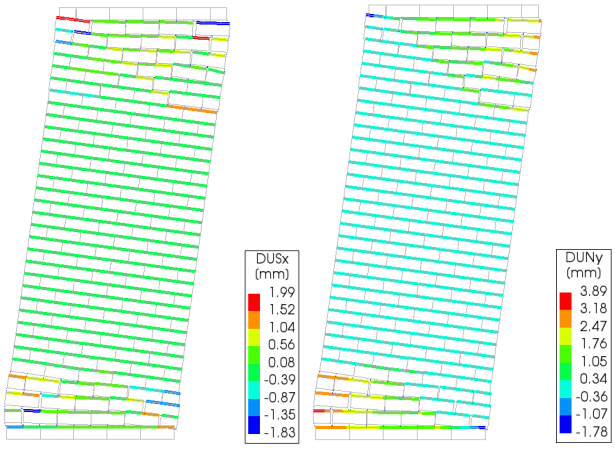

Figure 6.10: Shear (left) and normal (right) relative displacement of bed joints under largest shear deformation in deformed mesh for test COMP_3 (scaling factor=10)

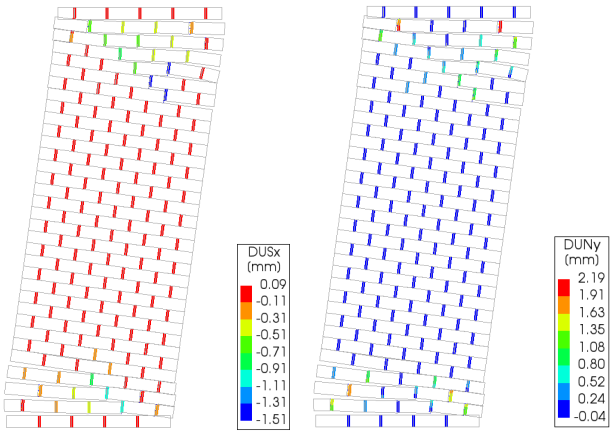

Figure 6.11: Shear (left) and normal (right) relative displacement of head joints under largest shear deformation in deformed mesh for test COMP_3 (scaling factor=10)

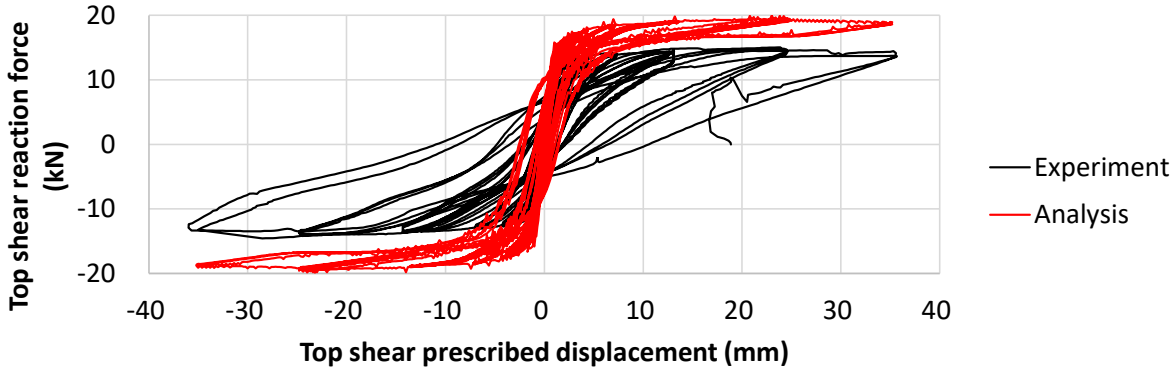

Figure 6.12: Force displacement diagram from DIANA simulation with new constitutive model for COMP_3 test with experimental measurements.

In figure 6.12, the force-displacement diagrams over all load cycles as registered in the experiment and as calculated by DIANA with the new constitutive model are plotted. The initial stiffness shows good agreement. However, the ultimate loading capacity is 25% higher than the experiment, and the energy dissipation and unloading stiffness are severely underestimated.

Also, in terms of the force-displacement curve, the degradation within each cycle is similar to the experiment. It means that loading the wall three times in both directions in each cycle is similar to loading the wall just one time in each cycle. Note that a single cycle is defined as three times the same applied load or deformation in both directions. In terms of crack patterns of the numerical result, loading the wall three times in each cycle can generate slightly more cracks with slightly larger crack width than just loading it once, which is consistent with mechanical understanding. However, this cannot be validated against the experiment because there is not experiment loaded just one time in each cycle.

In the following, some input parameters will be calibrated, and the reasons will be explained.

Looking back to the force-displacement curve, we could see that especially for the cycle with large lateral displacement, the structure is unloaded with shear force barely reduce. This is a very typical rocking behaviour with little toe crushing. Furthermore, because of the lack of toe crushing, the contact area for compression along the bottom mortar layer is very small (within half of the corner brick) while the rest of the layer is opened, as shown in the right plot of figure 6.10. The contact area is so small that it makes the level arm for vertical compression force almost equal to the length of the wall. Therefore

for the equilibrium of moment, the peak shear force can be calculated analytically:

$$F_s \times (h_{wall} - 2h_{FEM,u}) = q l_{wall} t_{wall} \times r_c \tag{6.1}$$

where

F_s: shear lateral force
h_{wall}: height of the wall $2760mm$
l_{wall}: length of the wall $1100mm$
t_{wall}: thickness of the wall $102mm$
$h_{FEM,u}$: height of the brick in the FE model $2760/34 = 81.176mm$
q: precompression pressure $0.4MPa$
r_c: level arm of the vertical compressive load $r_c = l_{wall} = 1100mm$

Solving the equation returns $F_s = 19kN$ which is very close to the peak of the force-displacement curve from the analysis. The lack of toe crushing in the numerical analysis also keeps the contact area (or the rotating center of the rocking) very small and close to the corner, until the wall is almost fully unloaded. Therefore the level arm r_c of the shear force barely reduces during the unloading, and almost the same amount of shear force is needed to keep the moment equilibrium mentioned above. This abovementioned behaviour is not the case for the experiment: The contact area could be much larger due to the crushing of the mortar layer or the splitting of the bricks, as shown in the report of the experiment[12]. Because in this analysis, we assume a fully elastic behaviour of the brick, therefore the plastic deformation at the corner might be underestimated.

To compensate for this disadvantage, the compressive strength of the bed joint can be reduced to a relatively low value ($2MPa$). The compressive fracture energy $G_{f,c}$ is also reduced to $12.85N/mm$ to keep the area under the softening branch of the modified Engineering Masonry compressive curve unchanged. Then the analysis is rerun, and the results are shown below.

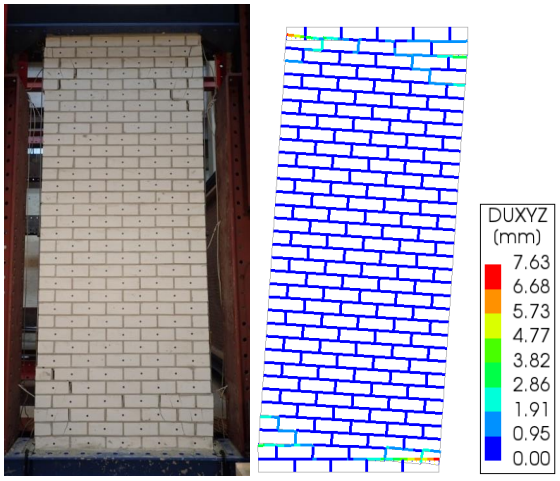

Figure 6.13: Observed crack pattern in experiment of test COMP_3 and the absolute value of relative displacement (calibrated) of the interface when it is loaded with 35mm lateral displacement and unloaded for COMP_3 (in deformed mesh with scaling factor=5)

Compared with the absolute value of the relative displacement of the interface from the un-calibrated model (figure 6.9), figure 6.13 above shows more deformation at the toe. This can also be verified by the relative normal displacement of the bed joint (figure 6.14), which has a maximum compressive relative displacement of $7.61mm$. The value is reasonable, and it is smaller than the actual thickness of the mortar layer ($10mm$) in the experiment. The width of the tensile crack on the other end of the bed joint is similar to the un-calibrated model with a maximum value of $3.69mm$. From the relative shear and normal displacement of the head joints (figure 6.25), the deformed mesh also shows some cracks,

which is consistent with the experiment. Overall, the failure mode of mimics the experimental result, which is a flexural failure with some toe crushing.

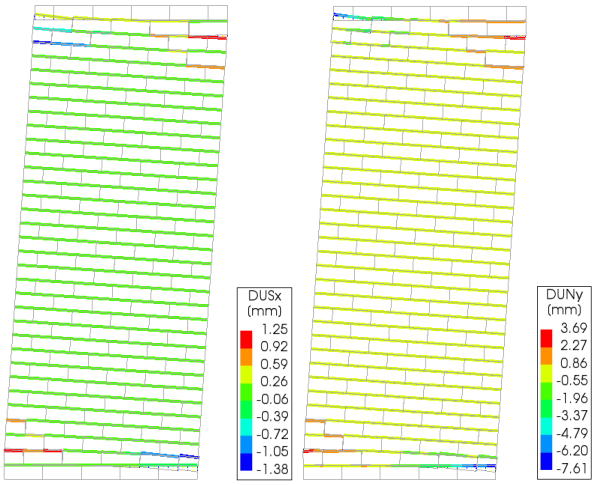

Figure 6.14: Shear (left) and normal (right) relative displacement of bed joints under largest shear deformation in calibrated deformed mesh for test COMP_3 (scaling factor=5)

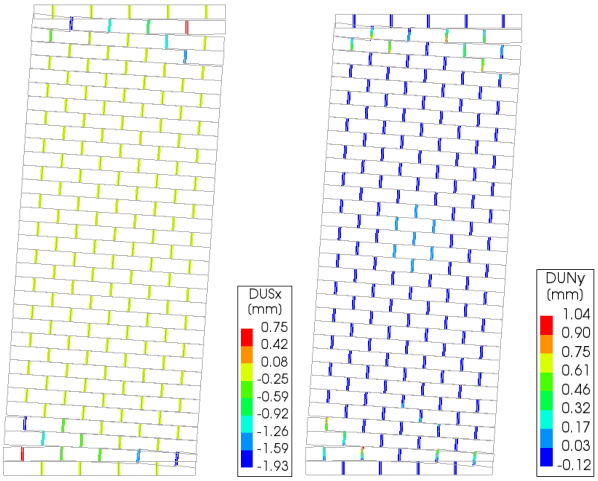

Figure 6.15: Shear (left) and normal (right) relative displacement of head joints under largest shear deformation in calibrated deformed mesh for test COMP_3 (scaling factor=5)

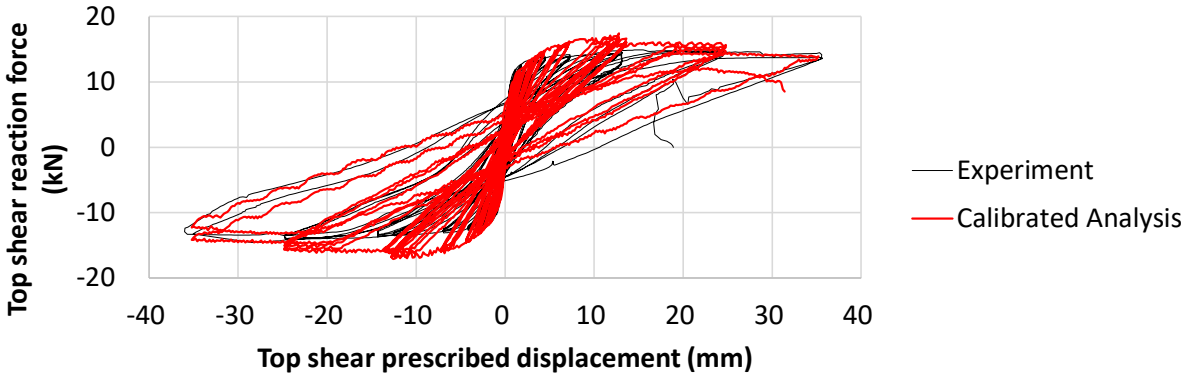

Figure 6.16: Force displacement diagram from calibrated DIANA simulation with new constitutive model for COMP_3 test with experimental measurements.

The force-displacement curve of the calibrated analysis is shown in figure 6.16. The curve shows a very good agreement in initial stiffness, unloading stiffness at the end of the loading, and energy dissipation with the experiment. The ultimate shear capacity is slightly higher than the experiment but still good. The shear capacity of the wall gradually reduces over the cycles, reaching during the last cycle ($35mm$) the shear force found in the experiment. Also, notice that the last two times of the unloading process in the negative direction show some fluctuation, which can be smoothened with the refinement of the mesh of the bed joints. Besides, the degradation within each cycle for loading multiple times is very close to the experiment, especially within the final cycle. Decomposing this force-displacement diagram shows very similar unloading and reloading behaviour for each cycle, which leads to the conclusion that this calibrated analysis shows good consistency in comparison with the experiment.

Table 6.4: Summary of results for test COMP_3 in comparison to the experiment

	New Constitutive Model	Calibrated New Constitutive Model
Initial stiffness	Good agreement	Good agreement
Stiffness at the end of the analysis	Poor agreement	Good agreement
Loading capacity	Reasonable agreement	Good agreement
Energy dissipation	Poor agreement	Good agreement
Crack pattern	Good agreement	Good agreement
Degradation within each cycle	Good agreement	Good agreement
Failure mechanism	Good agreement	Good agreement

6.3. Combined shear and flexural failure (Cantilever test COMP_6)

COMP_6 is a quasi-static in-plane cyclic test performed at the TU Delft [12]. The specimen is $4.0m$ wide, $2.76m$ high, and $102mm$ thick. The overburden stress of $0.5MPa$ is applied. The wall was tested under cantilever boundary conditions.

For the model of the test COMP_6 (figure 6.17), the bottom edge is tied to the bottom left node with translations restricted in all directions. The nodes along the top edge are tied to the top left corner in the horizontal directions to ensure identical horizontal translation. A rigid beam shown in magenta is attached to the top edge to achieve the cantilever boundary condition. In the first five steps, the vertical distributed load (blue arrow) is applied along the top edge. The deadweight of the wall is also applied in these five steps. After the first five steps, a series of horizontal prescribed displacements (green arrow) is applied to achieve cyclic loading with increasing cycle amplitudes ranging from $0.25mm$ to $15.6mm$.

The green lines and the yellow lines represent the zero-thickness interface elements for the head joints and the bed joints, respectively. The new constitutive model is used for these interface elements with the 13 parameters listed in table 6.2. The grey plane stress elements are assigned with the linear elastic parameters in table 6.1.

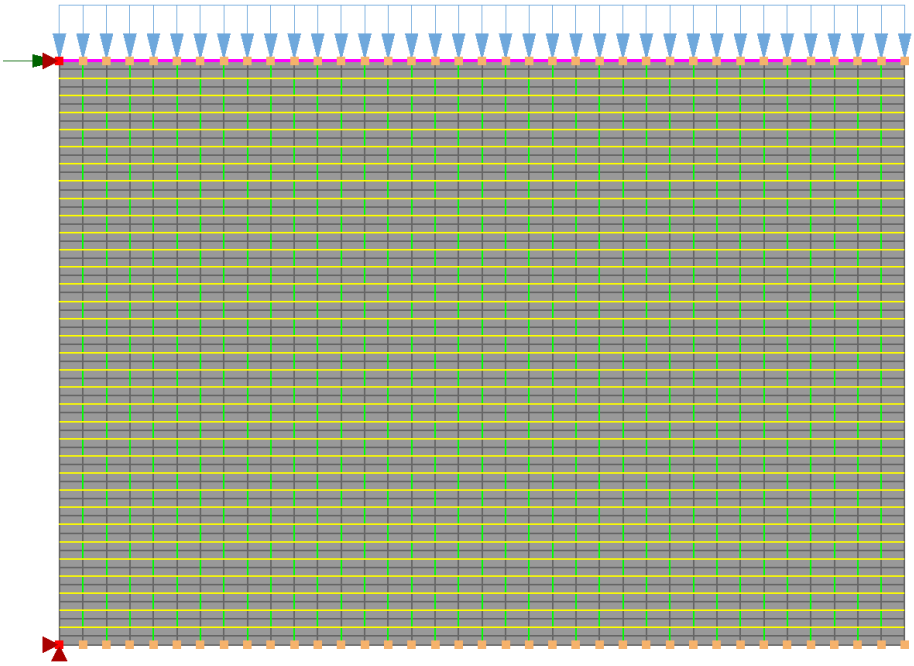

Figure 6.17: Finite element mesh with supports, loading for COMP_6 test

Figure 6.18 shows the crack pattern of the experiment, and figure 6.19 depicts the crack pattern and deformed shape for the maximum lateral displacement at the top edge ($15.6mm$) and when it is fully unloaded at the end of the analysis. The picture of the experiment shows several staircase cracks running from the top left corner directly to the bottom right corner, and also from the left side of the top edge to the bottom left corner. Also there are bricks crushing at corners, and the corners also drift to the steel columns on both sizes, which results in less support to the wall. The mesh of the analysis also shows large diagonal staircase cracks from the top corners to the bottom corners. However, the cross of the diagonal cracks locates at the lower center of the wall, while in the case of the experiment, it locates at the left upper center of the wall. Besides, there are some smaller diagonal cracks close to the bottom corner in the analysis, similar to the experiment. Although the crack pattern is reasonable, the movement of the wall indicates that the wall is dominated by a shear failure (sliding) behaviour, which is not very consistent with the experiment. In the experiment, the splitting of the bricks at the

corners and upper left center of the wall is prominant, which significantly reduces the capacity of the wall. This is clearly not the behaviour of shear sliding.

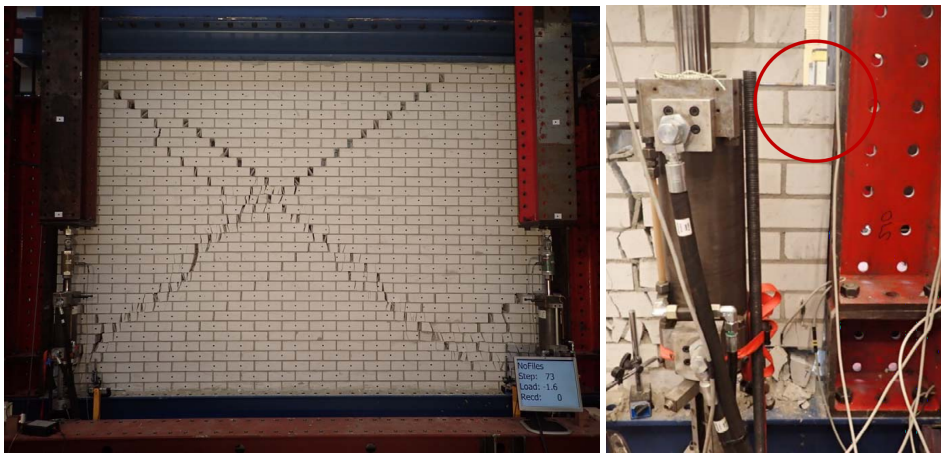

Figure 6.18: Observed crack pattern in the experiment of test COMP_6

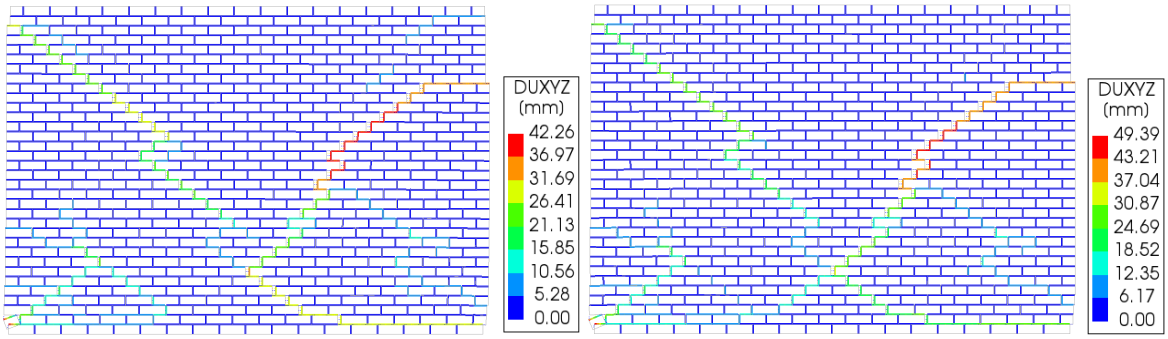

Figure 6.19: The absolute value of relative displacement of the interface when it is loaded with 35mm lateral displacement and unloaded for COMP_6 (in deformed mesh with scaling factor=1)

To be specific, in the analysis, the relative displacements of the interface in both shear and normal directions of the bed and head joints are illustrated in figure 6.20 and 6.21 respectively. Figures are captured when the wall reaches its maximum lateral displacement at the top $(15.6mm)$. From the relative shear displacement of the bed joints and the relative normal displacement of the head joints, we can observe that the wall is cracked into several big triangle pieces that are sliding with each other, which generates a maximum $41mm$ head joints crack. The relative normal displacement of the bed joints and the relative shear displacement of the head joints is relatively minor which means crushing and flexural failure at the bottom corners barely occurs, while crushing of the bottom corners did occur at the later stage of the experiment although the diagonal staircase crack occurred first from the top left corner. In the experiment, the wall shifts from combined flexural and shear behaviour to a dominating flexural behaviour when the lateral displacement increased. The analysis is only accurate at the early stage when the flexural and shear behaviours both contribute to the deformation, and it deviates to shear sliding instead of flexural behaviour subsequently.

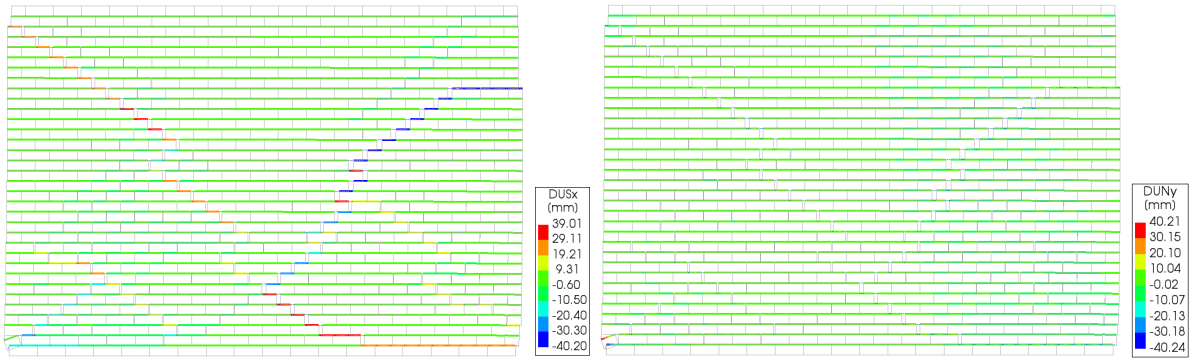

Figure 6.20: Shear (left) and normal (right) relative displacement of bed joints under largest shear deformation in deformed mesh for test COMP_6 (scaling factor=1)

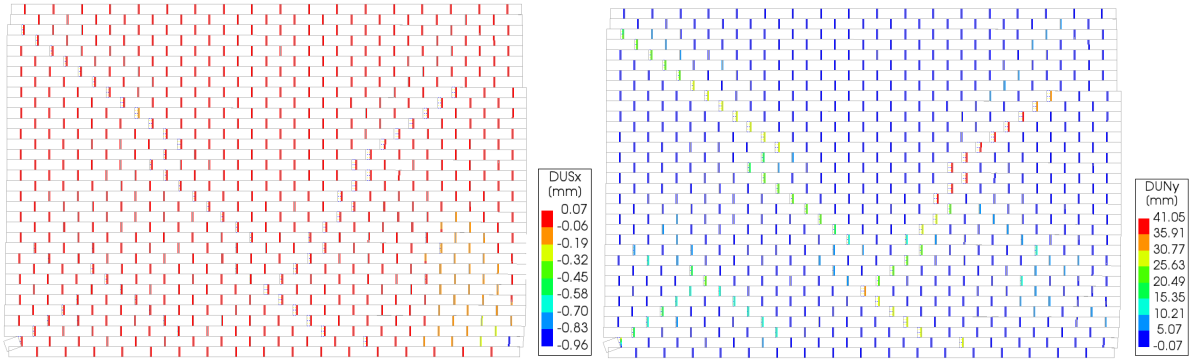

Figure 6.21: Shear (left) and normal (right) relative displacement of head joints under largest shear deformation in deformed mesh for test COMP_6 (scaling factor=1)

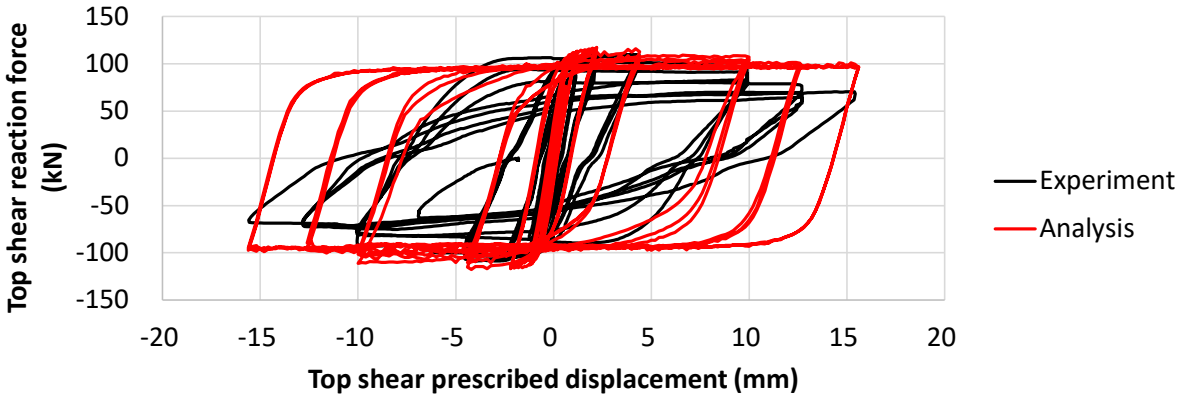

Figure 6.22: Force displacement diagram from DIANA simulation with new constitutive model for COMP_6 test with experimental measurements.

In figure 6.22, the force-displacement diagrams over all load cycles as registered in the experiment and as calculated by DIANA with the new constitutive model are plotted. The initial stiffness and loading capacity show good agreement. However, the energy dissipation and unloading stiffness are severely overestimated. Also, it should be noted that for the cycle with an amplitude equal to $10mm$, the analysis shows an expansion of dissipated area when loaded the wall three times, while the experiment shows shrinkage of the area on the contrary. This is due to the fact that for the analysis, as the head-joint crack develops dramatically, the flexural restoration is taking less proportion of the unloading process,

whereas the shear sliding is increasing[1] . For the experiment, the flexural restoration is more dominant as the crushing of the corner worsens, while the shear sliding is limited as the diagonal staircase cracks only widen slowly. Because shear sliding following the initial shear stiffness that is much higher than the flexural restoration, tilting to one of them increases or decreases the unloading stiffness respectively. Also, having a constant peak capacity for each cycle in the analysis is also a typical characteristic of the domination of shear sliding. In contrast, decreasing peak capacity is the result of flexural damage. Therefore the force-displacement curve also confirms that the analysis is only correct at the beginning of the analysis and deviates afterwards due to the wrong failure mechanism.

In the following, some input parameters will be calibrated, and the reasons will be explained.

From the discussion above, we noticed that the failure of the wall in the FE analysis is dominated by shear sliding, so does the force-displacement curve reveal. The analysis shows little toe crushing or flexural failure behaviour. To enable toe crushing, similar to COMP_3, the compressive strength f_c of the head joints can be reduced. Additionally, to reduce the shear sliding, the friction angle phi can be slightly increased to increase the resistance in shear, such that the structure is relatively weaker in flexure. To be specific, f_c is reduced to $4.5MPa$ from $5.98MPa$ and ϕ is increased to $26.57\circ$ from $23.27\circ$. The result of the calibrated FE analysis is shown below. Note that only reducing f_c to a lower value such as $3MPa$ or $2MPa$ will yield a similar result in terms of the force-displacement curve and crack pattern, except that more toe crushing will take place.

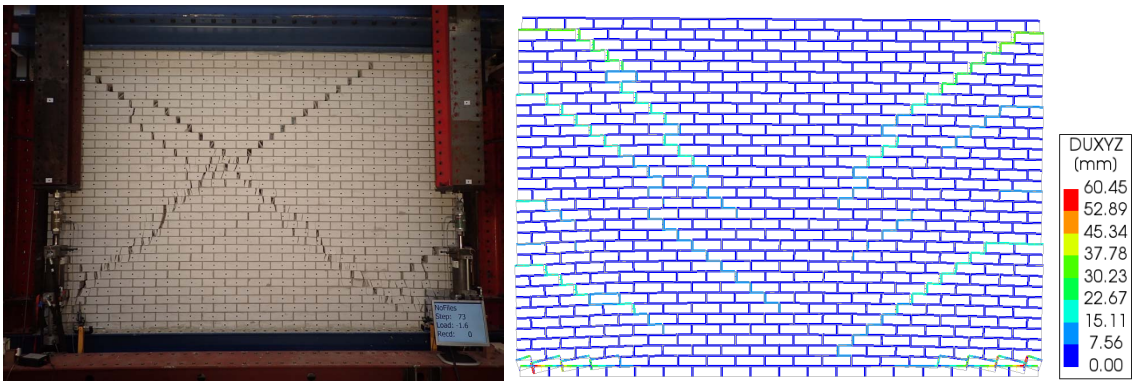

Figure 6.23: Observed crack pattern in experiment of test COMP_6 and the absolute value of relative displacement (calibrated) of the interface when it is loaded with 35mm lateral displacement for test COMP_6

Compared to the relative normal displacement of the bed joints of the un-calibrated analysis (figure 6.20), the calibrated result shows significant toe crushing at the bottom mortar layer (figure 6.24) with the maximum compressive relative displacement of $60mm$. Also, the maximum relative shear displacement drops from the previous $39mm$ to $30mm$. More staircase cracks generate at the upper part of the wall than in the original analysis which is more concentrated at the lower wall, as shown in the relative shear displacement of the bed joints (figure 6.24) and relative normal displacement of the head joints (figure 6.25). However, the left shifted crack pattern is still not the case for the analysis which is more symmetric. Although the crack pattern is still not the same as the experiment, as no significant cross of stair crack can be seen, it still shows a combination of shear crack and toe crushing behaviour that is similar to the experiment. Overall speaking, it is better than the un-calibrated model.

[1]The flexural restoration means that during the unloading process, the structure is restoring to its undeformed shape in the way similar to a flexural beam. In contrast, the structure can also restore to the undeformed shape by sliding back to its original position. The combination of them comprises the unloading behaviour. Usually, the flexural restoration is characterized by a more gradual reduction of top lateral reaction force, while the sliding back will suddenly reduce a huge amount of lateral reaction force since shear unloading follows initial stiffness.

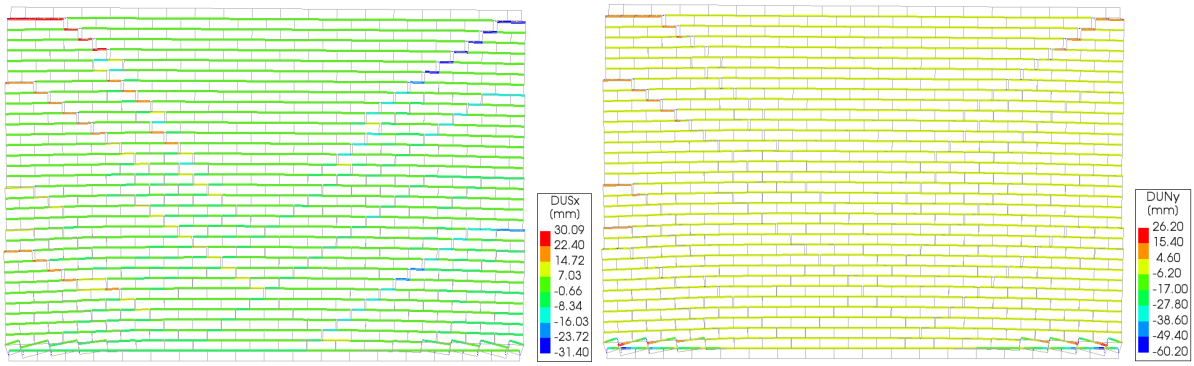

Figure 6.24: Shear (left) and normal (right) relative displacement of bed joints under largest shear deformation in calibrated deformed mesh for test COMP_6 (scaling factor=1)

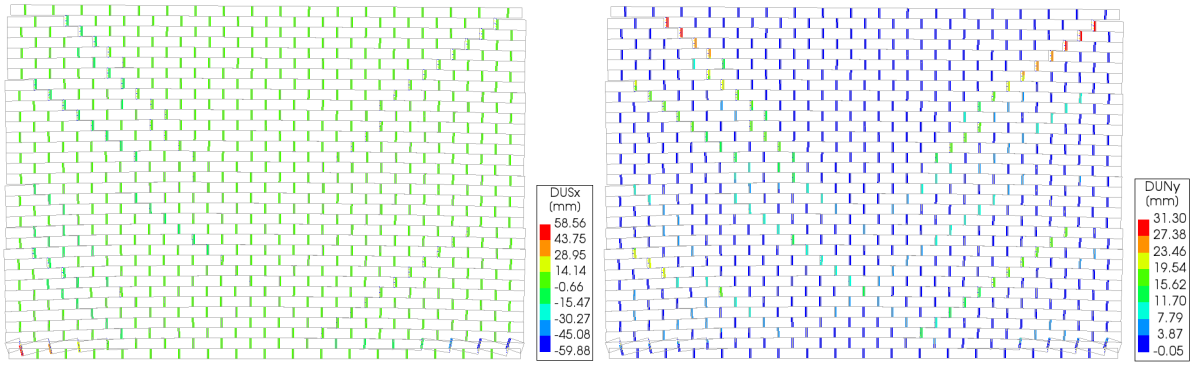

Figure 6.25: Shear (left) and normal (right) relative displacement of head joints under largest shear deformation in calibrated deformed mesh for test COMP_6 (scaling factor=1)

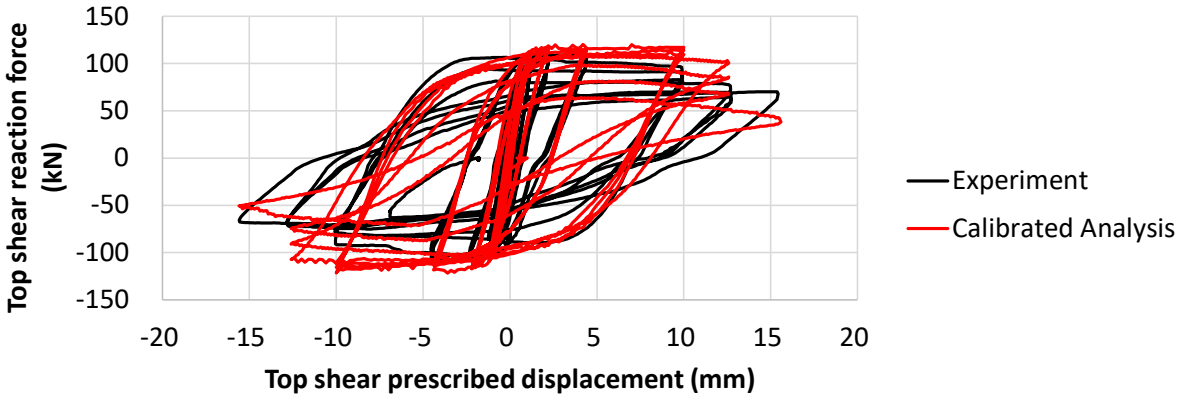

Figure 6.26: Force displacement diagram from calibrated DIANA simulation with new constitutive model for COMP_6 test with experimental measurements.

The force-displacement curve of the calibrated model is depicted in figure 6.26 and compared versus the experimental results. The analysis shows a good agreement in initial stiffness, ultimate capacity, unloading stiffness at the end of the loading procedure, and energy dissipation with the experiment. The difference mainly lies in the degradation of each cycle for loading multiple times. In the experiment, dramatic degradation due to the unloading and reloading three times occurs at the cycle with the amplitude equal to $10mm$, which leads to the dramatic reduction of peak capacity in the next cycle. This is due to the dramatic toe crushing at the corner in the experiment. In the analysis, the dramatic reduction happens one cycle later, which is the one with the amplitude about $12.5mm$. However, their

behaviours of degradation are similar. When degradation within a cycle occurs, there are both reduction of the shear capacity and shrinkage of the area of the loop. Besides, they are both due to the toe crushing, although the toe crushing in the experiment is more of the splitting of the bricks, whereas, in the numerical analysis, it can only happen as crushing of bed joints. Therefore, we can still conclude that the force-displacement curve of the analysis mimics the experimental result in a decent way. More generally, both the experiment and the calibrated analysis show the shift from a combined shear and flexural behaviour at the early stage of loading to a flexural dominating failure behaviour at the end.

Table 6.5: Summary of results for test COMP_6 in comparison to the experiment

	New Constitutive Model	Calibrated New Constitutive Model
Initial stiffness	Good agreement	Good agreement
Stiffness at the end of the analysis	Poor agreement	Good agreement
Loading capacity	Good agreement	Good agreement
Energy dissipation	Poor agreement	Good agreement
Crack pattern	Reasonable agreement	Reasonable agreement
Degradation within each cycle	Poor agreement	Good agreement
Failure mechanism	Poor agreement	Good agreement

6.4. Summary

In this chapter, the quantitative verification on the structural wall level is performed. A real example of obtaining values for input parameters from material tests is discussed in detail. These input parameters are adopted for modelling three masonry walls with different governing failure mechanisms, namely shear failure, flexural failure and combined shear and flexural failure. The FE analyses are run, and the outcomes are compared with the experiments conducted on the same walls. The proposed constitutive model shows to be particularly good at modelling pure shear failure (COMP_4). However, for the models involving flexural behaviour such as COMP_3 and COMP_6, it usually underestimates the toe crushing, which results in a deviation between the numerical and experimental results. This might be due to the fact that the compressive plastic deformation or even failure of the brick is not able to be completely captured in the current model, although we tried to lump all the plastic deformation of the masonry including the brick to the interface. There might be some form of plastic deformation of the brick, such as splitting, that is impossible to considered equivalently with interface element. However, the non-linearity of the brick cannot be simply added into the current model because most of the input parameters, as well as some of the algorithms of the constitutive model itself, are derived under the assumption of perfectly elastic bricks. If the non-linearity of the brick is considered in the FE model, then the parameters of the interface element must also change, and some of the algorithms should also alter consequently. This is far beyond the scope of this thesis. Also, this will dramatically increase the computational cost and might not be worthy. During the calibration of the parameter, it is found that the nonlinear compressive behaviour of the interface element is particularly important, which will also be shown in the brief introduction of parameter study in the next chapter. Maybe, it will be possible to find a uni-axial compressive curve for bed-joint interface elements that could equivalently simulate the splitting behaviour such that the brick can still be perfectly elastic. Because of the limitation in time, the easiest solution to have a more realistic simulation on flexural failure is to reduce the compressive strength f_c of the bed joints, as discussed before. This could be an applicable way for structures under relatively low precompression. If it is applicable for structures under high precompression remains unknown. Also, there are no clear guidelines provided in this thesis about the extent the compressive strength should reduce. This is due to the limited number of models available for calibration and also the lack of theoretical study.

Additionally, note that the dependency of the step size of the analysis is briefly studied during the analyses of the wall models. The results of the analyses turn out to be barely dependent on the step size as long as it can converge. The bigger step size can only reduce the resolution of the force-

displacement curve and increase the amount of fluctuation but will not influence the overall trend. This is consistent with one of the purposes of the implementation of the sub-increment that the result should be step-size independent, as discussed in section 3.5.

Also, no divergence problems were encountered during any of the FE analyses, except if the structure really fails. The FE analysis is much more robust with Quasi-Newton-Raphson (secant) scheme than with the Full-Newton-Raphson (tangential) scheme, but this has nothing to do with the proposed constitutive model. In the proposed constitutive model, the tangential stiffness of the uni-axial constitutive curves are returned, and whether the FE program would like to use it for iteration depends on the user setting in the program. In all the analyses, Quasi-Newton-Raphson (secant) scheme is used in DIANA to avoid negative terms in the global stiffness matrix.

In a nutshell, this chapter shows that the proposed constitutive model is a robust method that does not have numerical difficulties at the corner at the yield surface, by eliminating the conventional mapping back process. The model is accurate for shear failure and less accurate for flexural failure. If the input parameters are slightly calibrated, the model can also replicate the flexural crack pattern and force-displacement curve very well.

7

Brief introduction to parameter study

In this section, the influence of the change of some important parameters on the behaviour of the wall is discussed. The parameter study is based on the FE model built in the previous section. The study reflects the sensitivity of the constitutive model to the change of parameters and provides a guideline on how precise some of the parameters should be to obtain a reasonable result.

For obtaining the conclusions below, a high number of analyses were run to see the effect of altering parameters. Due to the limitation of the space and time, only some of the results of the analyses will be posted, but the conclusion for each parameter will be described in detail.

7.1. Number of loading and unloading in a cycle

The influence of the number of loading and unloading in each cycle on the overall behaviour is crucial because it determines whether it is necessary to run the same cycle several times in the analysis.

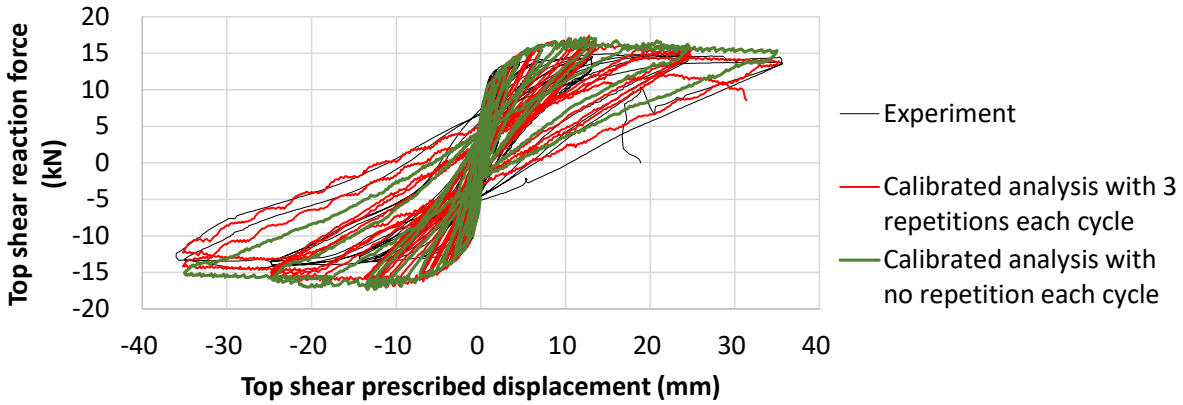

Figure 7.1: Analysis results of the models of COMP_3 loaded with 3 repetitions in each cycle (initial value) and with no repetition in each cycle (modified value)

For structures that dominated by rocking failure, such as the double clamped short wall COMP_3 (figure 7.1), one time of loading and unloading in positive and negative directions can already generate a force-displacement curve that is similar to the analysis with multiple repetitions in each cycle. In these cases, an increase in the number of repetitions per cycle, with the same amplitude of displacement, can lead

to wider cracks but will not change the overall behaviour or capacity. Therefore, it is sufficient for each cycle to have a single repetition, in positive and negative directions, to reduce computation time dramatically.

If the structures dominated by shear sliding, one should be careful about whether the loss of cohesion will significant influence the result or not, because the loss of cohesion is strongly related to the total absolute relative displacement, or the number of repetitions in each cycle. If the lost of cohesion is very slow (because the shear fracture energy is relatively large) and the amplitude of each cycle is relative small, then the lost of cohesion can be neglected, such as the wall COMP_4. In this case, one time of loading and unloading in positive and negative directions can also already generate a force-displacement curve that is similar to the analysis with multiple repetitions in each cycle. If the cohesion barely contribute to the sliding resistance, then repetitions in each cycle is also not needed. However, if cohesion contribute a significant amount of resistance, loading with several repetitions in each cycle could be important. For example, if the friction angle ϕ of the wall COMP_4 is reduced to lower value to increase the proportion of contribution of cohesion to the shear resistance, there will be significant reduction of shear capacity due to cohesion loss, if the wall is loaded more times in each cycle. In this case, repetitions in each cycle must be modelled in the FEA.

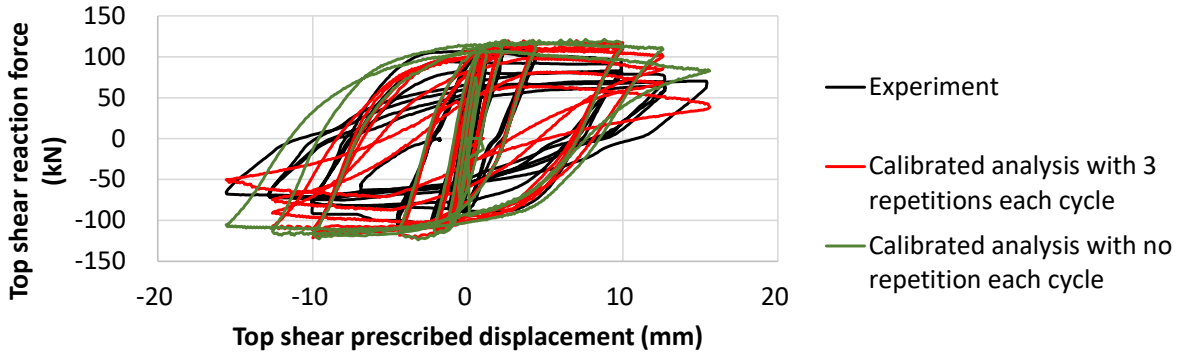

Figure 7.2: Analysis result of the models of COMP_6 loaded with 3 repetitions in each cycle (initial value) and with no repetition in each cycle (modified value)

For structures that combine both shear and flexural behaviours, such as the cantilever long wall COMP_6 (figure 7.2), it could be crucial to have repetitions per cycle as in the experiment. Usually, this kind of structure will show combined shear and flexural behaviour at the early stage of the loading procedure. As the number of cycles increases, or as the number of repetitions within each cycle increases, the structure will start to degrade dramatically with the shear or flexural behaviour dominated. The timing of the transition of behaviour depends heavily on the number of repetitions in each cycle. The more repetitions it is loaded, the faster it will shift to shear failure (sliding) or flexural failure (toe crushing). For the one that fails with toe crushing, multiple loading and unloading can lead to a fast reduction in peak capacity, even if the amplitude of the cycle remains unchanged. Therefore, the structure needs to be loaded multiple times in each cycle. Otherwise, the capacity of the structure at the end of the analysis can be overestimated.

7.2. Unloading and reloading parameter of compression λ

The unloading and reloading parameter λ is used to defined the proportion of the unloading with initial stiffness to the entire unloading process, as described in section 3.3.2. If $\lambda = 1$, then the structure is unloaded with initial stiffness, and if $\lambda = 0$, the structure is unloaded with secant stiffness. The intermediate value of λ between 1 and 0 corresponds to the combination of these two unloading methods. Reloading follows the same path as unloading.

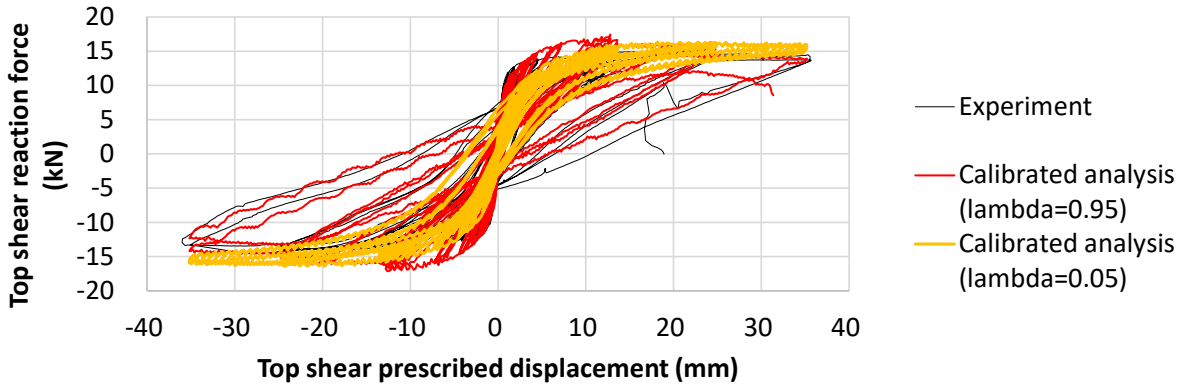

Figure 7.3: Analysis result of the models of COMP_3 with $\lambda = 0.95$ (initial value) and $\lambda = 0.05$ (modified value)

The value of λ is less important for sliding behaviour as in the COMP_4 because the compressive stress in the bed joints is relatively stable and does not directly influence the unloading and reloading behaviour of the analysis. However, it is essential for flexural behaviour. The compressive experiments have shown that the masonry tends to be unloaded with initial stiffness, meaning that λ should be closer to 1. If the secant unloading is used in the analysis, for instance, in COMP_3 (figure 7.3), the energy dissipation will still be severely underestimated even with compressive strength smaller than $2MPa$. Note that in the original compressive curve from the Engineering Masonry Model, at reloading a straight line to the last loading extreme point (or the elastic limit point ($d_{c,limit}, \sigma_{c,limit}$)) is followed, while in this constitutive model, the reloading follows the same path as unloading, which is similar to the experiment. The reason for the original constitutive model to adopt that reloading behaviour might be to have a better energy dissipation during unloading and reloading. The study in this thesis indicates that if using the original reloading method for interface elements, energy dissipation can be overestimated.

In conclusion, for the simulation of masonry structure, a value of λ that is closer to 1 is recommended. For the simulation of other materials, the value of λ should be carefully selected to ensure a correct energy dissipation for flexural failure.

7.3. Precompression

The increase of precompression has a similar effect as the decrease of compressive strength f_c of the bed joints. The higher the precompression, the better energy dissipation will be. Also, if the compressive strength of the bed joints is high enough to allow rocking behaviour without significant toe crushing, the peak capacity of the force-displacement curve will increase as the precompression force increases. For sliding behaviour, the higher the precompression, the slower the wide concentrated staircase crack will occur. If the analysis shows relatively small dispersed head joint cracks in the diagonal directions, such as the COMP_4, it does not mean that the concentrated crack will not occur. Keep loading the wall with greater lateral displacement will eventually result in wide concentrated staircase cracks. In reality, the concentrated staircase crack usually occurs earlier than the analysis, and this might be due to the imperfection of the joints.

7.4. Compressive curve and relative displacement of compressive strength $d_{c,peak}$

Both of the compressive curves are not perfect for the interface element in masonry simulation.

The advantage of the parabolic curve is that the shape of the curve before the peak has a more grad-

ual reduction of the slope than the modified Engineering Masonry Model compressive curve. However, the relative displacement $d_{c,peak}$, or in other word the $(d_{c,fc})$ of the peak strength f_c, is fixed to be $5f_c/(3K_{c,e})$, which is shown to be smaller than the typical values observed in the compressive experiments. Therefore the ductility of the hardening branch is relatively too small, and the reduction in secant stiffness is also too slow. This will result in an overestimation of the stiffness and capacity during the early stages of cyclic loading (orange line in figure 7.4). The initial elastic stiffness of compression $K_{c,e}$ can be reduced for compensation; however, it also reduces the unloading stiffness if initial stiffness is followed. This will, on the other hand, reduce the energy dissipation.

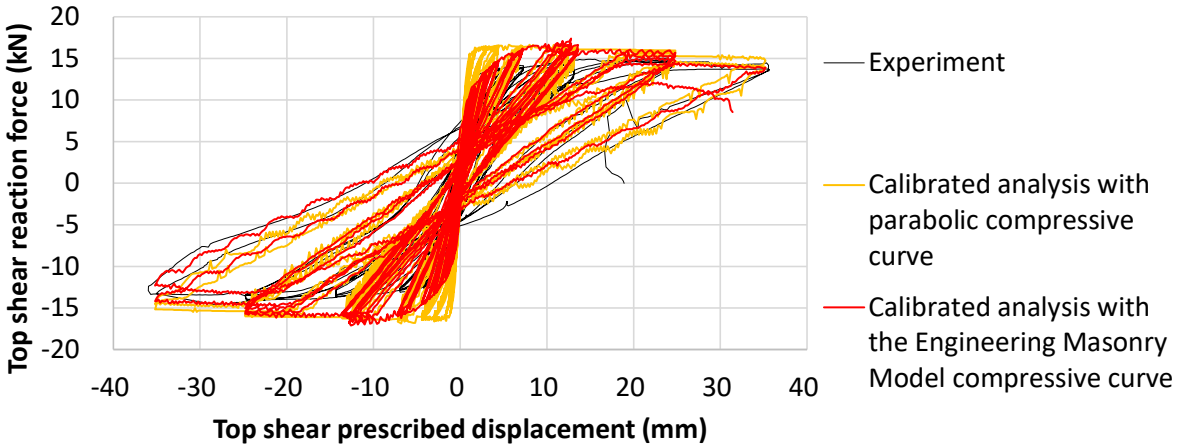

Figure 7.4: Analysis result of the models of COMP_3 with the Engineering Masonry Model compressive curve (initial) and parabolic compressive curve (modified)

The modified compressive curve from the Engineering Masonry Model is more flexible than the parabolic curve in letting the user define the value of the $d_{c,peak}$. However, when $d_{c,peak}$ is relatively large compared with $f_c/Kc,e$, then the transition of the slope is not that smooth. A kink might exist at the connection of the third-order part and the parabolic part, which results in a sudden reduction of the slope. For example for the compressive strength $f_c = 2MPa$ and $d_{c,peak} = 0.89mm$, the slope of a very short length of third-order curve close to the connection (locating at $d_c = f_c/Kc,e$) is even negative. This could result in an underestimate of the peak capacity and overestimate energy dissipation for the cycle with a tiny amplitude. However, the stiffness in these cycles is better simulated than the parabolic curve. Besides, the simulation is good for cycles with relatively large amplitudes. Therefore, in the verification on the wall level, this modified Engineering Masonry Model compressive curve is used.

A better version of the uni-axial compressive curve could be proposed in a future study to solve this problem.

7.5. Compressive strength f_c

As mentioned above, the compressive curve of the bed joint is critical to the overall behaviour for flexure, so is the compressive strength f_c. The compressive strength of the bed joint is the most sensitive factor that influences the peak capacity of a wall featuring flexural behaviour. Reducing compressive strength can significantly increase the amount of toe crushing and consequently reduce the peak capacity of the lateral force. Besides, it is the most crucial factor to be calibrated to get a correct force-displacement curve for short walls such as COMP_3. As we can see from the calibration, reducing compressive strength increases the energy dissipation significantly. Furthermore, if the wall is a combined shear and flexural behaviour, such as the COMP_3, reducing compressive strength means reducing flexural stiffness, and therefore, the structure will be more likely to fail in the flexural way.

For sliding behaviour, the compressive strength f_c of the bed joints is less critical. No significant change

in the force-displacement curve can be observed for decreasing it. Of course, the compressive strength f_c should not be too low; otherwise, the flexural failure might occur.

For head joints, the value of it is also not important either. Reducing the compressive strength of the head joint will not change the force-displacement curve because the lateral and vertical force applied at the top is transferred to the bottom by the compression and shear of the bed joints. The contribution of the head joint is negligible, even if the compressive strength of the head joints is higher than that of the bed joints.

7.6. Friction angle ϕ

The friction angle ϕ of the bed joints is a critical value for analysis featuring shear failure, flexural failure, and the combination of them.

For sliding behaviour, such as the COMP_4, the friction angle is the most sensitive factor that influences the peak capacity. Slightly reducing the friction angle phi will lower the peak capacity. Therefore, to accurately determine the peak capacity of a shear failure dominated structure, phi should be carefully derived from the test and calibrated.

Also, if the friction angle ϕ is reduced to a lower value (green lines in figure 7.5), it is also possible that the sliding along the stair-case cracks will change into sliding along the top edge. This is because the top edge is under lowest precompression (considering the dead weight of the bricks) and its frictional resistance is the lowest. Increasing the shear fracture energy slows down the loss of cohesion (orange lines in figure 7.5), which, in the other way, increases the shear resistance of the top edge. And the sliding will maintain to be along the stair-case cracks of the wall.

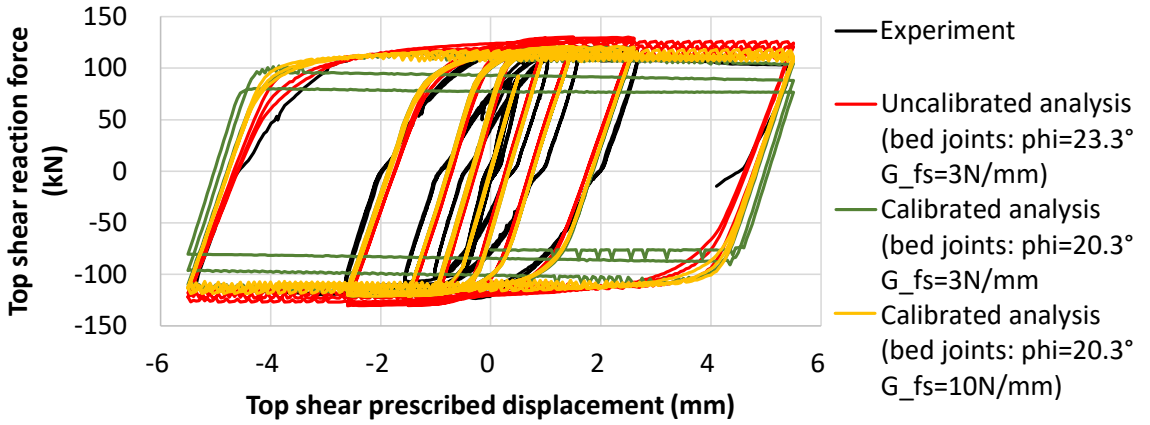

Figure 7.5: Numerical results of the un-calibrated model of COMP_4 (initial), the model of COMP_4 with bed joints of lower friction angle (modified), and the model of COMP_4 with bed joints of lower friction angle and higher shear fracture energy (modified)

For flexural behaviour, the analysis is less sensitive to the friction angle. However, it is still important because a too low friction angle will shift the flexural behaviour into a sliding behaviour. For example, if the short wall COMP_3 is analyzed with a very small frictional angle, it could fail with sliding instead of toe crushing. Therefore, although it is not that sensitive, the friction angle ϕ should still be in a reasonable range.

The friction angle of the head joints is not important as it barely influences the final result. This is because the shear force and vertical compressive force is not transferred through the head joints but

through the shear and compressive resistance of the bed joints.

7.7. Compressive fracture energy $G_{f,c}$

The compressive fracture energy of the bed joints controls the softening rate of the backbone curve of the force-displacement curve for flexural behaviour. The degradation of the backbone curve can be seen in the force-displacement curve of calibrated analyses for COMP_3 and COMP_6.

For the structures that combine flexural and shear behaviour, such as the COMP_6, increasing compressive fracture energy $G_{f,c}$ of the bed joints will make the structure to keep behaving as a combination of shear and flexure for more cycles (figure 7.6), or even fail in sliding. The reason is that increasing $G_{f,c}$ slows down the softening of the corner due to crushing, and accordingly, the flexural stiffness will not drop too fast. If the shear behaviour is not stiff enough compared with flexural behaviour, the structure will start sliding. Once the sliding begins, the compressive plastic deformation at the corner will not further increase, and it will never get back to flexural failure. That is also the reason why compressive fracture energy $G_{f,c}$ for the bed joints have minimal influence on structure featuring sliding effect, such as the COMP_4. To be more specific, if the structure is sliding, then compressive relative displacement at the corner will be very limited, therefore whether it will soften fast or slow in compression does not matter at all.

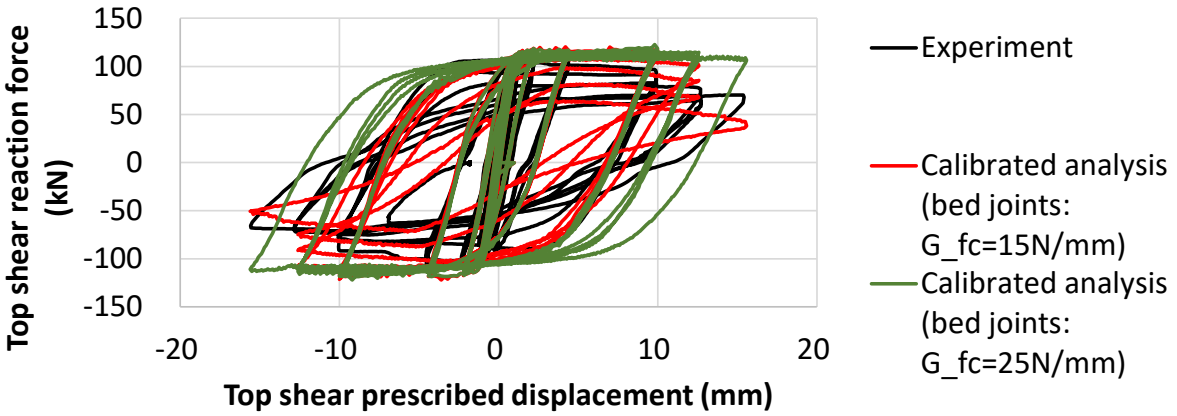

Figure 7.6: Analysis result of the models of COMP_6 with bed joints of $G_{fc} = 15N/mm$ (initial) and with bed joints of $G_{fc} = 25N/mm$ (modified)

Also note that numerically, a too low fracture energy value will require smaller step size or more iterations to converge.

Similarly to the compressive strength of head joints, the compressive fracture energy of the head joints barely influences the overall behaviour.

7.8. Tensile strength f_t and tensile fracture energy $G_{f,t}$

In this thesis, a great proportion of content is to introduce the coupling effect between the tension and shear. However, whether these algorithms are realistic or not cannot be verified directly from these for wall tests. The reason is that the mortar joints are fragile in tension. Many mortar layers will be completely damaged in tension with a small lateral displacement at the top. And because the wall is precompressed, the crack in tension will not directly lead to the failure of the wall. Therefore, it is hard to see its effect until a wall with very little precompression is tested.

Also because of the reasons mentioned above, the value of the tensile strength f_t and tensile fracture energy $G_{f,t}$ of the bed joints have very limited influence on the result as long as they are relatively low compared with compressive strength f_c and compressive fracture energy $G_{f,c}$. For flexural behaviour, increasing both of them can increase the peak capacity of the first several cycles with tiny amplitudes, but after the tensile softening, the force-displacement curve will become the same as the one without increasing f_t and $G_{f,t}$. The crack pattern can only be slightly different.

For the head joints, increasing or decreasing these two parameters even has a smaller impact (figure 7.7). It will only slightly increase or decrease the width of the head joint crack. Actually, at the very early stage of the analysis, most of the head joints have developed extremely small micro-cracks. After the crack is fully developed, whether it will become part of the wide concentrated staircase cracks (usually with the width of several millimeters) or not depends on the shear and compression behaviours of the bed joints. The compression at the bed joints determines their maximum shear capacity and consequently determines their relative shear displacements. If the relative shear displacement of a bed joint is significantly higher than that of the adjacent one, a concentrated head joint crack will develop. Therefore, it is not useful to alter the tensile parameters of the head joints to control the timing of the formation of concentrated wide crack or the width of it, unless they are increased to some unreasonably high value.

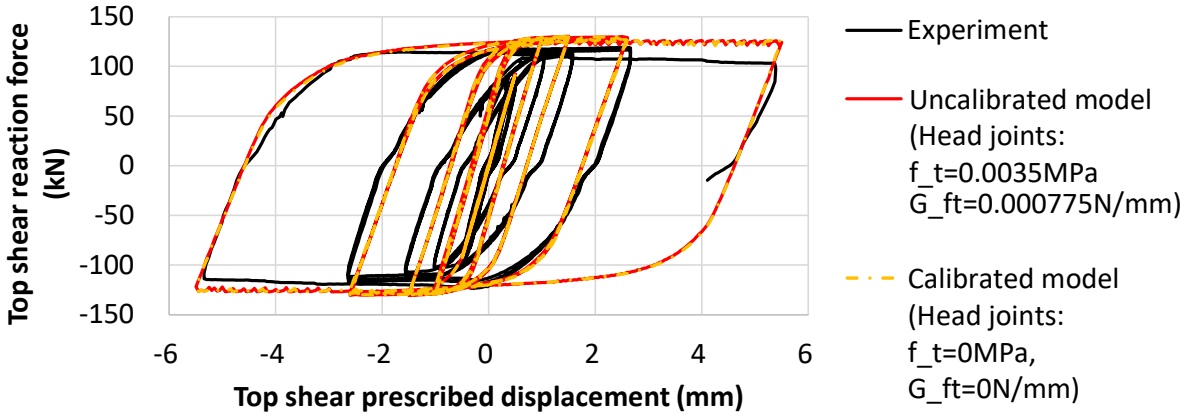

Figure 7.7: Numerical results of the un-calibrated model of COMP_4 (initial) and the model of COMP_4 with head joints of zero tensile strength (modified)

In conclusion, as long as the tensile strengths of bed joints and head joints are in a reasonable range, they will not noticeably influence the force-displacement curve and the crack pattern.

7.9. Cohesion c and shear fracture energy $G_{f,s}$

The value of cohesion c and shear fracture energy $G_{f,s}$ is not important if the cohesion contributes little to the overall shear resistance. The little contribution is defined by a very low cohesion, or a very fast degradation of cohesion (due to low shear fracture energy or possible tensile cracks). In this case, increasing the cohesion and the shear fracture energy can slightly increase the peak of the first several cycles of a wall with shear behaviour, such as COMP_3 and COMP_6. However, the cohesion will deplete in a short time due to the tensile cracks along the same bed joints. Because of the precompression, the shear resistance of the wall is mainly contributed by friction instead of cohesion.

If the cohesion contributes significantly to the shear resistance, and it does not degrade very fast, then changing the value of cohesion c or shear fracture energy $G_{f,s}$ can lead to change of peak lateral capacity of each cycle. This is also the case for the structure with very low precompression, because the lateral resistance is no longer dominant by friction. The wall COMP_4 can be influenced by the change of cohesion and shear fracture energy (figure 7.8 and 7.5). First, the double clamped boundary

condition of this long wall determines that most of the head joints are always in compression, so their cohesion will not suddenly reduce due to tensile cracks. Second, the ultimate relative displacement for the head joint is more than $42mm$ and therefore, cohesion will degrade gradually. The contribution of the cohesion can be estimated by $c/(-\sigma tan(\phi)+c) = 0.14MPa/(0.5MPa \times 0.43 + 0.14MPa) = 39\%$, which is significant. Therefore, changing these shear parameters will influence its result.

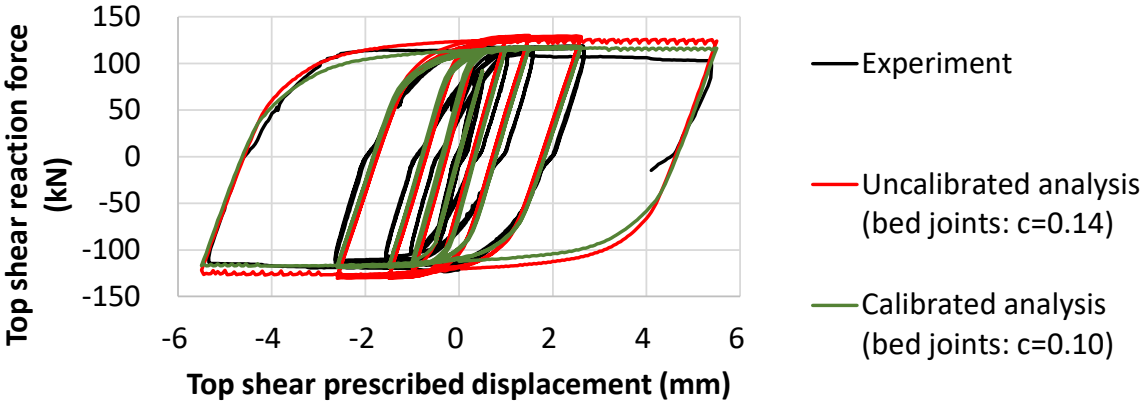

Figure 7.8: Numerical results of the un-calibrated model of COMP_4 (initial) and the model of COMP_4 with head joints of lower cohesion (modified)

7.10. Summary

To sum up, for getting a reasonable result of the analysis, all the parameters in the head joints have little influence on the overall behaviour. Among all the parameters for bed joints, the most sensitive parameters are the compressive strength f_c, relative displacement corresponding to the strength $d_{c,peak}$ and compressive fracture energy $G_{f,c}$, which characterize the compressive curve, This is especially the case for wall featuring flexural failure. The friction angle ϕ is also crucial to determine the peak capacity of sliding and determine if it will fail in flexure or shear. Also note the ways that these input parameters influence the structural behaviour is also consistent with the understanding of mechanics.

The conclusions made above are based on the limited number of wall models tested and may not represent the other circumstances.

8

Conclusions, discussion and future work

8.1. Conclusions

This thesis proposes an iterative constitutive model with sub-increments for interface elements used in the discrete crack model for masonry. The constitutive model is based on the multi-surface plasticity criterion that includes tension cut-off, compression cut-off and Coulomb friction. The theories and assumptions behind are thoroughly demonstrated in chapter 3, with all the formulas derived based on reasonable mechanics understanding. The essence of this constitutive model is as follows:

1. The pair of total increments of relative shear and normal displacements provided by the FEA program is divided into more pairs of sub-increments to resolve the weakness of loading the structure in normal and shear directions sequentially, in consideration of the possible path dependency of the plastic process.
2. For each pair of sub-increment, the uni-axial loading algorithm is applied first in the normal direction and then in the shear direction. The uni-axial loading algorithm utilizes the uni-axial constitutive curves for tension, compression, and shear, incorporated with one of the two proposed Coupling Options.
3. After the uni-axial loading in either of these two directions, the iterative damage calculation algorithm is used to ensure the updated stress state (shear and normal stresses) is on the yield surface defined by the updated damage factors.

The combination of the uni-axial loading algorithm and the iterative damage calculation algorithm eliminates the mapping-back process in conventional elastoplastic constitutive models.

With a clear code structure, various modules are written to compose the proposed constitutive model, including the Constitutive Array Re-constructor, the Elastic Predictor, the Elastic Calculator, the Elastic Limit Finder, and most importantly, the Plastic Calculator. The module of Plastic Calculator further includes the Normal and Shear Uni-axial Plastic Loader as well as the Damage Calculator as the realization of the two core algorithms mentioned above. All these modules are visualized with flow charts to show the overview and details of their structure in chapter 4.

In chapter 5, the code is tested qualitatively on single integration point level. To be specific, the evolution of stress state during the calculation is reviewed in the shear and normal coordinates and the coordinate of the yield surfaces. Different combinations of initial relative displacements and increments of relative displacements are tested in the same manner to cover most of the circumstances of plastic loading.

The results indicate good stability of the iterative algorithms. Moreover, the differences between the two Coupling Options of uni-axial loading are discussed. There are scenarios when one of the two Options yields more conservative result or both of them yield identical result. The conclusion regarding which one is more accurate cannot be made until further validation against experiments. Also, the necessity of sub-increments is confirmed, and the convergence rate is $O(n^1)$.

In chapter 6, the code is validated quantitatively on wall level. That is, three wall models are analyzed and compared with the experimental results of these three walls. The three walls presented have different geometrical and boundary conditions, and each one represents a different type of failure—pure shear failure, flexural failure, or finally, the combination of flexure and shear. The comparison shows that this constitutive model is more capable of modelling shear behaviour than flexural behaviour. With some calibrations of input parameters, the flexural behaviour can also be well simulated.

Finally, in chapter 7, the influence and sensitivity of different input parameters are discussed to provide guidelines for the required accuracy of each parameter for a satisfactory analysis.

The major conclusions of this thesis are:

1. The proposed sub-increment based iterative constitutive model successfully eliminates the mapping-back process. The iterative algorithm is found to be numerically stable for all tested loading conditions, and the convergence rate of the sub-increment is $O(n^1)$. The constitutive model is also robust for all the wall analyses performed, without encountering any divergence;

2. The constitutive model has incorporated reasonable loading and unloading behaviours for tension, compression, and shear, such that it is capable of applications in cyclic analyses. It can cover the majority of shear and flexural failure mechanisms, including rocking, shear sliding, diagonal cracking, and toe crushing;

3. The model can very accurately model shear behaviour, and it can also model the flexural behaviour well with some calibrations. The satisfactory accuracy herein means the good agreement between analyses and experiment on various aspects, including initial stiffness, stiffness at the end of the analysis, loading capacity, energy dissipation, crack pattern, degradation within each cycle and failure mechanism;

4. The constitutive model is not step-size and mesh-size dependent. Refining the step size and the mesh size can smoothen the force-displacement curve and slightly change the width of the crack, but the overall behaviour will not alter. This feature can reduce the computational time while still ensuring a certain amount of accuracy;

5. Straightforward formulas are provided to calculate the input parameters from the material properties. In addition, an example is given, which describes in detail how to obtain input parameters for the analyses of wall COMP_3, COMP_4, and COMP_6;

6. The parameter study based on the tested masonry walls indicates that the constitutive model is almost insensitive to the input parameters of the head joints. For the bed joints, it is most sensitive to the compressive strength, the relative displacement corresponding to the compressive strength, and the friction angle. It is insensitive to tensile strength and tensile fracture energy, as the masonry wall is very weak in tension and usually precompressed. The fact that this constitutive model is not sensitive to parameters that are hard to be measured through experiments eases the users' efforts needed to estimate them.

The first three points indicate the robustness, accuracy, and reliability of the proposed sub-increment based iterative constitutive model. The fourth to sixth points ensure that the constitutive model is feasible in engineering practices.

8.2. Critical reflection

From the analyses of the masonry wall, it is clear that the wall models usually underestimate the toe crushing behaviour in flexure if the compressive strength f_c of the bed joint is not reduced to a low level. From the experiment of the masonry wall with flexural behaviour, we can see that most of the toe crushing is actually characterized by the splitting of the bricks in the direction parallel to the vertical compressive stress. Also, according to the numerical analysis, the bricks at the bottom corner shows very low levels of tensile stress, or even for most of the time, the corner bricks are biaxially compressed. Therefore splitting is not due to the tensile stress in the horizontal direction. In fact, it is due to the excessive compressive stress in the vertical direction that enlarges the vertical micro-cracks in the bricks, or due to the vertical cracks in the bed joints that propagate into the bricks. This means that adding an extra dummy interface element at the center of the brick will not be able to capture the splitting crack. Moreover, in the experiment, after the splitting, the flexural stiffness (horizontal stiffness) of the bricks degrades such that the contact area for compression increases, and the center of the compressive zone shifts from the corner towards the center of the wall, which could reduce the peak shear capacity of the force-displacement curve. In the analysis, even if the interface elements of the bed joints can deform vertically as if toe crushing occurs, the stiffness of the bricks cannot be reduced, so the contact area of compression remains small and close to the edge. Therefore, the peak capacity of a masonry wall with flexural failure is often overestimated. A possible remedy is to reduce the compressive strength f_c of the bed joints such that the compressive zone will be larger and similar to the reality.

In addition, the discrete crack model should be used with caution for cases where large shear deformations are expected, no matter which constitutive model is adopted. The large deformation defined herein refers to when the real contact length between the master and the slave interface is noticeably smaller than the length of the interface itself. In the case of an excessive amount of relative shear displacement, the compressive stress at this interface can no longer be calculated by dividing the nodal force by the length and the width of that element. Instead, it should be divided by a reduced contact area. This is usually the case for the staircase cracks with huge head joint openings. In this situation, the contact area of the bed joints along the staircase crack is smaller, and the vertical force that the bed joints is required to carry can only be carried by a smaller area now, which leads to the splitting of the adjacent bricks and the crushing of the bed joints; translating this to our numerical model, the compressive stress of the integration point should be much higher meaning that crushing of this interface element of the bed joints might have already occurred. Also, due to the reduction of the contact area, the bed joint might also be unable to provide enough frictional resistance, if the compressive stress is limited by the compressive strength. Including geometrical nonlinearities will not solve the problem. Unlike continuum elements that take into account the extra in-plane moment induced by force on the nodes of the new deformed shape, interface elements cannot identify the extra moment of the sheared nodes. This is because of the nature of the interface elements. The two nodes of a line interface element are uncoupled, like two independent springs. Extra moment due to geometrical nonlinearity cannot be applied on a single spring without deformation of the adjacent spring at the same time. Not to mention that the interface element of the bed joint cannot obtain the crack width of the head joint above it, so the reduction of the contact area is an impossible task to realize. A possible remedy is also to reduce the compressive strength f_c of the bed joints if the width of the crack in the head joints can be correctly estimated.

However, it is crucial to realize that the discussions above are both the general weaknesses of the interface elements or the discrete crack model, despite the constitutive model used. The reduction of compressive strength could be a common method to remedy these two weaknesses for all discrete crack models. This can be achieved by manually calibrating the input compressive strength. A possibly better approach might be to use a compressive cap (refer to figure 2.4 in section 2.3.1) instead of the compression cut-off in the multi-surface plasticity criterion, and at the same time, to couple the maximum capacities of compression and shear as it is done for tension and shear. By doing so, the maximum compressive capacity is automatically reduced when the shear stress is high. And accordingly, using one of the Coupling Options purposed, the compressive softening can occur without reaching the input compressive strength.

The shortcoming that is particularly of this thesis lies in the lack of verification of the proposed coupling effect between tension and shear. The constitutive model can robustly ensure that the updated stress state is on the updated yield surface after a plastic process. However, being correct in terms of plasticity concepts is not equal to being realistic. Whether the location of the final stress state or the amount of damage is correct or not remains uncertain until it is validated against experimental results. For structures like masonry walls, which are usually precompressed, it might not be an urging problem to solve. Actually, there are barely any masonry experiments that investigate the combination of tension and shear. Therefore the coupling effect of tensile and shear stresses in masonry interfaces cannot be validated easily. However, if this constitutive model is applied to a different type of surface where a combination of shear and tensile failure often occurs, then the loss of cohesion and tensile strength dominate the behaviour. For such kind of application, whether this algorithm returns the correct amount of stresses and damage should be further investigated.

8.3. Future work

As mentioned multiple times in this thesis, the key factor in an accurate simulation of flexural behaviour is to model the compressive behaviour better. The compressive curves used in this model are not that ideal for ductile hardening behaviour. Therefore more work could be done in the future on trying to develop a better formulation of the compressive curve in order to possibly allow better modelling of the toe crushing behaviour, without a dramatic reduction of the compressive strength f_c of the bed joints. On the other hand, if we keep the existing compressive curve, one could try to derive an analytical or empirical formula to estimate the amount of reduction needed for compressive strength f_c of the bed joints for more accurate results. Furthermore, as is discussed in the last section, the compressive cap, in place of the compression cut-off, can be adopted in the multi-surface plasticity criterion, with maximum capacities of compression and shear coupled. It might be able to allow softening in compression before the compressive stress reaches the (uncalibrated) input compressive strength. This could limit the compressive stress and further limit the shear stress that originally leads to the overestimation of lateral force.

In addition, below are listed some more points that could be instereting for future research:

- The coupling solution between tension and shear proposed in this thesis need to be validated and maybe modified based on experiments;
- All the models above were run with a maximum of 100 sub-increments, which is believed to be already very accurate as if the tension and shear are loaded simultaneously. However, to what extent changing the maximum value will influence the accuracy is not yet studied;
- More types of wall typologies can be tested with this constitutive model to further investigate the capability of this constitutive model. More comprehensive parametric studies could be performed in the future, to investigate the influence and sensitivity of more input parameters on different types of masonry walls;
- Comparison between the proposed iterative constitutive model against the existing constitutive models can be made. It could be in various aspects such as accuracy, computational time, robustness, etc.;
- In this thesis, cyclic analyses are included. More tests can be done with time history analysis to test its robustness;
- The proposed constitutive model is designed for 1D interface elements. The future study can further apply it to 2D interface elements.

A

Derivation of relation of softening stiffness

In this appendix, the relations between the softening stiffness $K_{s,so}$ $K_{t,so}$ of the interface element in FE model and the softening stiffness $K'_{s,so}$ $K'_{t,so}$ of the cracked surface in the mechanical model in shear and tension direction are discussed. The softening stiffness do to crushing of the mechanical model in compression is not mentioned in this thesis as it is not needed in the algorithm of this constitutive model.

Consider the simple structure composed of two units and a mortar joint as it has been introduced in figure 3.1 in chapter 3. Now that real structure has been loaded in shear direction in term of prescribed displacement at the top of the upper unit, as shown in figure 3.2.

Assume that as the shear load increases, both the mortar layer and the units deform. This also results in an increase of relative displacement of the interface element in the FE model. And at a certain stress state, due to the relatively weaker mortar joint and the imperfection somewhere in this joint, the stress of a certain horizontal cross-section of the joint will reach the shear strength first, and the shear crack initiates along that cross-section. Before the crack initiates, no relative displacement exists for the potential cracked surface. As the prescribed displacement continuously increases, the relative displacement along that crack emerges and increases, as shown in figure A.1. The internal shear force and the shear deformation of the other parts, including the intact mortar layer and the upper and lower units, will decrease as the crack further develops. The development of the crack is associated with the increase of the relative displacement of that ideal crack in orange and the decrease of the load it can carry, also called as softening. Note that even for the real structure in orange line, it is assumed that all the plastic deformation concentrated at that idealized crack line, which might be different from the reality but still reflects the mechanical behaviour which the real structure will have. Also note that this crack in orange can be any horizontal line in that mortar joint and it is not necessary for it to be at the same line as the zero-thickness interface element.

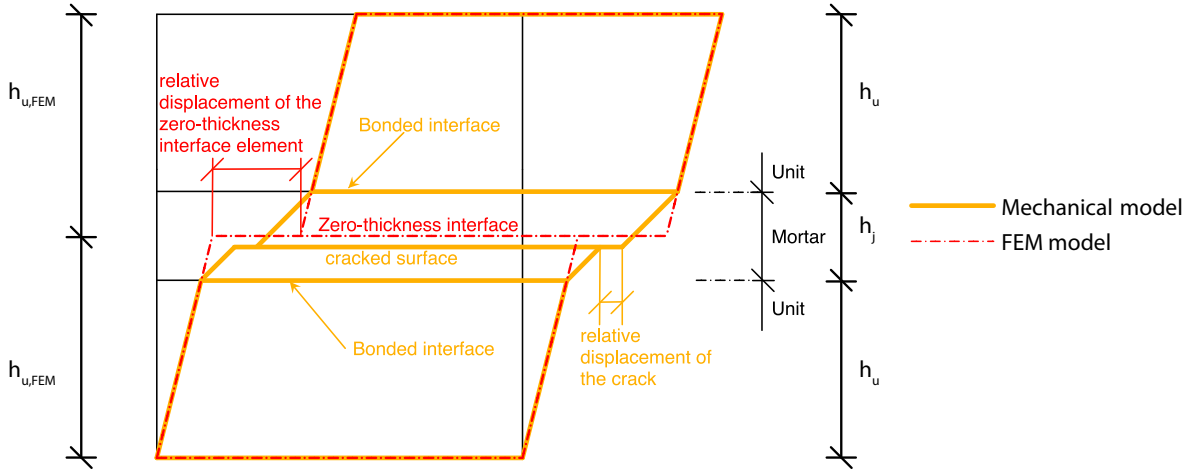

Figure A.1: Detailed mechanical model loaded in shear (orange) and its FE model (red) after cracked

Before the crack initiate, the potential cracked surface has a dummy stiffness (much higher value than the stiffness of the mortar). After the crack initiate, in the FE model, the softening branch of the stress-relative displacement curve of the cracked interface and the part of units which are originally the joint follows the below linear relation:

$$d_s = (\frac{h_j}{G_u} + \frac{1}{K_{s,so}})\tau + (\frac{1}{K_{s,e}} - \frac{1}{K_{s,so}})f_s \tag{A.1}$$

where
h_j: the height of the cracked masonry joint layer.
$K_{s,so}$: the shear softening stiffness of the zero-thickness interface element.

And in mechanical model, the softening branch of stress-relative displacement curve of the cracked joint follows the below linear relation:

$$d_s = (\frac{h_j}{G_j} + \frac{1}{K'_{s,so}})\tau - \frac{1}{K'_{s,so}}f_s \tag{A.2}$$

where $K'_{s,so}$ is the shear softening stiffness of the cracked surface in the mechanical model.

To make sure that the mechanical model and the FE model behave exactly the same, the equation A.1 and A.2 should be identical. Combined with equation 3.3, the following condition can be derived.

$$\frac{1}{K_{s,so}} = \frac{1}{K_{s,e}} + \frac{1}{K'_{s,so}} \tag{A.3}$$

Hereby the relation between the shear softening stiffness of the cracked surface in the mechanical model and the softening stiffness of the interface element is derived.

Similarly, in tension, the softening branch of the stress-relative displacement curve of the FEM simplified discrete crack model and the mechanical model can be written as equation A.4 and A.5 respectively.

$$d_t = (\frac{h_j}{E_u} + \frac{1}{K_{t,so}})\sigma + (\frac{1}{K_{t,e}} - \frac{1}{K_{t,so}})f_t \tag{A.4}$$

where $K_{t,so}$ is the tensile softening stiffness of the zero-thickness interace element.

$$d_t = (\frac{h_j}{E_j} + \frac{1}{K'_{t,so}})\sigma - \frac{1}{K'_{t,so}} f_t \tag{A.5}$$

where $K'_{t,so}$ is the tensile softening stiffness of the cracked surface in the mechanical model.

By combining the equation A.4, A.5 and 3.7, the relation between the shear softening stiffness of the cracked surface in the mechanical model and the shear softening stiffness of the interface element can be derived as follows.

$$\frac{1}{K_{t,so}} = \frac{1}{K_{t,e}} + \frac{1}{K'_{t,so}} \tag{A.6}$$

B

Calculation processes of 11 tests on integration point level

The results of the 11 tests conducted on integration point level are as follows:

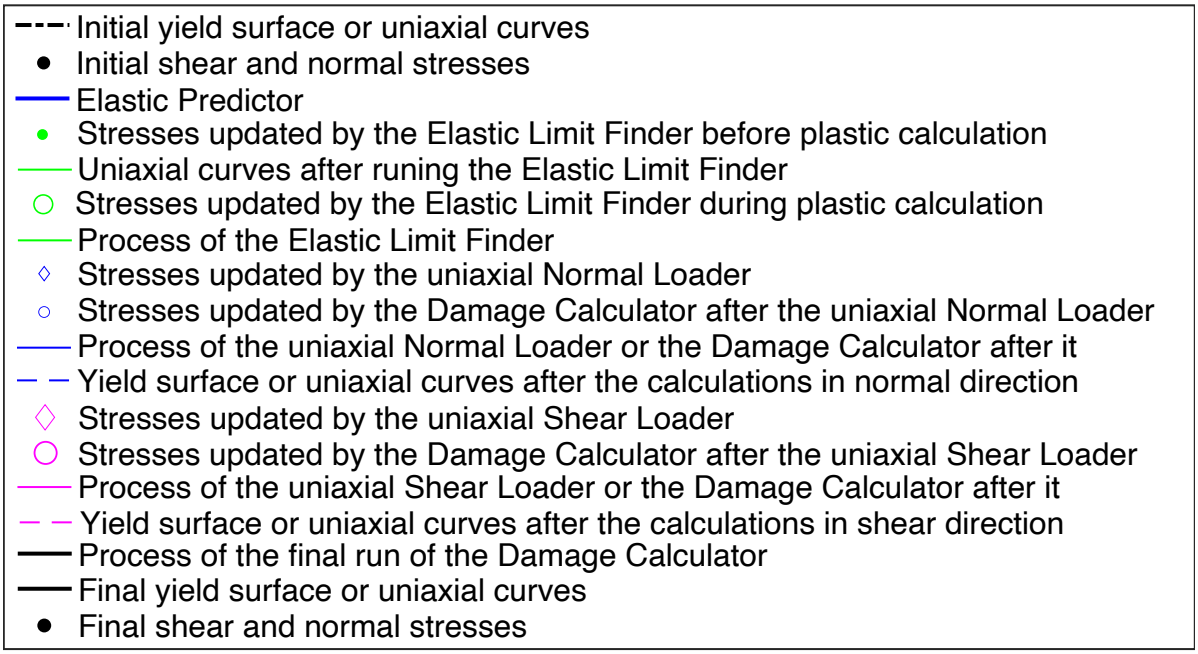

Figure B.1: Common legend for all the figures in this chapter

B.1. Test No.1

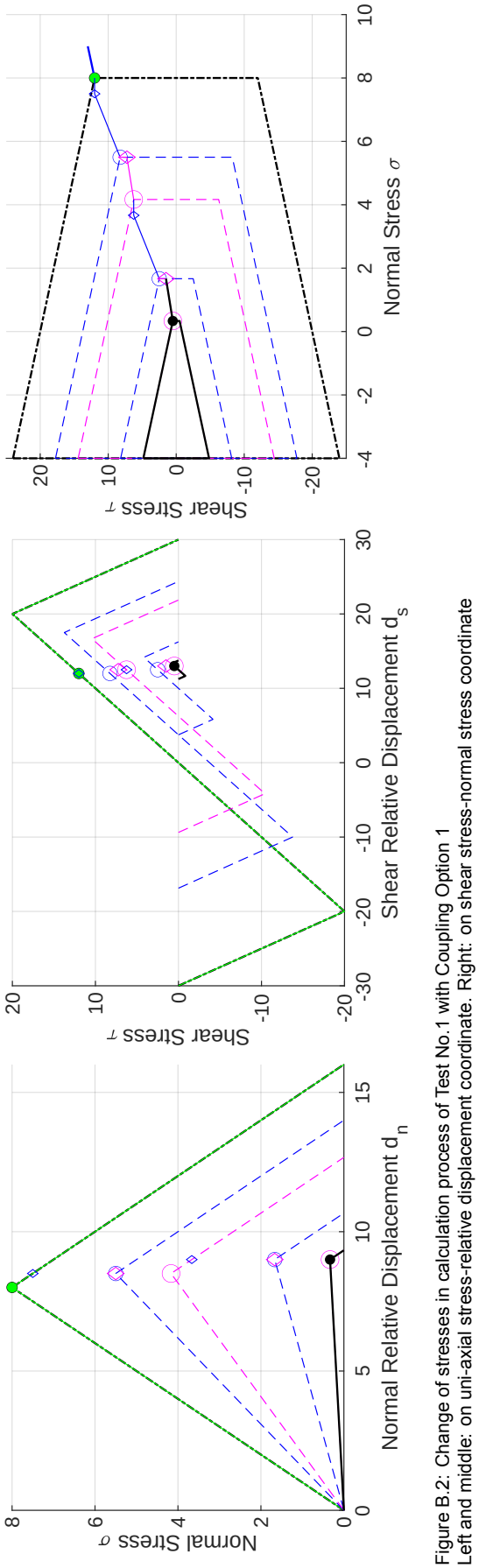

Figure B.2: Change of stresses in calculation process of Test No.1 with Coupling Option 1
Left and middle: on uni-axial stress-relative displacement coordinate. Right: on shear stress-normal stress coordinate

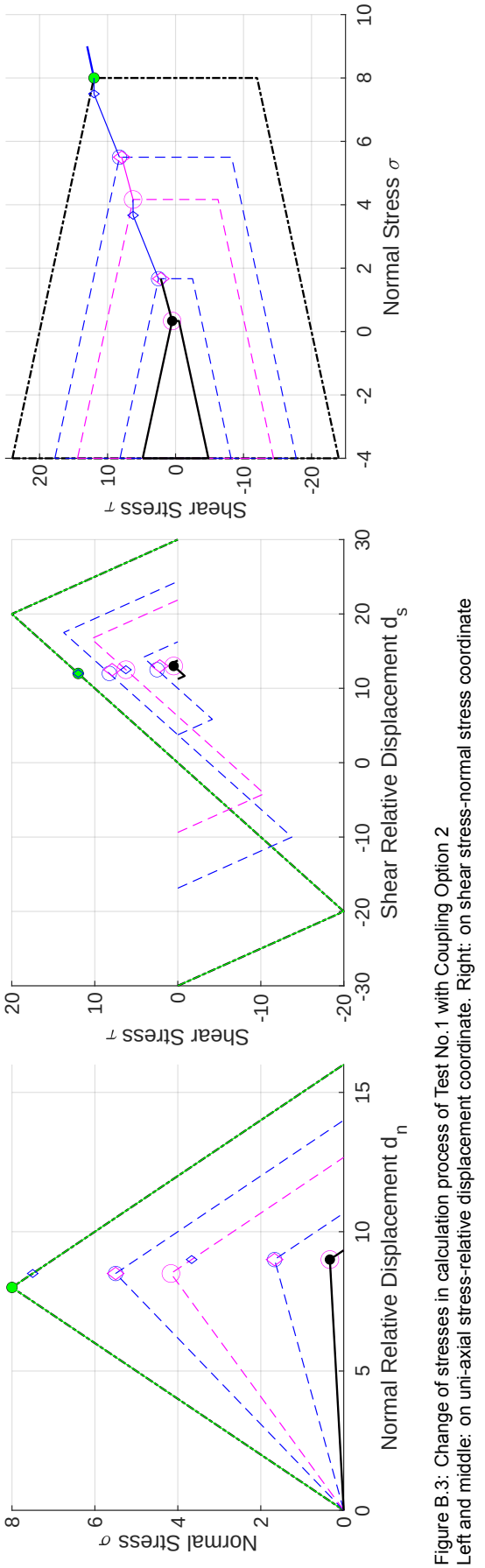

Figure B.3: Change of stresses in calculation process of Test No.1 with Coupling Option 2
Left and middle: on uni-axial stress-relative displacement coordinate. Right: on shear stress-normal stress coordinate

B.2. Test No.2

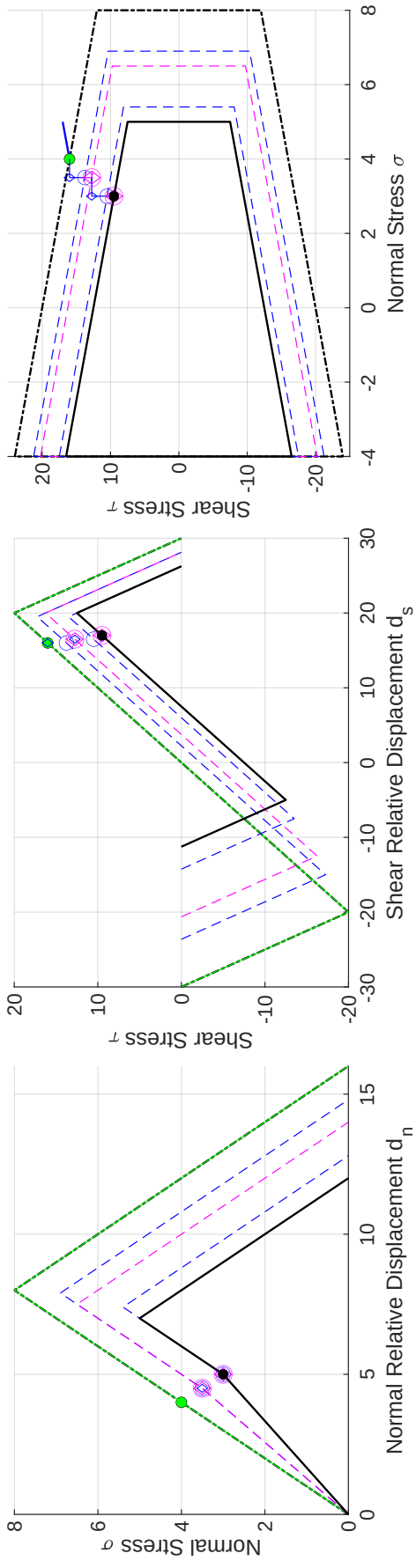

Figure B.4: Change of stresses in calculation process of Test No.2 with Coupling Option 1
Left and middle: on uni-axial stress-relative displacement coordinate. Right: on shear stress-normal stress coordinate

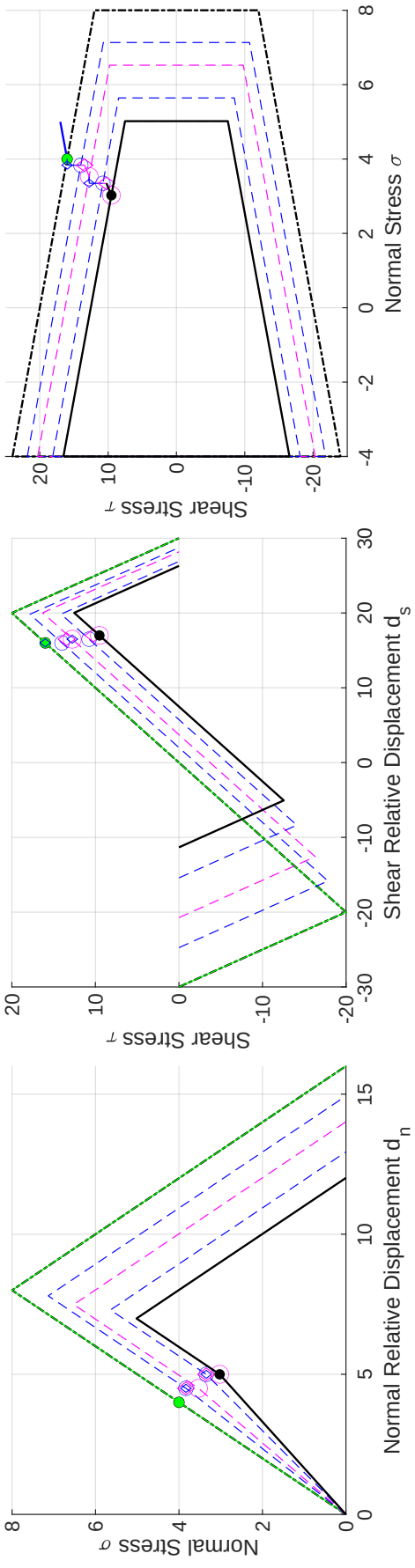

Figure B.5: Change of stresses in calculation process of Test No.2 with Coupling Option 2
Left and middle: on uni-axial stress-relative displacement coordinate. Right: on shear stress-normal stress coordinate

B.3. Test No.3

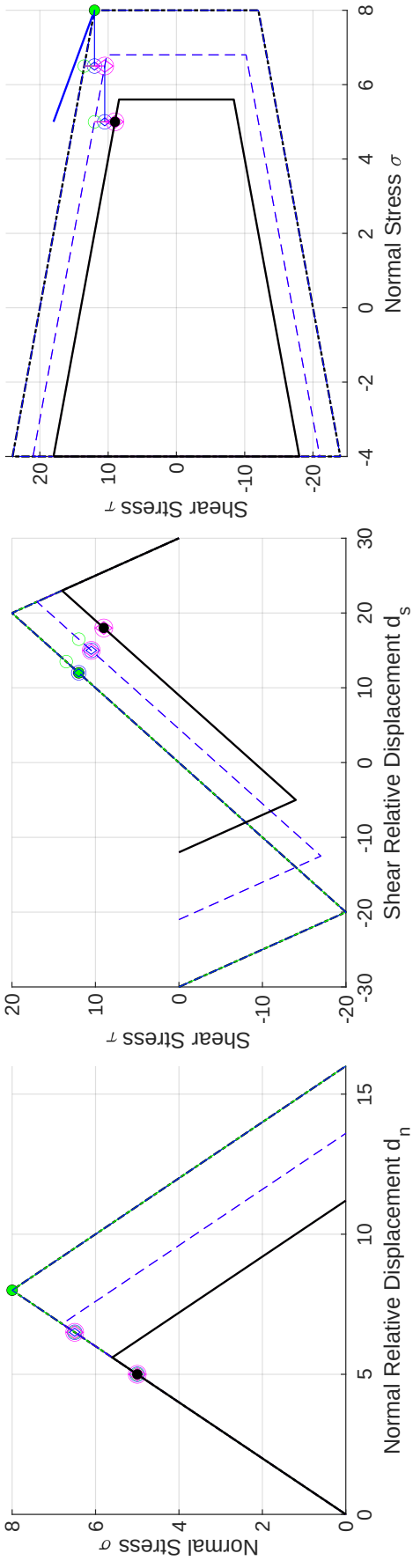

Figure B.6: Change of stresses in calculation process of Test No.3 with Coupling Option 1
Left and middle: on uni-axial stress-relative displacement coordinate. Right: on shear stress-normal stress coordinate

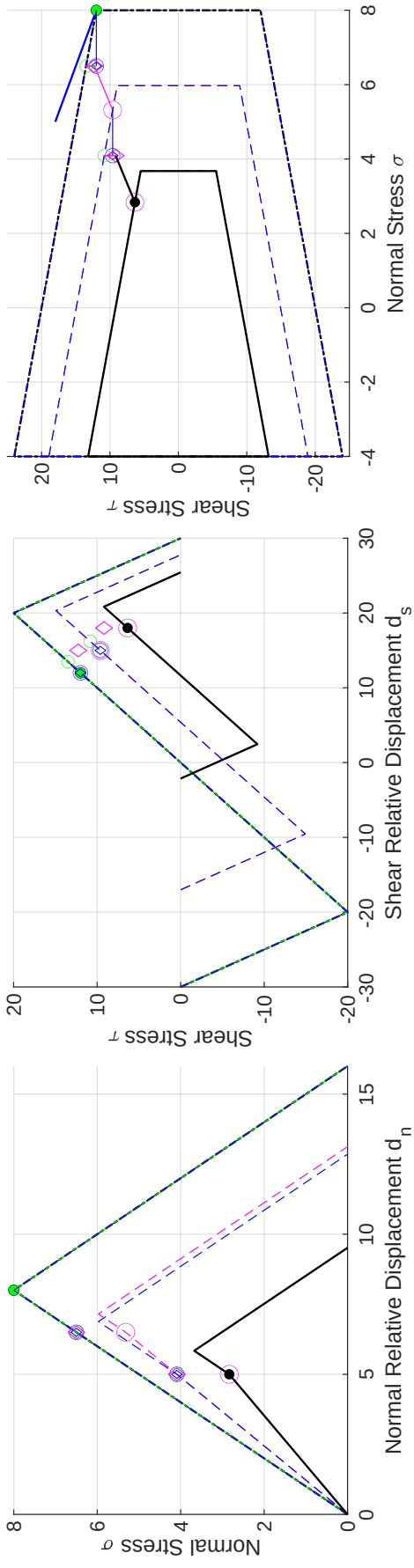

Figure B.7: Change of stresses in calculation process of Test No.3 with Coupling Option 2
Left and middle: on uni-axial stress-relative displacement coordinate. Right: on shear stress-normal stress coordinate

B.4. Test No.4

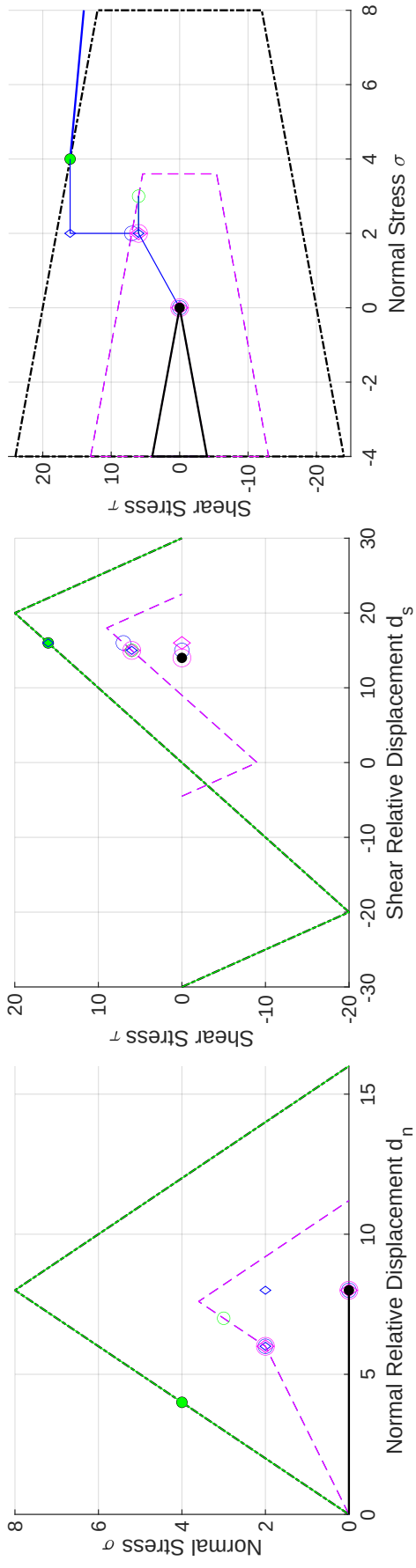

Figure B.8: Change of stresses in calculation process of Test No.4 with Coupling Option 1
Left and middle: on uni-axial stress-relative displacement coordinate. Right: on shear stress-normal stress coordinate

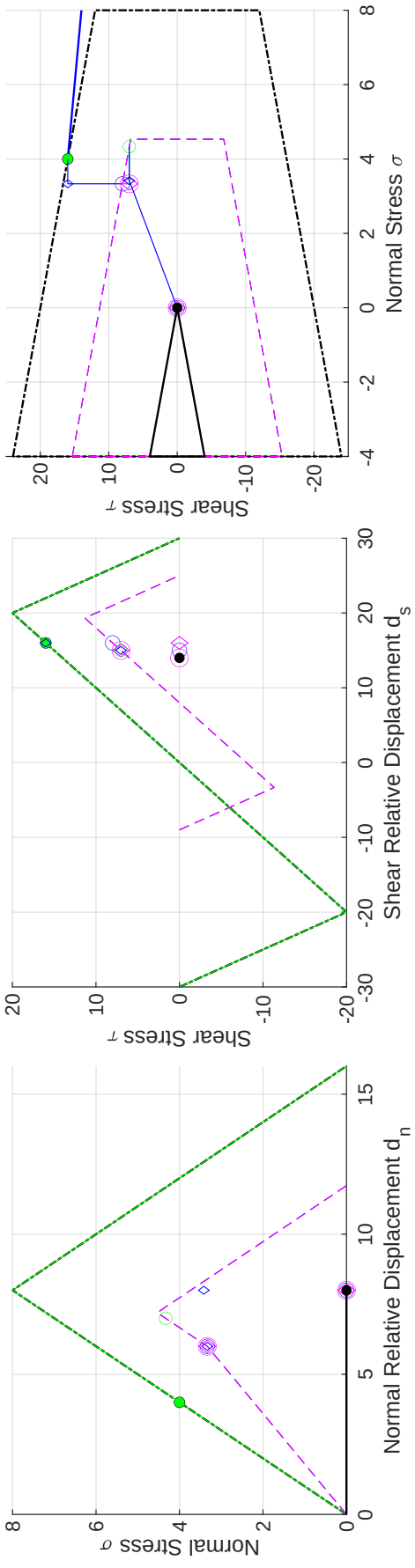

Figure B.9: Change of stresses in calculation process of Test No.4 with Coupling Option 2
Left and middle: on uni-axial stress-relative displacement coordinate. Right: on shear stress-normal stress coordinate

B.5. Test No.5

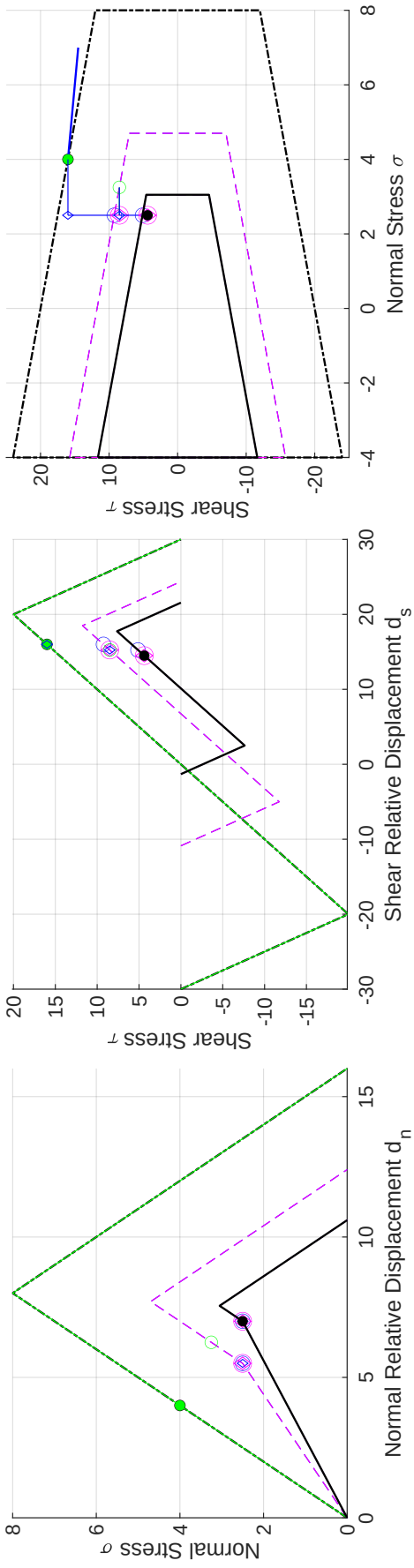

Figure B.10: Change of stresses in calculation process of Test No.5 with Coupling Option 1
Left and middle: on uni-axial stress-relative displacement coordinate. Right: on shear stress-normal stress coordinate

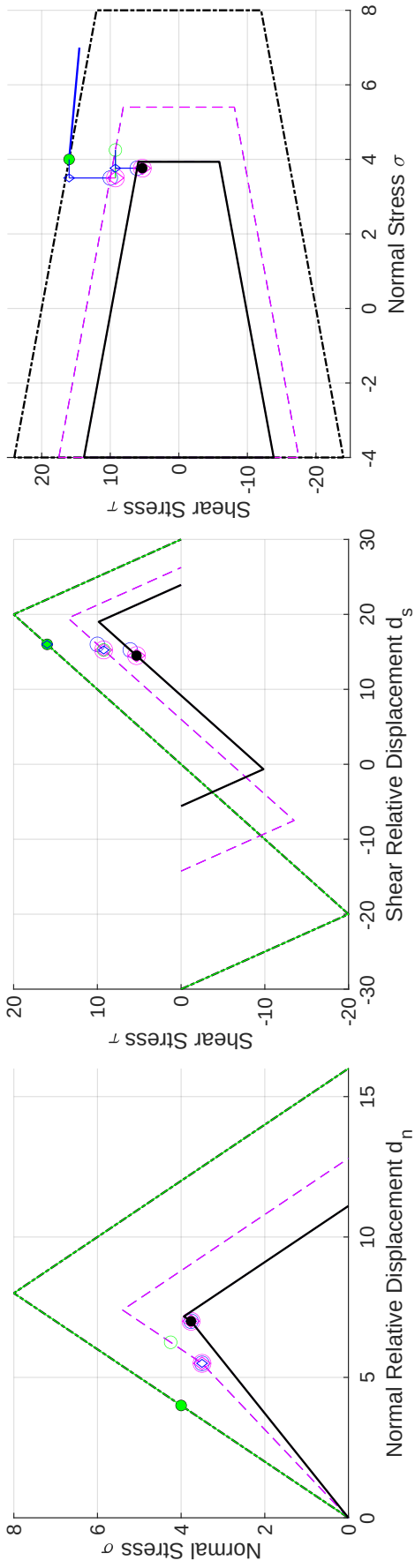

Figure B.11: Change of stresses in calculation process of Test No.5 with Coupling Option 2
Left and middle: on uni-axial stress-relative displacement coordinate. Right: on shear stress-normal stress coordinate

B.6. Test No.6

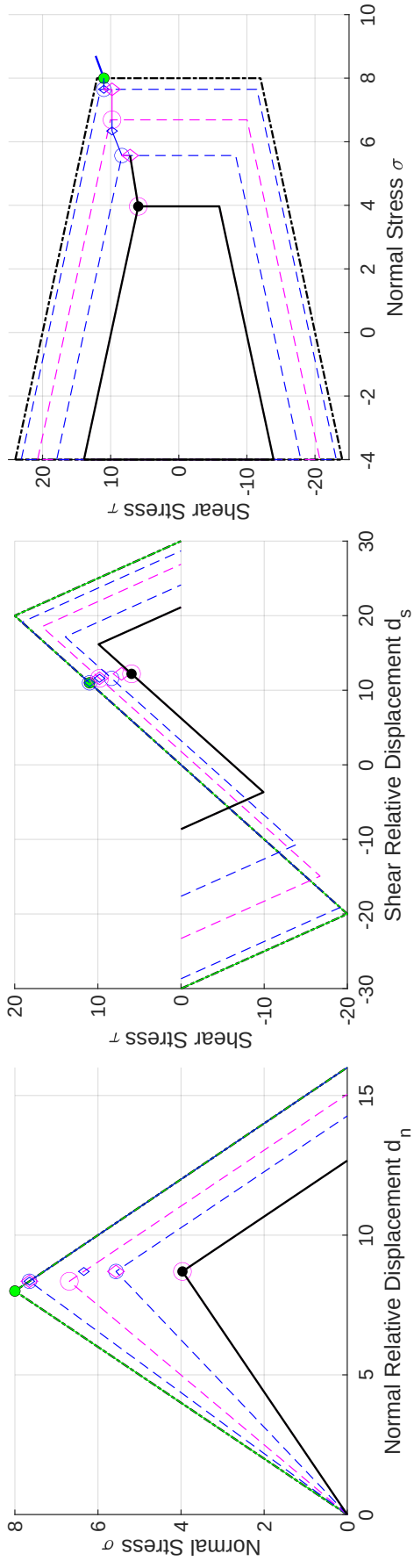

Figure B.12: Change of stresses in calculation process of Test No.6 with Coupling Option 1
Left and middle: on uni-axial stress-relative displacement coordinate. Right: on shear stress-normal stress coordinate

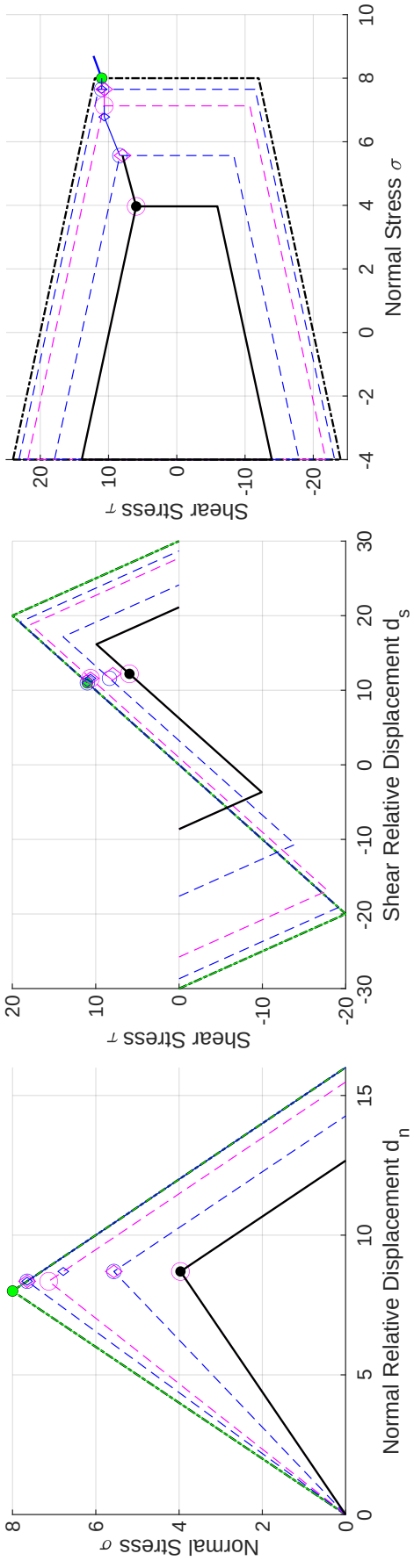

Figure B.13: Change of stresses in calculation process of Test No.6 with Coupling Option 2
Left and middle: on uni-axial stress-relative displacement coordinate. Right: on shear stress-normal stress coordinate

B.7. Test No.7

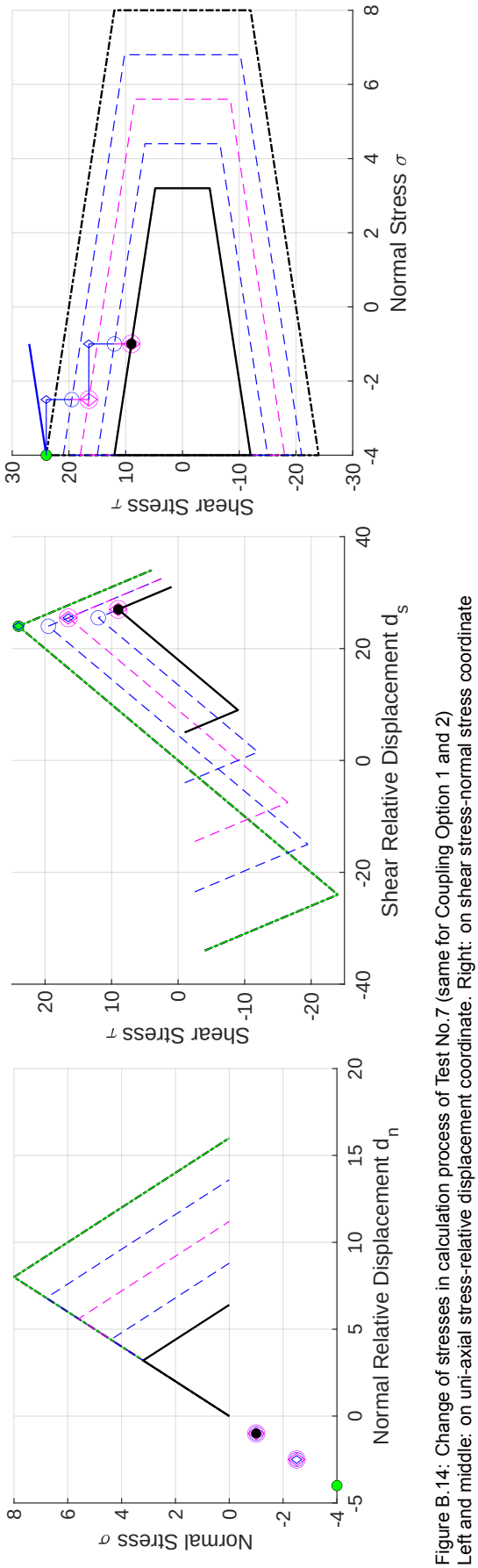

Figure B.14: Change of stresses in calculation process of Test No.7 (same for Coupling Option 1 and 2)
Left and middle: on uni-axial stress-relative displacement coordinate. Right: on shear stress-normal stress coordinate

B.8. Test No.8

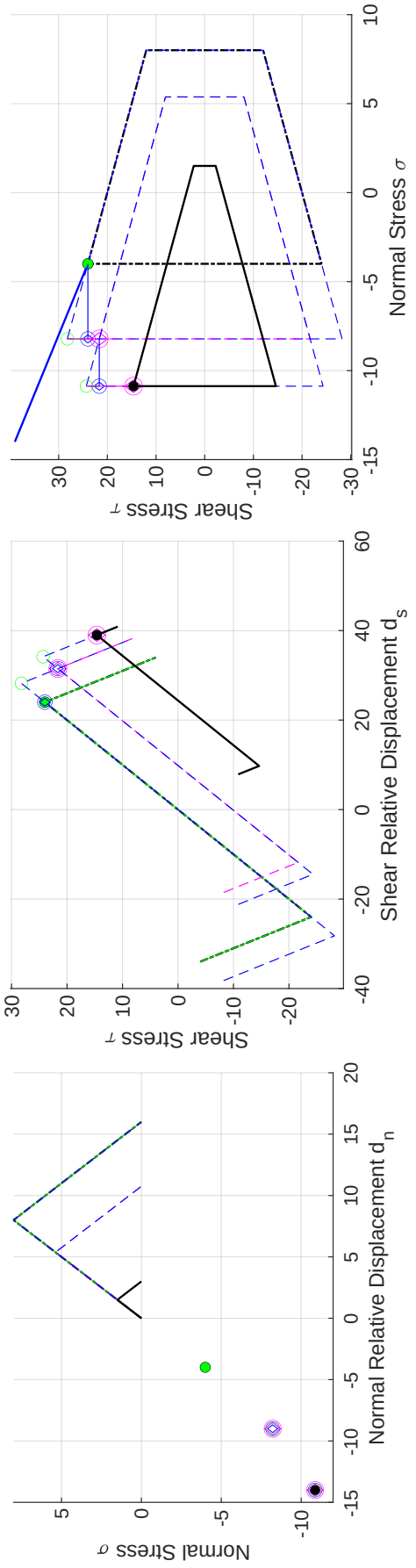

Figure B.15: Change of stresses in calculation process of Test No.8 (same for Coupling Option 1 and 2)
Left and middle: on uni-axial stress-relative displacement coordinate. Right: on shear stress-normal stress coordinate

B.9. Test No.9

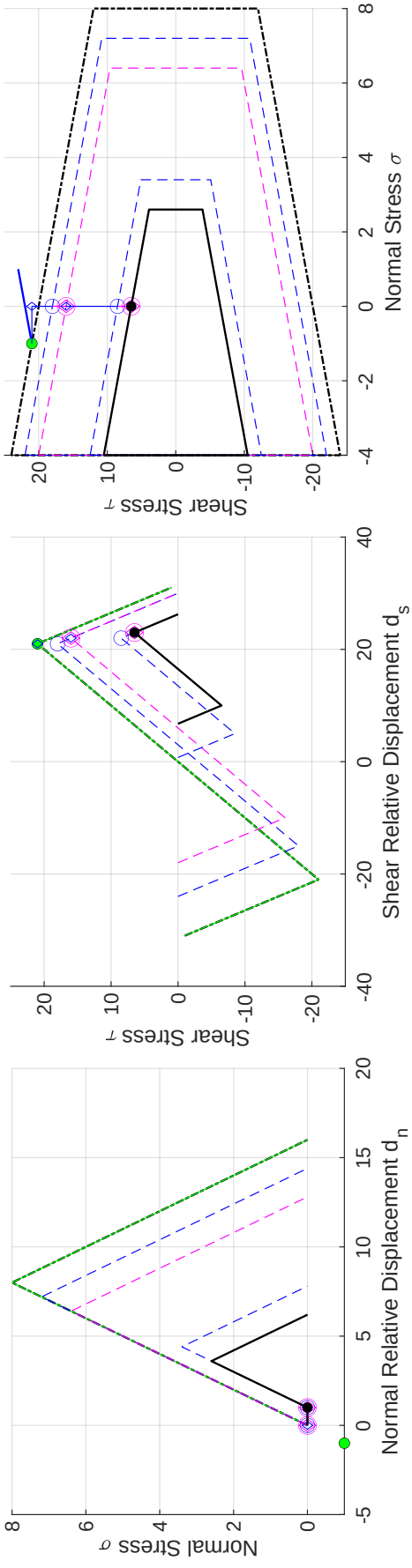

Figure B.16: Change of stresses in calculation process of Test No.9 with Coupling Option 1
Left and middle: on uni-axial stress-relative displacement coordinate. Right: on shear stress-normal stress coordinate

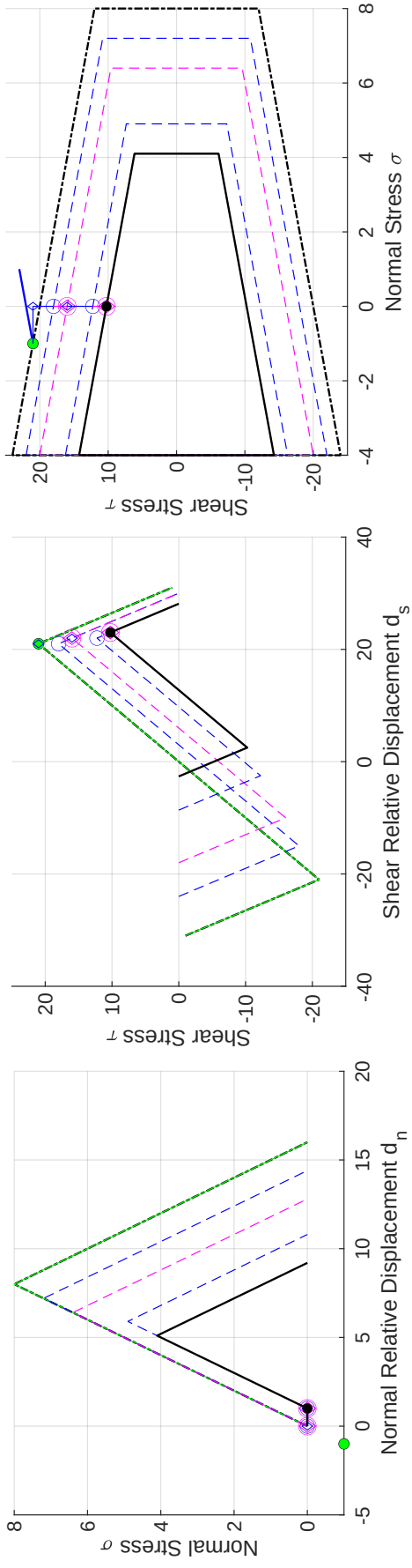

Figure B.17: Change of stresses in calculation process of Test No.9 with Coupling Option 2
Left and middle: on uni-axial stress-relative displacement coordinate. Right: on shear stress-normal stress coordinate

B.10. Test No.10

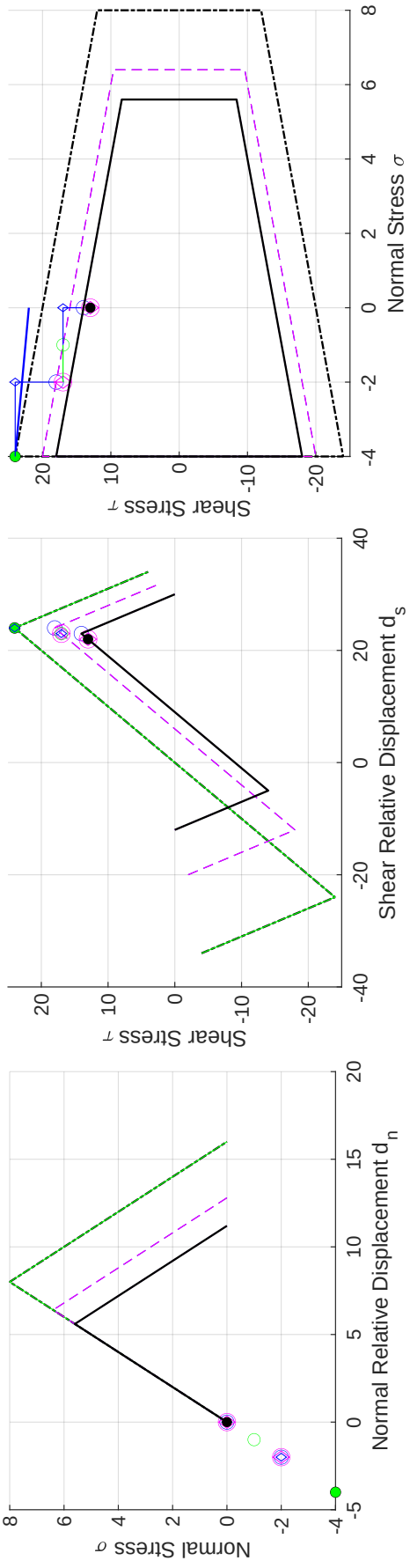

Figure B.18: Change of stresses in calculation process of Test No.10 (same for Coupling Option 1 and 2)
Left and middle: on uni-axial stress-relative displacement coordinate. Right: on shear stress-normal stress coordinate

B.11. Test No.11

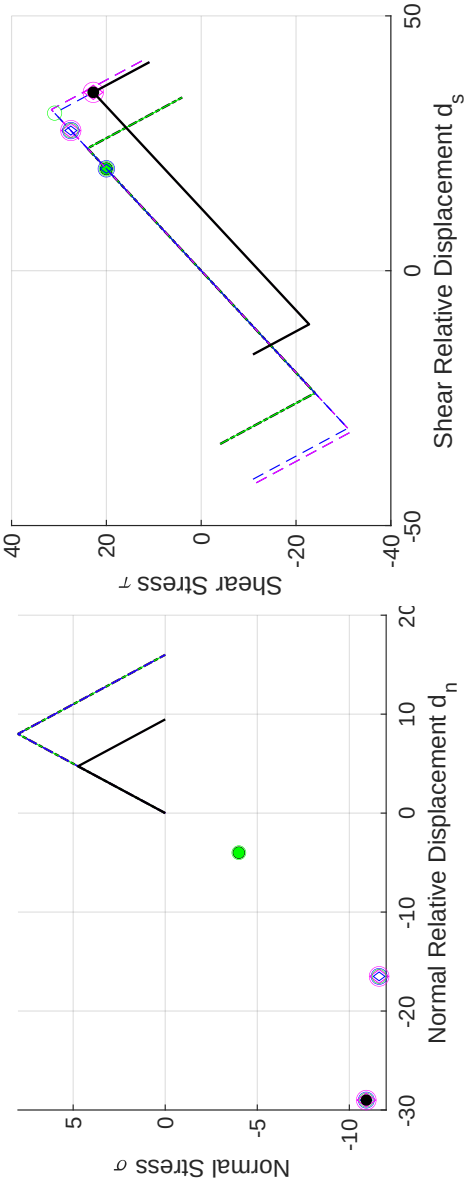

Figure B.19: Change of stresses in calculation process of Test No.11 (same for Coupling Option 1 and 2) on uni-axial stress-relative displacement coordinate

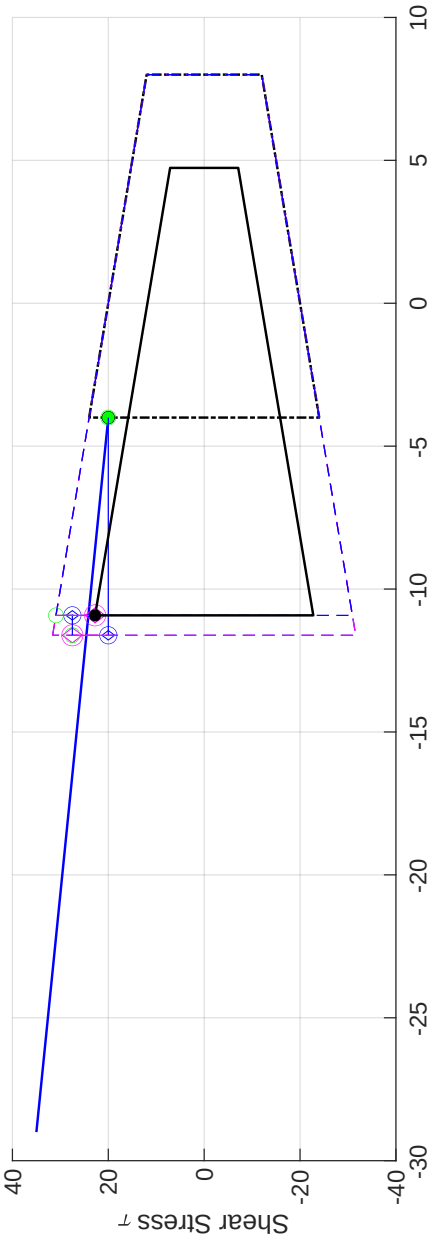

Figure B.20: Change of stresses in calculation process of Test No.11 (same for Coupling Option 1 and 2) on shear stress-normal stress coordinate

C

Overview of material tests

This table is table 54 in the report of Material characterisation of replicated masonry and wall ties [2].

Table C.1: Overview of mechanical properties for calcium silicate and clay masonry obtained in the first testing period

Property	Symbol	Unit	Calcium silicate masonry			Clay masonry		
			Average	St. dev.	C.o.V.	Average	St. dev.	C.o.V.
Compressive strength of mortar	f_m	MPa	**6.59**	0.66	0.10	**6.11**	0.57	0.09
Flexural strength of mortar	f_{mt}	MPa	**2.79**	0.22	0.08	**2.43**	0.32	0.13
Flexural strength of masonry unit	f_{bt}	MPa	**2.74**	0.16	0.06	**4.78**	0.94	0.20
Elastic modulus of masonry unit	E_b	MPa	**8990**	3202	0.36	**7211**	3849	0.53
Compressive strength of masonry in the direction perpendicular to bed joints	f'_m	MPa	**5.93**	0.52	0.09	**14.73**	1.00	0.07
Elastic modulus of masonry in the direction perpendicular to bed joints	E_1	MPa	**3174**	467	0.15	**7728**	1287	0.17
	E_2	MPa	**5091**	1774	0.35	**6921**	1288	0.19
	E_3	MPa	**2746**	282	0.10	**8156**	1334	0.16
Poisson ratio of masonry in the direction perpendicular to bed joints	ν		**0.14**	0.01	0.07	**-**	-	-
Fracture energy in compression for loading perpendicular to bed joints	$G_{f\text{-}c}$	N/mm	**31.5**	5.1	0.16	**47.0**	4.8	0.10
Compressive strength of masonry in the direction parallel to bed joints	$f_{m,h}$	MPa	**7.55**	0.17	0.02	**7.53**	0.59	0.08
Elastic modulus of masonry in the direction parallel to bed joints	$E_{1,h}$	MPa	**2212**	660	0.30	**5030**	483	0.10
	$E_{2,h}$	MPa	**3583**	1668	0.47	**6526**	1589	0.24
	$E_{3,h}$	MPa	**2081**	864	0.42	**4676**	766	0.16
Fracture energy in compression for loading parallel to bed joints	$G_{f\text{-}c,h}$	N/mm	**43.4**	7.2	0.17	**31.4**	8.1	0.26
Masonry flexural strength with the moment vector parallel to the bed joints and in the plane of the wall	f_{x1}	MPa	**0.21**	0.05	0.25	**0.40**	0.11	0.26
Masonry flexural strength with the moment vector orthogonal to the bed joint and in the plane of the wall	f_{x2}	MPa	**0.76**	0.36	0.47	**1.12**	0.28	0.25
Masonry flexural strength with the moment vector orthogonal to the plane of the wall	f_{x3}	MPa	**0.40**	0.09	0.23	**0.61**	0.11	0.17
Flexural bond strength	f_w	MPa	**0.27**	0.12	0.43	**0.27**	0.15	0.54
Masonry (bed joint) initial shear strength	f_{v0}	MPa	**0.14**			**0.15**		
Masonry (bed joint) shear friction coefficient	μ		**0.43**			**0.87**		
Residual masonry (bed joint) initial shear strength	$f_{v0,res}$	MPa	**0.03**			**0.01**		
Residual masonry (bed joint) shear friction coefficient	μ_{res}		**0.54**			**0.74**		

D

USRMATs, USRINDs and USRSTAs

Table D.1: USRMATs for zero-thickness interface elements

USRMAT	Notation	Unit	Property	Remarks
USRMAT(1)	$K_{s,e}$	MPa/mm	Elastic shear stiffness	Positive
USRMAT(2)	$K_{t,e}$	MPa/mm	Elastic tensile stiffness	Positive
USRMAT(3)	$K_{c,e}$	MPa/mm	Elastic compressive stiffness	Positive
USRMAT(4)	$G_{f,s}$	N/mm	Shear fracture energy	Positive
USRMAT(5)	$G_{f,t}$	N/mm	Tensile fracture energy	Positive
USRMAT(6)	$G_{f,c}$	N/mm	Compressive fracture energy	Positive; Defined differently for two compression curves
USRMAT(7)	ϕ	∘ circular degree	Friction angle	Positive
USRMAT(8)	c	MPa	Cohesion	Positive; Also called initial shear strength
USRMAT(9)	ft	MPa	Tensile strength	Positive
USRMAT(10)	fc	MPa	Compressive strength	Positive
USRMAT(11)	$ratio_{K,r}$	dimensionless	Ratio of residual stiffness	$0 \leqslant ratio_{K,r} \ll 1$; Shared by tension, compression and shear
USRMAT(12)	λ	dimensionless	Unloading and reloading factor	$0 \leqslant \lambda \leqslant 1$
USRMAT(13)	$d_{c,peak}$	mm	Compressive relative displacement corresponding to the compressive strength	Positive; Only valid for the Engineering Masonry Model compressive curve; Use random value for parabolic compressive curve.

Table D.2: USRINDs for zero-thickness interface elements

USRIND	Name	Initial value	Remarks
USRIND(1)	Initialization toggle	0	Becomes 1 after first step
USRIND(2)	Coupling Options	1 or 2	
USRIND(3)	Maximum number of sub-increments	user-defined	Must be $\geqslant 2$
USRIND(4)	Output toggle for *.out file	0 for no output, 1 for full output, 2 for simplified output	For models with huge number of steps or meshes, 0 is recommended
USRIND(5)	Output toggle in console	0 for no output, 1 for debug output	0 is recommended; Its value can be changed in console when error occurs
USRIND(6)	Type of compressive curve	1 for parabolic curve, 2 for Engineering Masonry Model curve	2 is recommended for masonry structures
USRIND(7)	Size of K_t array	0	Log the number of USRSTAs used to store Kt

Table D.3: USRSTAs for zero-thickness interface elements

USRSTA	Name	Initial value
USRSTA(1)	Tensile and shear damage factor	0.00000E+00
USRSTA(2)	Compressive damage factor	0.00000E+00
USRSTA(3)	Shear ultimate relative displacement	0.00000E+00
USRSTA(5)-(10)	Shear constitutive array K_s	0.00000E+00
USRSTA(11)-(22)	Compressive constitutive array K_c	0.00000E+00
USRSTA(23)-(n*)	Tensile constitutive array K_t	0.00000E+00

n should be a value much higher than 28. For the analyses conducted in this thesis, n= 200

E

Examples of DIANA text input

E.1. DAT file for model COMP_3

```
: Diana Datafile written for Diana 10.3
'UNITS'
LENGTH MM
FORCE N
'DIRECTIONS'
   1   1.00000E+00   0.00000E+00   0.00000E+00
   2   0.00000E+00   1.00000E+00   0.00000E+00
   3   0.00000E+00   0.00000E+00   1.00000E+00
'MODEL'
DIMENS "2D"
GRAVDI 2
GRAVAC  -9.81000E+03
'COORDINATES'
   1   0.00000E+00   0.00000E+00   0.00000E+00
   2   1.11111E+02   0.00000E+00   0.00000E+00
   3   2.22222E+02   0.00000E+00   0.00000E+00
   4   2.22222E+02   0.00000E+00   0.00000E+00
...
1579   1.00000E+03   2.76000E+03   0.00000E+00
1580   1.00000E+03   2.76000E+03   0.00000E+00
1581   1.11111E+03   2.76000E+03   0.00000E+00
'MATERI'
   1 NAME   "MortarHeadJoint"
     MATMDL USER
     DSNY     1.04357E+01
     DSSX     1.63636E+01
     USRIFC CYCLIC
     USRVAL   1.63636E+01   1.04357E+01   1.04357E+01   1.00000E-01
              7.75000E-06   3.40000E+01   2.32677E+01   1.40000E-02
              3.50000E-03   8.10000E+00   1.00000E-04   9.50000E-01
              3.30820E+00
     USRSTA   0.00000E+00   0.00000E+00   0.00000E+00   0.00000E+00
              0.00000E+00   0.00000E+00   0.00000E+00   0.00000E+00
... % At least 28 USRSTAs are needed, while actual situation usually
```

```
... % needs much more. Recommend to have more than 200 USRSTAs
              0.00000E+00   0.00000E+00   0.00000E+00   0.00000E+00
     USRIND 0 1 100 0 0 2 0
   2 NAME   "MortarBedJoint"
     MATMDL USER
     DSNY     1.21165E+02
     DSSX     3.93064E+01
     USRIFC CYCLIC
     USRVAL   3.93064E+01   1.21165E+02   1.21165E+02   3.00000E+00
              7.75000E-03   1.50000E+01   2.32677E+01   1.40000E-01
              1.05000E-01   5.93000E+00   1.00000E-04   9.50000E-01
              8.97265E-01
     USRSTA   0.00000E+00   0.00000E+00   0.00000E+00   0.00000E+00
              0.00000E+00   0.00000E+00   0.00000E+00   0.00000E+00
... % At least 28 USRSTAs are needed, while actual situation usually
... % needs much more. Recommend to have more than 200 USRSTAs
              0.00000E+00   0.00000E+00   0.00000E+00   0.00000E+00
     USRIND 0 1 100 0 0 2 0
   3 NAME   "ClayBrick"
     MCNAME CONCR
     MATMDL LEI
     ASPECT
     POISON   0.14000E+00
     YOUNG    8.99000E+03
     DENSIT   1.80500E-09
'GEOMET'
   1 NAME   "MortarGeo"
     GCNAME LINE
     GEOMDL STLIIF
     CONFIG MEMBRA
     THICK       1.02000E+02
   2 NAME   "BrickGeo"
     GCNAME SHEET
     GEOMDL MEMBRA
     THICK       1.02000E+02
   3 GCNAME LINE
     GEOMDL CLS1B2
     RECTAN   4.00000E+02   2.00000E+02
'ELEMENTS'
SET  "BrickLayer 1"
CONNECT
   1 Q8MEM  1 2 17 16
...
  19 Q8MEM  14 15 30 29
  20 Q8MEM  29 30 45 44
MATERIAL 3
GEOMETRY 2
...
SET  "HeadJointLayer 1"
CONNECT
 681 L8IF  4 19 3 18
 682 L8IF  19 34 18 33
 683 L8IF  7 22 6 21
 684 L8IF  22 37 21 36
 685 L8IF  10 25 9 24
 686 L8IF  25 40 24 39
```

```
 687 L8IF  13 28 12 27
 688 L8IF  28 43 27 42
MATERIAL 1
GEOMETRY 1
...
SET  ”BedJointLayer 1”
CONNECT
 987 L8IF  31 32 46 47
 988 L8IF  32 33 48 49
 989 L8IF  34 35 49 50
 990 L8IF  35 36 51 52
 991 L8IF  37 38 52 53
 992 L8IF  38 39 54 55
 993 L8IF  40 41 55 56
 994 L8IF  41 42 57 58
 995 L8IF  43 44 58 59
 996 L8IF  44 45 60 61
MATERIAL 2
GEOMETRY 1
...
’LOADS’
CASE 1
NAME ”Precompression”
NODAL
1566 FORCE  2  -4.53333E+04
WEIGHT
CASE 2
NAME ”Shear Prescribed Deformation”
DEFORM
1566  TR 1   1.00000E+00
COMBIN
   1 1   1.00000E+00
   2 2   1.00000E+00
’SUPPOR’
NAME ”BottomSupport”
1    TR 1
1    TR 2
NAME ”TopSupport”
1566  TR 1
’TYINGS’
NAME ”BottomTying”
EQUAL TR 1 TR 2
/ 2-15 / 1
EQUAL TR 1 TR 2
/ 1567-1581 / 1566
’END’
```

E.2. DCF file for COMP_3

```
*FILOS
INITIA
*INPUT
*FORTRAN
USE ”usrmat.dll”
*NONLIN LABEL=”Structural nonlinear”
```

```
  BEGIN EXECUT
    TEXT "Precompression and dead weight"
    BEGIN LOAD
      LOADNR 1
      STEPS EXPLIC SIZES 0.200000(5)
    END LOAD
    BEGIN ITERAT
      MAXITE 100
      METHOD SECANT
    END ITERAT
  END EXECUT
  BEGIN EXECUT
    TEXT "Shear prescribed displacement"
    BEGIN LOAD
      LOADNR 2
      STEPS EXPLIC SIZES \
-0.05000(3) 0.05000(6) -0.05000(6) 0.05000(6) -0.05000(6) 0.05000(6) \
-0.050000(8) 0.05000(10) -0.05000(10) 0.05000(10) -0.05000(10) 0.05000(10) \
-0.05000(13) 0.10000(8) -0.10000(8) 0.10000(8) -0.10000(8) 0.10000(8) \
-0.10000(15) 0.10000(22) -0.10000(22) 0.10000(22) -0.10000(22) 0.10000(22) \
-0.10000(28) 0.10000(34) -0.10000(34) 0.10000(34) -0.10000(34) 0.10000(34) \
-0.10000(47) 0.10000(60) -0.10000(60) 0.10000(60) -0.10000(60) 0.10000(60) \
-0.10000(74) 0.10000(88) -0.10000(88) 0.10000(88) -0.10000(88) 0.10000(88) \
-0.20000(58) 0.20000(72) -0.20000(72) 0.20000(72) -0.20000(72) 0.20000(72) \
-0.20000(100) 0.20000(128) -0.20000(128) 0.20000(128) -0.20000(128) 0.20000(128) \
-0.20000(132) 0.20000(136) -0.20000(136) 0.20000(136) -0.20000(136) 0.20000(136) \
-0.20000(192) 0.20000(248) -0.20000(248) 0.20000(248) -0.20000(248) 0.20000(248) \
-0.20000(300) 0.20000(352) -0.20000(352) 0.20000(352) -0.20000(352) 0.20000(352) \
-0.20000(176)
    END LOAD
    BEGIN ITERAT
      MAXITE 100
      METHOD SECANT
    END ITERAT
  END EXECUT
  BEGIN SOLVE
    BEGIN ITERAT
      PRECON ILU
      SUBSTR AUTOMA
    END ITERAT
  END SOLVE
  BEGIN OUTPUT
    TEXT "Output"
    BINARY
    SELECT STEPS ALL /
    DISPLA TOTAL TRANSL GLOBAL
    DISPLA TOTAL TRANSL LOCAL
    DISPLA INCREM TRANSL GLOBAL
    DISPLA INCREM TRANSL LOCAL
    STRAIN TOTAL GREEN GLOBAL INTPNT
    STRAIN TOTAL GREEN PRINCI INTPNT
    STRAIN TOTAL TRACTI LOCAL INTPNT
    STRAIN TOTAL TRACTI GLOBAL INTPNT
    STRESS TOTAL CAUCHY GLOBAL INTPNT
    STRESS TOTAL CAUCHY PRINCI INTPNT
    STRESS TOTAL TRACTI LOCAL INTPNT
```

```
    STRESS TOTAL TRACTI GLOBAL INTPNT
    FORCE REACTI TRANSL GLOBAL
    FORCE EXTERN TRANSL GLOBAL
  END OUTPUT
*END
```

Bibliography

[1] A. Anthoine. In-plane behaviour of masonry: A literature review. Technical report, Comission of the European Communities, JRC - Institute for Safety Technology, Ispra, Italy, 1992.

[2] R. Esposito, F. Messali, and J. G. Rots. Tests for the characterization of replicated masonry and wall ties. Technical report, Delft University of Technology, 4 2016.

[3] P. H. Feenstra. *Computational Aspects of Biaxial Stress in Plain and Reinforced Concrete*. PhD thesis, Delft University of Technology, 11 1993.

[4] T. M. Ferreira, A. A. Costa, and A. Costa. Analysis of the out-of-plane seismic behaviour of unreinforced masonry: A literature review. *International Journal of Architectural Heritage*, 9(8): 949–972, 2015. doi: 10.1080/15583058.2014.885996. URL https://doi.org/10.1080/15583058.2014.885996.

[5] KNMI. Aardbevingen door gaswinning. https://www.knmi.nl/kennis-en-datacentrum/uitleg/aardbevingen-door-gaswinning. Accessed: 2019-01-01.

[6] P. B. Lourenço. *Computational strategies for masonry structures*. PhD thesis, Delft University of Technology, 02 1996.

[7] P. B. Lourenço and J. G. Rots. Multisurface interface model for analysis of masonry structures. *Journal of Engineering Mechanics*, 123(7):660–668, 1997. doi: 10.1061/(ASCE)0733-9399(1997)123:7(660).

[8] V Mariani, F Messali, MAN Hendriks, and JG Rots. Numerical modelling and seismic analysis of dutch masonry structural components and buildings. In *16th World Conference on Earthquake Engineering, 16WCEE 2017*, 2017.

[9] N. Mendes and P. B. Lourenço. *Seismic Vulnerability of Existing Masonry Buildings: Nonlinear Parametric Analysis*, pages 139–164. 04 2015. ISBN 978-3-319-16129-7. doi: 10.1007/978-3-319-16130-3_6.

[10] D. Ngo and A. C. Scordelis. Finite element analysis of reinforced concrete beams. *Journal Proceedings*, 64(3). doi: 10.14359/7551.

[11] Y. R. Rashid. Analysis of reinforced concrete pressure vessels. *Nuclear Engineering and Design*, 7:334–344, 04 1968. doi: 10.1016/0029-5493(68)90066-6.

[12] G. Ravenshorst and F. Messali. In-plane tests on replicated masonry walls. Technical report, Delft University of Technology, 4 2016.

[13] J. G. Rots. Numerical simulation of cracking in structural masonry. *Heron*, 36:49–63, 01 1991.

[14] G. M. A. Schreppers, A. Garofano, F. Messali, and J. G. Rots. Diana validation report for masonry modelling. Technical report, DIANA FEA BV and Delft University of Technology, 2 2016.

[15] C. Vlek. Induced earthquakes from long-term gas extraction in groningen, the netherlands: Statistical analysis and prognosis for acceptable-risk regulation. *Risk Analysis*, 38(7):1455–1473, 7 2018. ISSN 0272-4332. doi: 10.1111/risa.12967. URL https://doi.org/10.1111/risa.12967.